MODELING AND CONTROLLER DESIGN OF A VTOL AIR VEHICLE

A THESIS SUBMITTED TO
THE GRADUATE SCHOOL OF NATURAL AND APPLIED SCIENCES
OF
MIDDLE EAST TECHNICAL UNIVERSITY

BY

ANIL SAMİ ÖNEN

IN PARTIAL FULFILLMENT OF THE REQUIREMENTS
FOR
THE DEGREE OF MASTER OF SCIENCE
IN
AEROSPACE ENGINEERING

MARCH 2015

Approval of the thesis:

MODELING AND CONTROLLER DESIGN OF A VTOL AIR VEHICLE

submitted by **ANIL SAMİ ÖNEN** in partial fulfillment of the requirements for the degree of **Master of Science in Aerospace Engineering Department, Middle East Technical University** by,

Prof. Dr. Gülbin Dural Ünver _____
Dean, Graduate School of **Natural and Applied Sciences**

Prof. Dr. Ozan Tekinalp _____
Head of Department, **Aerospace Engineering**

Prof. Dr. Ozan Tekinalp _____
Supervisor, **Aerospace Engineering Dept., METU**

Assoc. Prof. Dr. D. Funda Kurtuluş Bozdemir _____
Co-Supervisor, **Aerospace Engineering Dept., METU**

Examining Committee Members:

Assoc. Prof. Dr. lkay Yavrucuk _____
Aerospace Engineering Dept., METU

Prof. Dr. Ozan Tekinalp _____
Aerospace Engineering Dept., METU

Assoc. Prof. Dr. D. Funda Kurtuluş Bozdemir _____
Aerospace Engineering Dept., METU

Asst. Prof. Dr. Ali Türker Kutay _____
Aerospace Engineering Dept., METU

Assoc. Prof. Dr. Tayfun Çimen _____
Roketsan A.Ş.

Date: 12.03.2015

I hereby declare that all information in this document has been obtained and presented in accordance with academic rules and ethical conduct. I also declare that, as required by these rules and conduct, I have fully cited and referenced all material and results that are not original to this work.

Name, Last Name : Anıl Sami ÖNEN

Signature :

ABSTRACT

MODELING AND CONTROLLER DESIGN OF A VTOL AIR VEHICLE

Önen, Anıl Sami
M.S., Department of Aerospace Engineering
Supervisor: Prof. Dr. Ozan Tekinalp
Co-Supervisor: Assoc.Prof. Dr. D.Funda Kurtuluş Bozdemir

March 2015, 120 pages

This thesis focuses on modeling, controller design, production and flight test of a VTOL unmanned air vehicle. The air vehicle that is designed and manufactured for this study has three propellers. A nonlinear mathematical model of the aircraft is developed. For this both numerical codes as well as wind tunnel tests have been carried out. A simulation code is then written in MATLAB/Simulink environment that describes the physical properties of the system in detail. After trimming the air vehicle at appropriate equilibrium points in hover and forward flight phase separately, the nonlinear model is linearized around that trim points and Linear Quadratic Regulator (LQR) and Linear Quadratic Tracking (LQT) controllers are designed. After verifying both controllers through the nonlinear simulation, hover flight tests of the aircraft are also successfully carried out and results are reported.

Keywords: Vertical take-off and landing, unmanned air vehicle, hover flight control, flight testing

ÖZ

DİKEY KALKIŞ VE İNİŞ YAPABİLEN BİR HAVA ARACININ MODELLENMESİ VE KONTROLCÜ TASARIMI

Önen, Anıl Sami
Yüksek Lisans, Havacılık ve Uzay Mühendisliği Bölümü
Tez Yöneticisi: Prof. Dr. Ozan Tekinalp
Eş-Tez Yöneticisi: Doç.Dr. D.Funda Kurtuluş Bozdemir

Mart 2015, 120 sayfa

Bu tez, dikey kalkış ve iniş yapabilen bir insansız hava aracının modellenmesi, kontrolcü tasarımı, üretimi ve teslterini içermektedir. Bu çalışma için tasarlanan ve üretilen hava aracı, üç pervaneye sahiptir. Hava aracının doğrusal olmayan matematik modeli oluşturulmuştur. Bunun için nümerik hesaplamalar ve rüzgar tüneli testleri yapılmıştır. Ardından hava aracının fiziksel özelliklerini detaylı bir şekilde tanımlayan simülasyon kodu MATLAB/Simulink ortamında yazılmıştır. Hava aracının havada asılı kalma ve ileri uçuş fazlarında uygun denge noktalarının bulunmasının ardından, doğrusal olmayan model bu denge noktaları etrafında doğrusal hale getirilmiş ve Doğrusal Karesel Regülatör (LQR) ve Doğrusal Karesel Takip (LQT) kontrolcüleri tasarlanmıştır. Tasarlanan kontrolcülerin doğrusal olmayan simülasyon kodu ile doğrulanmasının ardından, tasarlanan hava aracı ile havada asılı kalma fazında uçuş testleri başarı ile gerçekleştirilmiş sonuçlar raporlanmıştır.

Anahtar Kelimeler: Dikey kalkış-iniş, insansız hava aracı, havada asılı kalma uçuş kontrolcüsü, uçuş testi

To my mom and my love

ACKNOWLEDGEMENTS

I would like to express my gratitude to my supervisor Prof. Dr. Ozan Tekinalp and my co-supervisor Assoc. Prof. Dr. D. Funda Kurtuluş Bozdemir for their valuable guidance and patience throughout this study. Furthermore I would like to thank Murat Şenipek who has shared his valuable comments about the modeling process. I would like to thank Talha Mutlu who has shared his precious time during the manufacturing process and constructing the test setup and Levent Cevher who has helped me in constructing the hardware and installing the software. Moreover, I would like to thank Osman Güngör, İsmail Özdemir Uzunlar and Caner Çalık who have willingly shared their precious time during the experimental studies. Without their help this study could not have been finalized. I would like to thank the team members [1] of the METU Aerospace Department for AIAA / DBF 2013 competition for the initial design that is modified in this study. I would also like to thank to Arda Aksu and Özer Güvenç for their valuable comments and insight into the topic. In addition I would like to thank Saffet Gökuç who has shared his valuable time for the flight tests.

I would like to thank my partner, Mutlu, for her love, kindness, patience and support she has shown throughout the study. Last but not the least, I would like to thank to my family for their endless love. Words cannot express how grateful I am to my parents for all of the sacrifices that they have made on my behalf.

Finally, I would like to thank Boeing Company for the support to cover the production costs of this aircraft.

TABLE OF CONTENTS

LIST OF TABLES

TABLES

LIST OF FIGURES

FIGURES

NOMENCLATURE

p, q, r	Body axis angular rates (roll, ptitch, yaw)
$\dot{u}, \dot{v}, \dot{w},$	Body axis translational accelerations
u, v, w	Body axis velocities
x, y, z	Earth axis positions
ϕ,θ, ψ	Euler angles (roll, pitch, yaw)
ϕ_{com}, θ_{com}, ψ_{com}	Pilot commands (roll, pitch, yaw)
α, β	Wind angles (angle of attack, sideslip angle)
σ, δ	Electric motor tilt angles (front, aft)
δ_{elev}, δ_{rudder}, $\delta_{aileron}$	Control surface deflections (elevator, rudder, aileron)
δ_{th1}, δ_{th2}, δ_{th3},	Electric motor throttle inputs (percentage)
V	Total velocity relative to air
C_L, C_D	Lift and drag coefficient
C_x, C_y, C_z	Body axis non-dimensional aerodynamic force coefficients
C_l, C_m, C_n	Body axis non-dimensional aerodynamic moment coefficients
I_{xx}, I_{yy}, I_{zz}	Mass moment of inertias
I_{xy}, I_{xz}, I_{yz}	Product moment of inertias
ρ	Air density
b	Span
$\bar{c}$	Mean chord length
S	Wing area
$\bar{q}$	Dynamic pressure
a_{sound}	Speed of sound
m	Mass
g	Gravitational acceleration
DCM	Direction Cosine Matrix
DoF	Degrees of Freedom
r_x	The distance between the front motors and the center of gravity of the aircraft in x axis.

r_x^{aft}	The distance between the aft motor and the center of gravity of the aircraft in x axis.
r_y	The distance between the front motors and the center of gravity of the aircraft in y axis.
r_z	The distance between the front motors and the center of gravity of the aircraft in z axis.
r_z^{aft}	The distance between the aft motor and the center of gravity of the aircraft in z axis.
Q_1	The reactive torque value of the first electric motor
Q_2	The reactive torque value of the second electric motor
Q_3	The reactive torque value of the third electric motor

CHAPTER 1

INTRODUCTION

Aircraft with vertical take-off and landing capability has attracted interest for many years. While helicopters offer good hover capabilities, tilt rotor aircraft may take-off and land vertically as well as fly faster and has longer endurance.

This chapter presents a brief literature review on Unmanned Air Vehicles (UAVs), specifically with vertical take-off and landing (VTOL) UAVs and the modeling and control of them. Moreover, this chapter mentions the aim of this thesis and describes the document overview.

1.1 Literature Review

1.1.1 Competitor Study

In recent years, the use of the UAVs has been significantly increased. This stems from the fact that the UAVs can perform various kinds of missions including surveillance, target acquisition/designation, reconnaissance, data acquisition, rapid supply of materials, so and so forth. In handling such missions, working with UAVs is much more feasible than manned aircrafts.

There are three kinds of UAV configurations that are mainly used; fixed wing configuration, helicopter configuration and tilt rotor configuration. The fixed wing configuration has a fixed wing-fuselage combination and a propulsion system that is

placed in such a way that the thrust vector is produced in the horizontal direction. A runway is required for this configuration in order to take-off and land. The helicopter configuration which has a rotor mounted on the fuselage do not need a runway to take-off and land because the rotor above the fuselage produces thrust in such a way that the aircraft can take-off and land vertically. The last configuration is the compromise between these two. It does not need a runway to take-off and land as it can produce vertical lift with the propulsion system that is mounted vertically. Moreover, it can perform forward flight by tilting the engines. Not only having the capability of performing forward flight, but also taking-off and landing vertically is a great contribution to aeronautics and several studies have been done on this subject.

In Figure 1 several examples of VTOL UAVs are given.

(a) Panther UAV [2]

(b) Aerovel-Flexrotor [3]

(c) Scorpion [4]

(d) QTW QUX-02A [5]

Figure 1 VTOL UAV Concepts

Panther UAV (Figure 1.a) performs transition between hover and cruise state by thrust vectoring. Panther UAV's wing and stabilizers stand in stable position during transition. Aerovelco-Flexrotor (Figure 1.b) takes-off toward its tail over its special platform. Aerovelco-Flexrotor's control surfaces and stabilizers are used for

transition during flight. Scorpion (Figure 1.c) has a unique design. Although Scorpion does not perform vertical take-off, it can take-off in short distances. Scorpion performs its take-off and landing by thrust vectoring. The most important property of Scorpion is that it has a pivoting wing configuration during all flight profile including turbulent conditions. Last competitor aircraft, QTW QUX-02A (Figure 1.d) perform its takeoff and landing by using 4 vertically mounted electric motors to the wing. Wings are tilted from vertical position to ground parallel position during transition.

Some full size military models have been developed. There is also a continued interest for UAV's taking off and landing automatically. In this thesis design-development and flight control of such an aircraft is reported.

1.1.2 Modeling and Control

Autonomous hover and transition for fixed wing aircrafts are investigated in the past. The linear or nonlinear controllers that are designed are verified by using simulation and flight test results especially for hover and transition flight modes. A research group from Georgia Institute of Technology for instance has studied dynamic inversion with neural network adaptation to provide an adaptive controller capable of transitioning a fixed-wing UAV to and from hovering flight in a nearly stationary position. [6] Another research group from Gyeongsang National University has designed a trajectory tracking controller for a tiltrotor unmanned aerial vehicle that is capable of controlling the aircraft with one fixed controller architecture for all flight modes. [7] A research group from ETH Zurich designed a hybrid aircraft 'PacFlyer' that is capable of taking-off and landing vertically like a helicopter and flying in cruise like a regular airplane. The aircraft can perform a fully controlled flight envelope with the aid of a pilot. For cruise and hover, PID controllers are used, whereas for transition both the model and the controller for cruise and hover are combined. [8] In another study from Linköping University a model predictive controller is designed to stabilize the rotational rates of a tricopter UAV. The

controller is a multivariable controller that uses a quadratic optimization problem to compute the optimal control signal. [9]

1.2 Major Objectives

The major objective of this study is to create a model that very well describes the physical properties of the air vehicle and design a controller that stabilizes the air vehicle in hover phase and forward flight phase. The performance of the controller will be observed with the simulation and hardware tests.

1.3 Document Overview

The specification of the vehicle designed and manufactured is given in Chapter 2. The nonlinear dynamic model that simulates 6 DoF flight mechanics of the air vehicle is explained in Chapter 3. In Chapter 4, trimming and linearization analyses are presented for hover and forward flight phases. In Chapter 5, linear controller design is given and in Chapter 6 simulation results are presented. Chapter 7 presents hover flight tests conducted in the laboratory. Finally, the conclusion and recommendations for future work are given in Chapter 7.

CHAPTER 2

AIR VEHICLE DESIGN CHARACTERISTICS

In this chapter, the specification of the air vehicle that is studied throughout this thesis is given. As presented in the literature review section, there are various kinds of UAVs that are used in many different kinds of applications. Among all configurations, a vertical take-off and landing (VTOL) configuration is chosen for this study.

2.1 Design Specification

Using a proven design is thought to be more advantageous rather than designing a new aircraft. The aircraft that was designed and built previously for the AIAA (American Institute of Aeronautics and Astronautics) Design, Build and Fly (DBF) competition 2013 is chosen as an initial design. The theme of DBF 2013 was a joint strike fighter design which makes some design constraints common with the VTOL design concept.

Main reasons for choosing the competition aircraft are listed below:

Short Takeoff

The aircraft is capable of taking-off from very short distances like 10 meters. This implies that the aircraft can produce enough lift force to take-off at low speeds. This feature helps VTOL UAV at transition phase, since it can transit to the forward flight at low speeds.

Twin Engine Configuration

The aircraft has twin engine configuration which is an advantage for a VTOL UAV, due to the large thrust requirement during vertical take-off.

2.2 DBF'2013 Aircraft

The specifications of the DBF'2013 aircraft are given in Table 1. [1]

Table 1 Geometrical Parameters of DBF 2013 Aircraft

Wing		**Inverted V-Tail Properties**		**Aileron**	
Airfoil	S1223	Airfoil	NACA 0009	Span [m]	0.37
Span [m]	1.5	Angle Between V	92.3	% of Chord	25%
MAC	0.341	Span [m]	0.55	Max δ_a	30 ^{o}
Area [m2]	0.502	Total Area [m2]	0.114	**Flap**	
Aspect Ratio	4.48	Vertical Distance [m]	0.552	Span [m]	0.4
Taper Ratio	0.618	Chord [m]	0.148	% of Chord	25%
Oswald's eff.	0.934	Incidence Angle	-1	Max δ_f	30^o
Static Margin	13%	**Motor**		**Rudder-Vator**	
Incidence Angle	1	Type	A20 6XL	Span [m]	0.523
Twist Angle	2	Kv	1050	% of Chord	40%
c/4 Sweep	0	RPM_{max}	12000	Max δ_r	35 ^{o}
Fuselage		Rm	0.075	**Electrical System**	
Length [m]	0.74	Operating Current [A]	20	ESC	MASTERSPIN 22
Width [m]	0.16	Propellers	9x6 APC	Servo Act.	HS55-S3117
Height [m]	0.12	Propellers	10x5 Xoar	Receiver	FUTABA

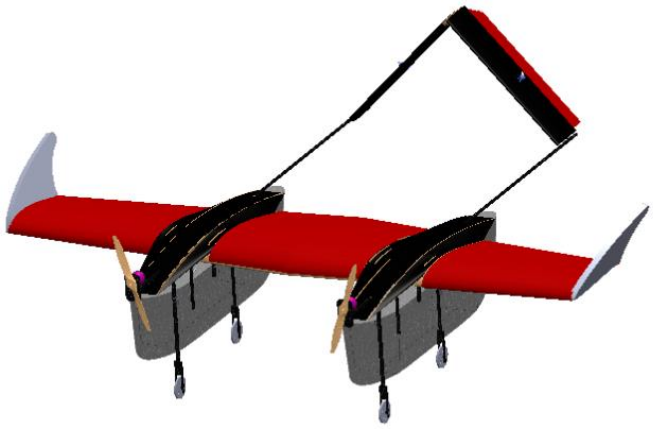

Figure 2 DBF 2013 Aircraft

In Figure 2, DBF 2013 aircraft is shown. It has a twin fuselage configuration with twin engine propulsion system. Moreover, inverted V-tail provides good control characteristics at stall condition.

2.3 Modifications to DBF 2013 Aircraft

In order to convert the present design into a tricopter UAV, some design modifications are made. Firstly, the front electric motors are mounted on a single shaft for simultaneous tilting of the propellers. One servo motor is used for the tilt mechanism. An additional electric motor is mounted aft of the center of gravity to provide an additional vertical thrust in the hover phase. This third motor also has a tilting capability around body x-axis for yaw stability and control during hover. Twin boom configuration is conserved, whereas the double fuselage is replaced with a single one for weight and drag reduction. The tail is placed 14 cm back when compared with the original design in order to tune the location of the center of gravity of the aircraft. This modification is crucial to satisfy the static stability of the aircraft both in hover and forward flight. The avionics of the aircraft is mounted below the middle of the wing. Moreover, with reduction of the fuselage, four wheel landing gear configuration is converted into a tricopter configuration. The final design is shown in Figure 3. The modified aircraft has a take-off weight of 3.4 kg and capability of lifting 3.79 kg maximum take-off weight.

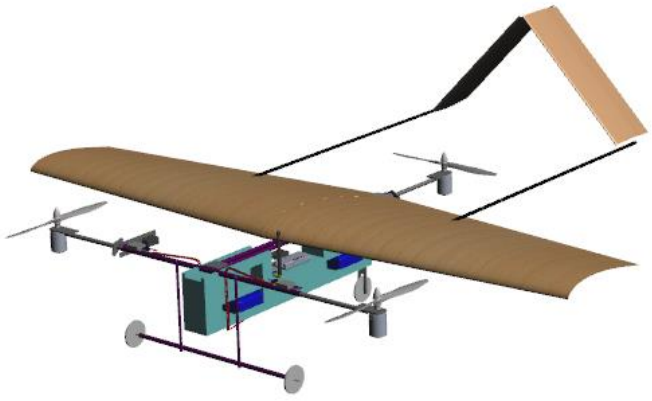

Figure 3 Prototype Aircraft

CHAPTER 3

NONLINEAR DYNAMIC MODEL

This section describes the nonlinear dynamic model developed for simulating the 6-DoF flight of the tricopter VTOL air vehicle. The model is coded in MATLAB/Simulink environment with equations of motion, the aerodynamics of the wing and tail, the propulsion system and gravitational effects. Attitude equations are also implemented. The dynamic model of the actuators that are the electric motors, front and aft tilting servos are not included in the model. The time required to tilt the front electric motors is measured to be 0.4 seconds and this result is assumed to be fast enough not to construct an actuator dynamic model. Moreover, in hover flight tests that are mentioned in Chapter 7, the response of the actuators are fast enough in stabilizing the aircraft.

3.1 Subsystems of the Nonlinear Model

The nonlinear aircraft model consists of five subsystems that are shown in Figure 4.

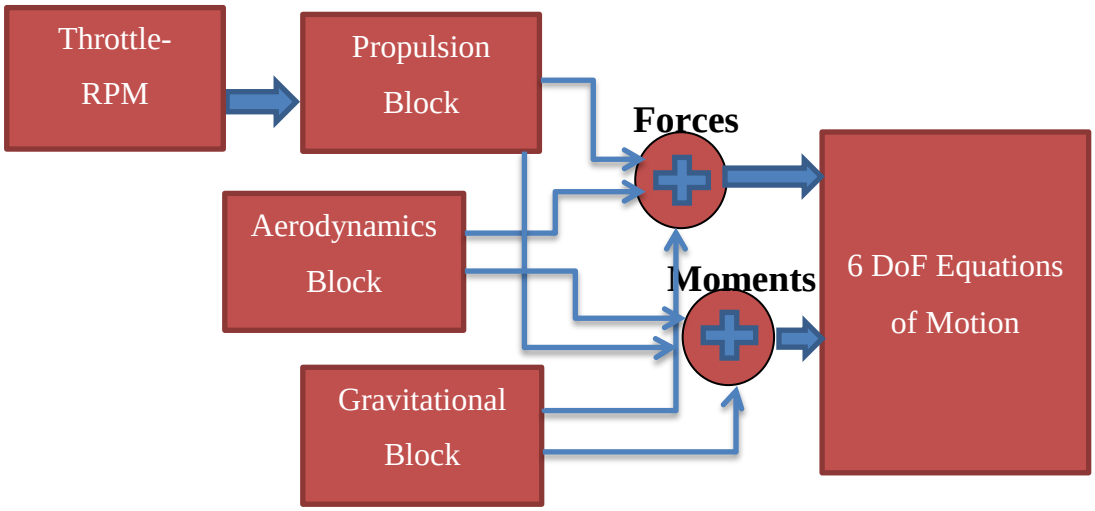

Figure 4 Nonlinear Model

3.1.1 Throttle-RPM Conversion Block

First submodel is the throttle-RPM conversion block. This block is created in order to make a relation between the throttle value of the transmitter and the RPM values of the electric motors. RPM values are used as an input for the propulsion subsytem block. To create a model experimentally, the throttle value of the transmitter and RPM value of the electric motor are logged throughout the test with the help of ESC (Electronic Speed Controller). After the tests these values are used to identify the relation between throttle and RPM by using the curve fitting toolbox in MATLAB. A second order polynomial that is shown in Eqn. (1) is used for all electric motors as they are identical.

$$RPM = p_1 * {\delta_T}^2 + p_2 * \delta_T + p_3 \quad (1)$$

where,

$$p_1 = -0.2772,\ p_2 = 129.64,\ p_3 = -161.55$$

The throttle-RPM conversion block is shown in Figure 5.

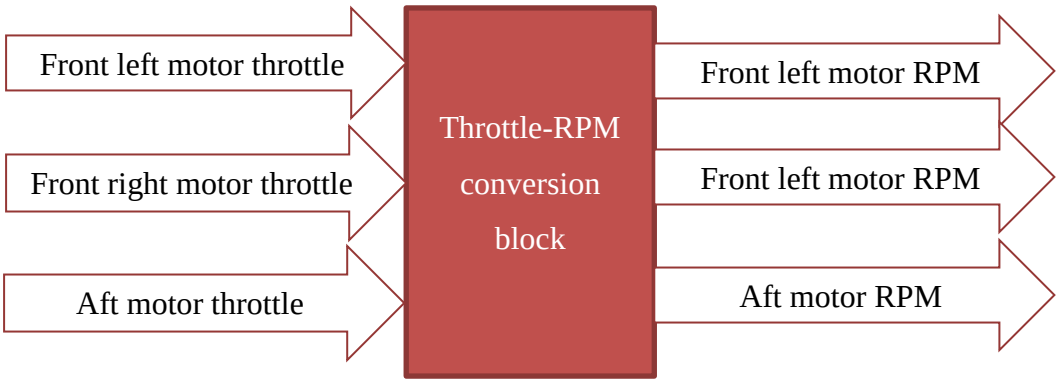

Figure 5 Throttle-RPM Conversion Block

3.1.2 Propulsion Model

The propulsion system block is based on a classical blade element/vortex formulation. An open source code, named as QPROP [10] is used. This code computes the thrust and torque values of the motor-propeller combinations with the knowledge of the geometry of the propeller, RPM value of the electric motor and the axial velocity that the motor faces directly. For this purpose a 10x5 propeller is cut into pieces as shown in Figure 6 and at each section local blade angle, blade chord, blade radius, zero lift angle of attack, lift curve slope are estimated. These values are modified in the generic code and shown in APPENDIX A.

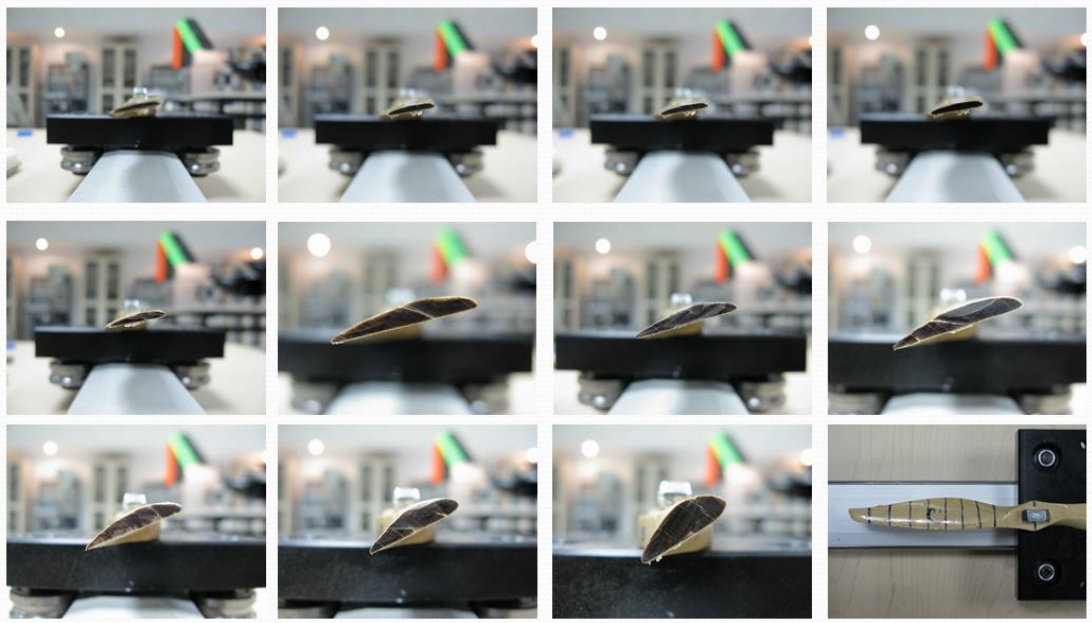

Figure 6 Propeller Geometry Identification

To verify the QPROP code and determine the performance characteristics of the electric motor-propeller combination, wind tunnel tests are performed in 1m x 1m wind tunnel of the Aerospace Engineering Department for different rotor angles and wind speed. [11] Wind tunnel test setup is shown in Figure 7, rotor angles and wind speed that are sampled in wind tunnel tests are shown in

Table 2. Electric motor with the firewall is mounted to a load cell that is capable of measuring all the forces and moments in the body fixed coordinate frame.

Figure 7 Wind Tunnel Test Setup

Table 2 Wind tunnel test parameters

Rotor angle (deg)	**0, 20, 40, 60**
Wind speed (m/s)	0, 5, 8, 10, 12 15, 20, 30

0^o rotor angle corresponds to the level flight condition, in other words front electric motors are positioned along body-x axis of the aircraft.

8 m/s and 12 m/s wind speed are particularly tested for 40^o and 60^o rotor angles, because obtaining the thrust and torque values around stall speed at high rotor angles is critical especially for transition flight phase. RPM values of the electric motors, axial speed in the wind tunnel, the thrust and torque values corresponding to different RPM values at different rotor angles and wind speed are recorded and a database is created. In logging the data, a DAQ system is used to record the load cell data and ESC (Electronic Speed Controller) is used to record the RPM values. The results of the wind tunnel tests are compared with the results of the blade element formulation of the QPROP.

The comparison of thrust and torque relation with RPM for 0^o and 40^o rotor tilt angles at different wind speeds are shown in Figure 8-Figure 23. The blue lines correspond to the experimental data and the green ones correspond to QPROP solution.

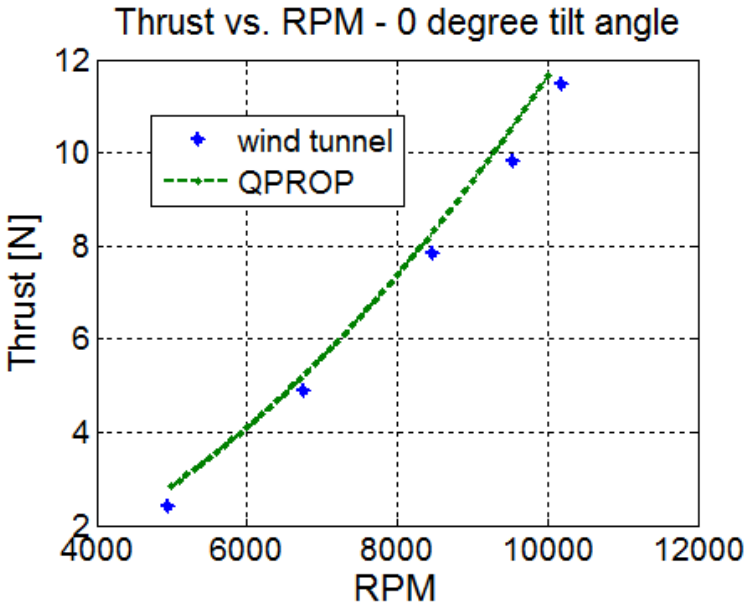

Figure 8 Comparison of Thrust [N] in QPROP with Experimental Data-at 0 m/s wind speed

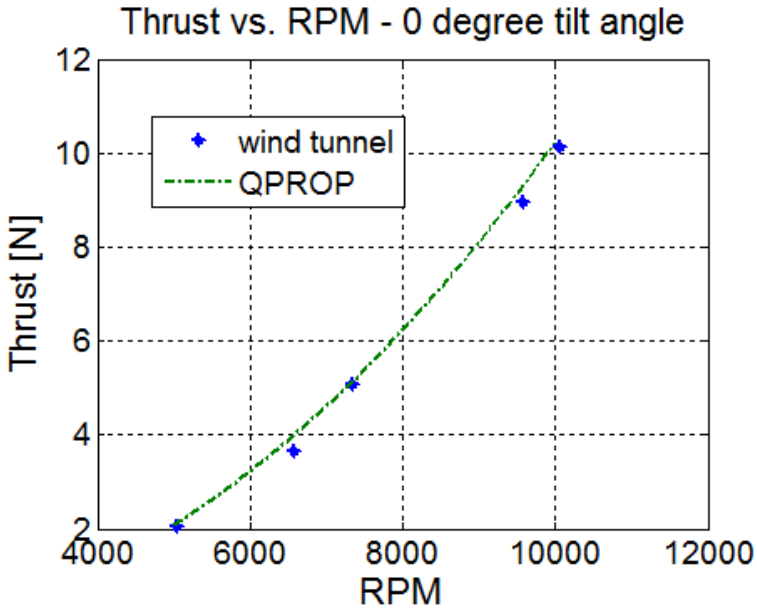

Figure 9 Comparison of Thrust [N] in QPROP with Experimental Data-at 5 m/s wind speed

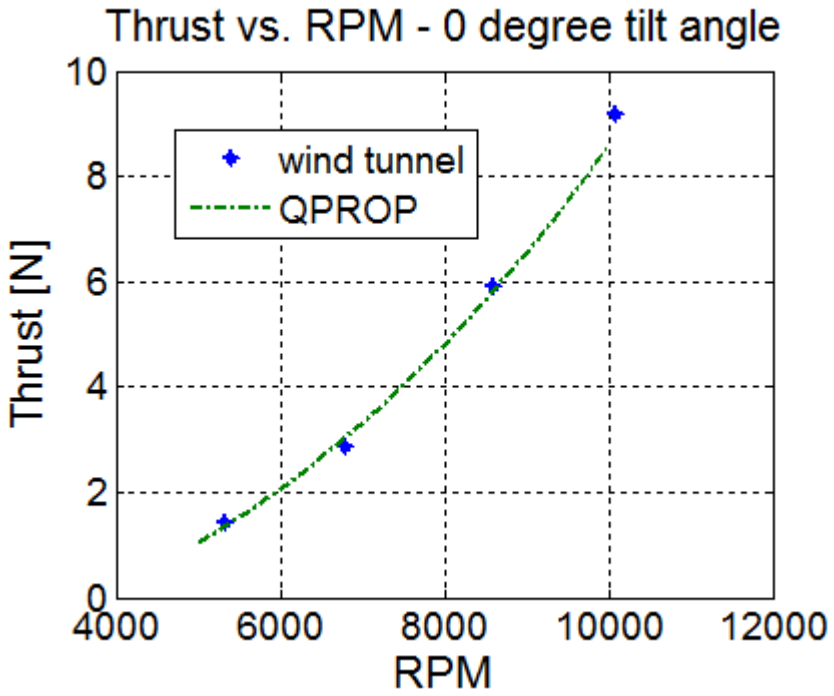

Figure 10 Comparison of Thrust [N] in QPROP with Experimental Data-at 10 m/s wind speed

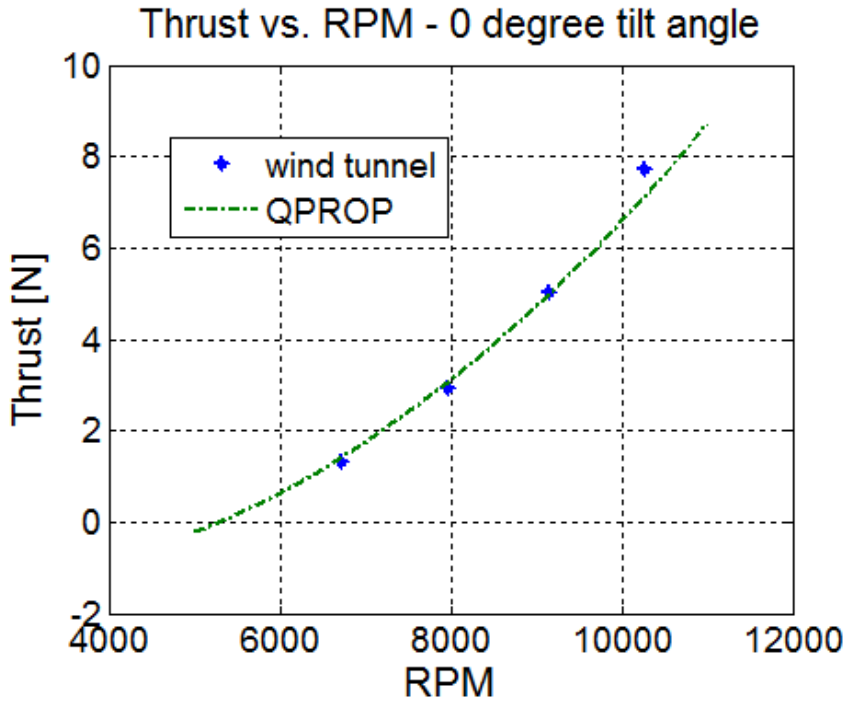

Figure 11 Comparison of Thrust [N] in QPROP with Experimental Data-at 15 m/s wind speed

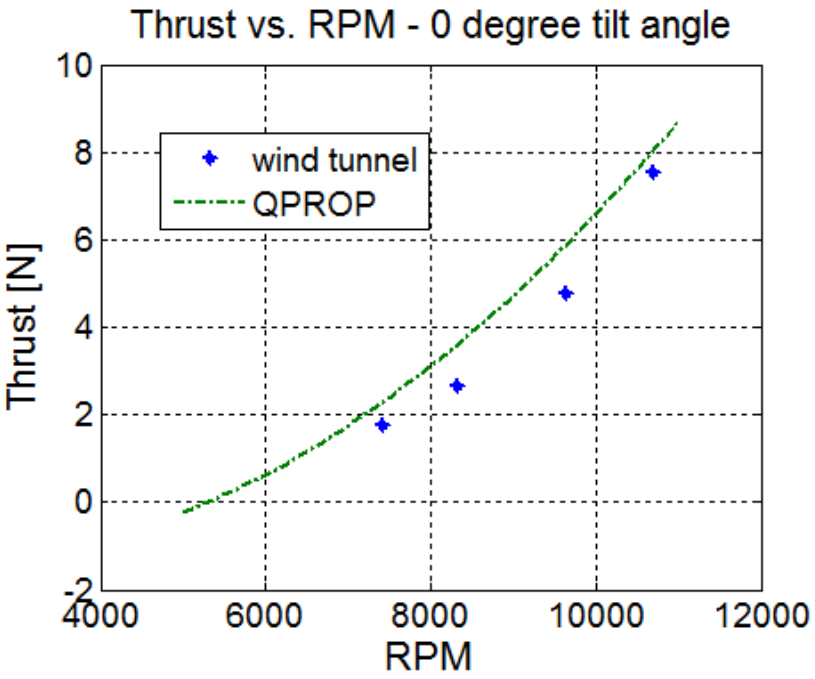

Figure 12 Comparison of Thrust [N] in QPROP with Experimental Data-at 20 m/s wind speed

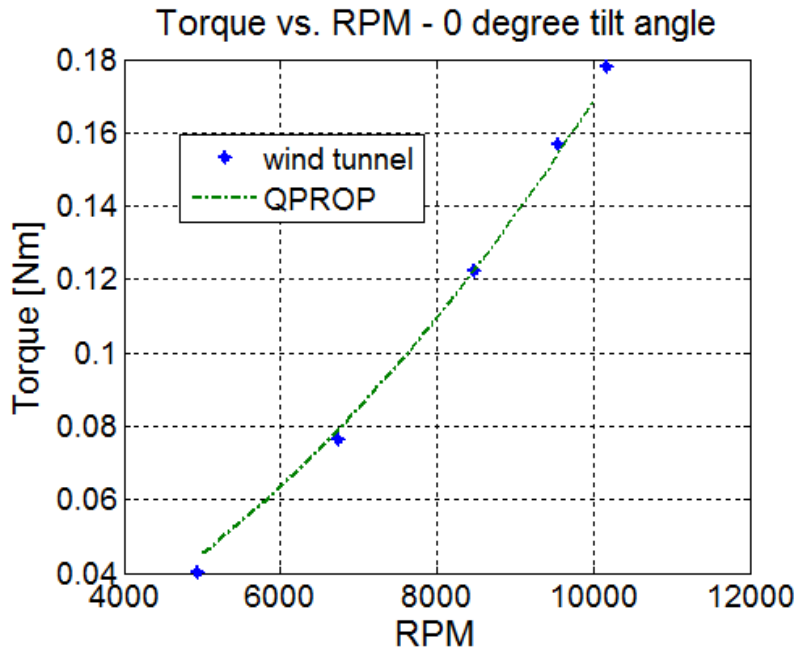

Figure 13 Comparison of Torque [Nm] in QPROP with Experimental Data-at 0 m/s wind speed

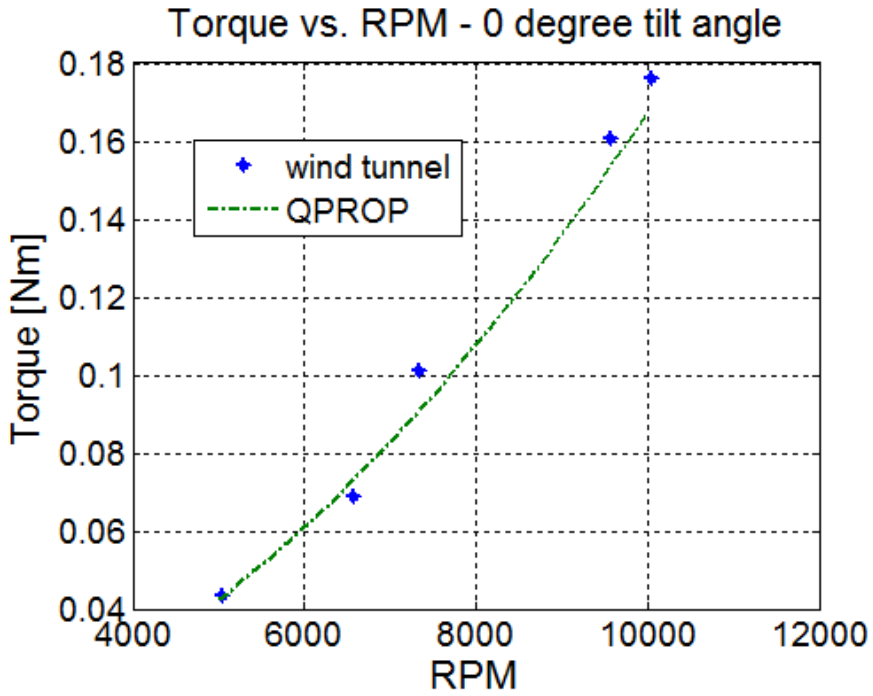

Figure 14 Comparison of Torque [Nm] in QPROP with Experimental Data-at 5 m/s wind speed

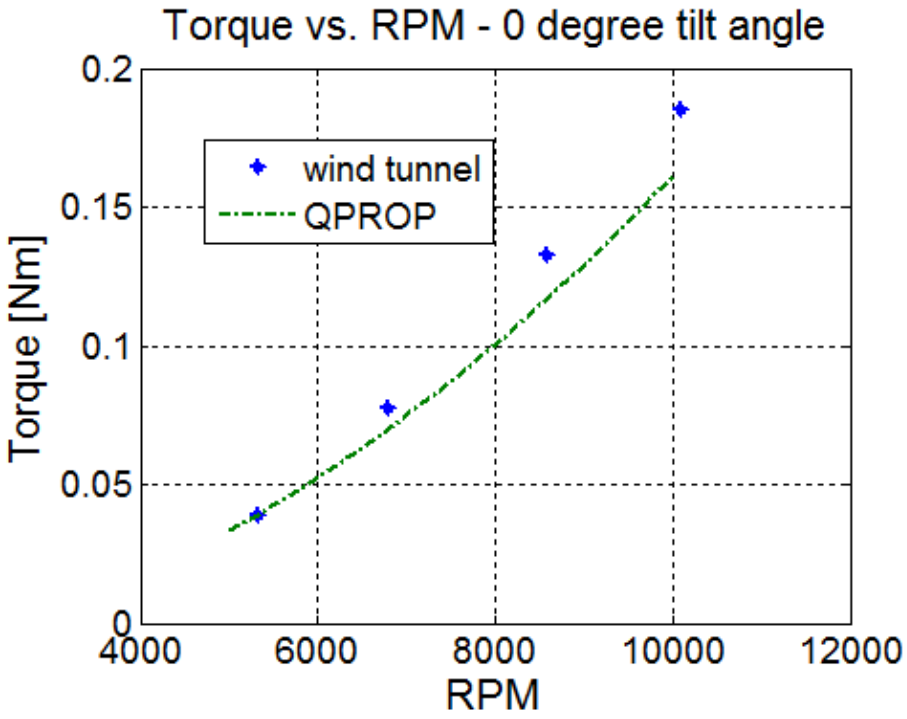

Figure 15 Comparison of Torque [Nm] in QPROP with Experimental Data-at 10 m/s wind speed

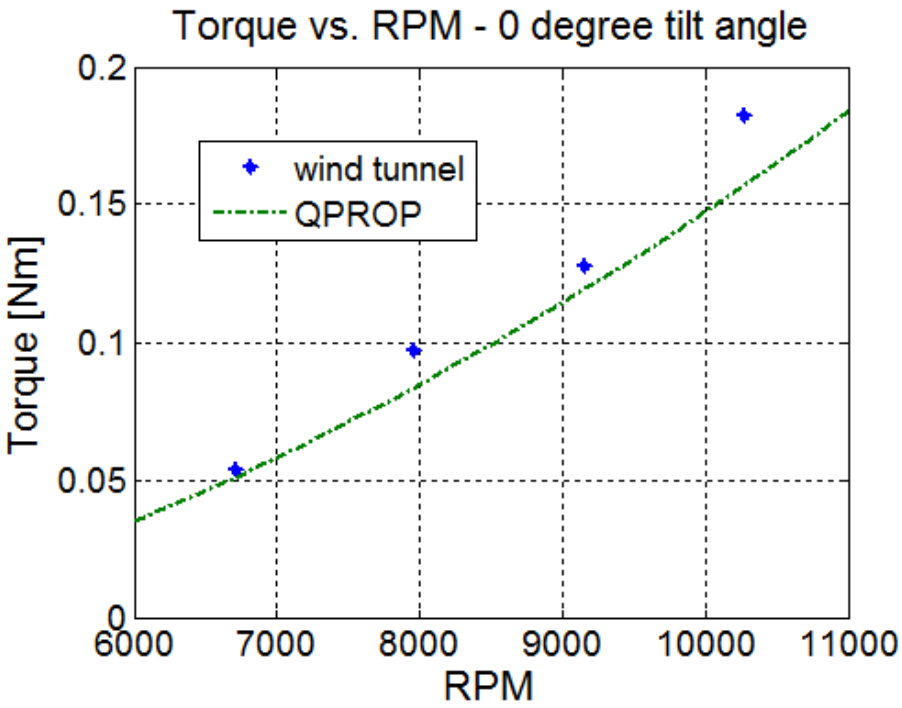

Figure 16 Comparison of Torque [Nm] in QPROP with Experimental Data-at 15 m/s wind speed

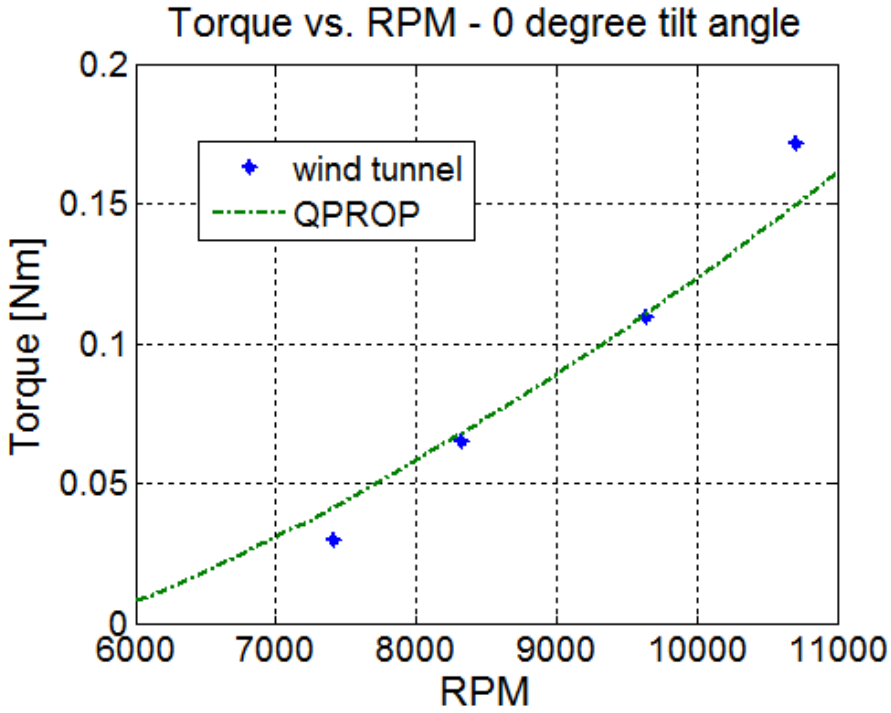

Figure 17 Comparison of Torque [Nm] in QPROP with Experimental Data-at 20 m/s wind speed

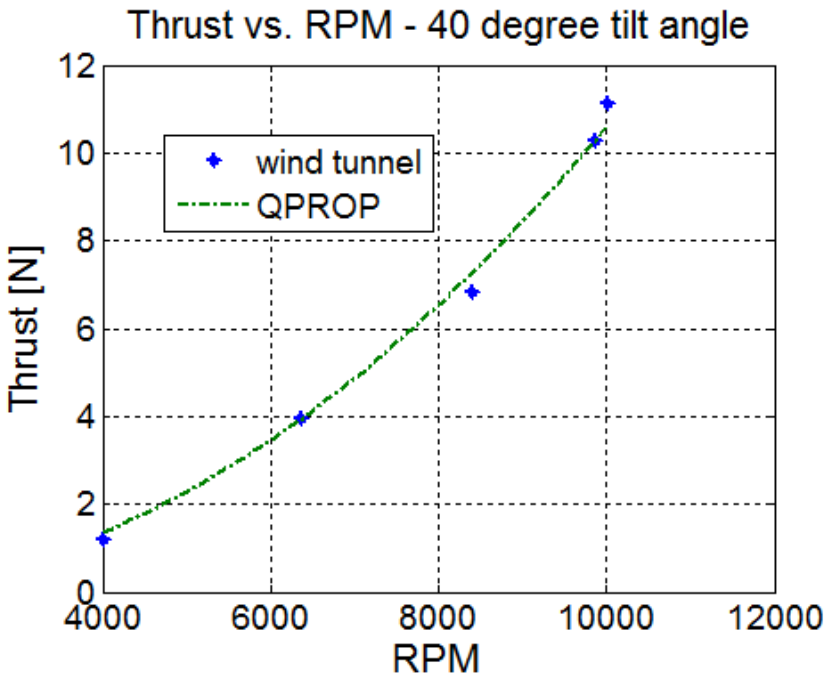

Figure 18 Comparison of Thrust [N] in QPROP with Experimental Data-at 5 m/s wind speed

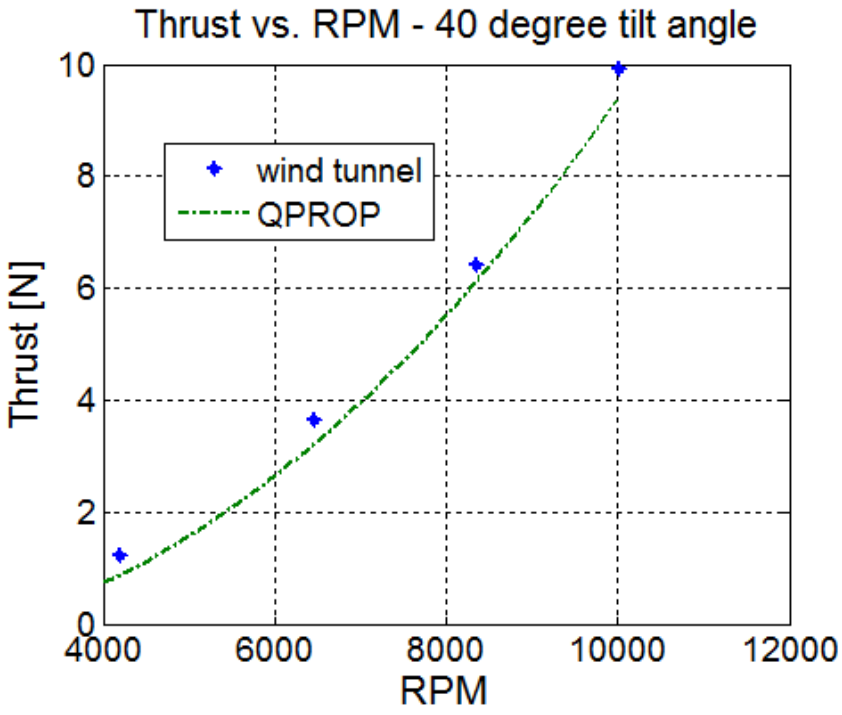

Figure 19 Comparison of Thrust [N] in QPROP with Experimental Data-at 10 m/s wind speed

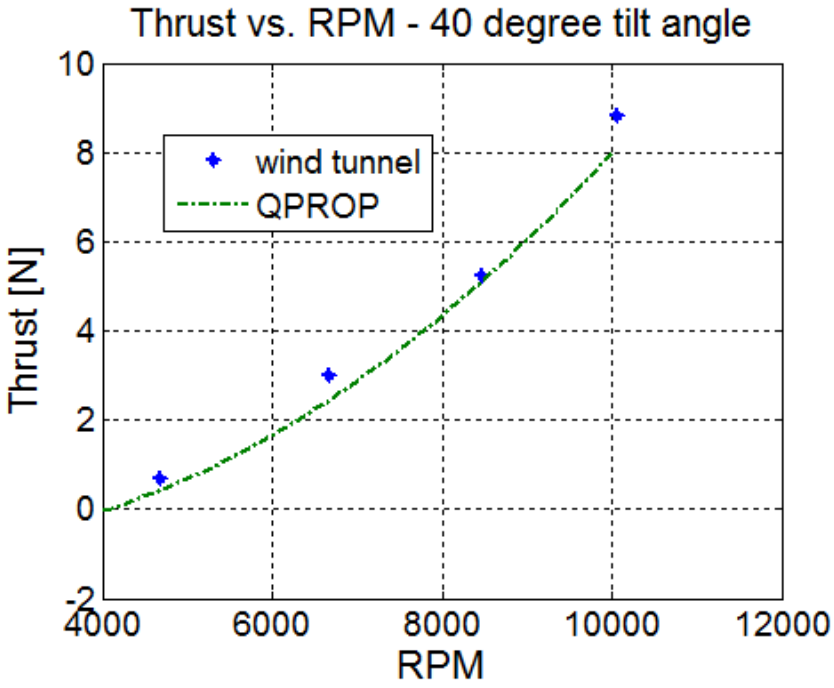

Figure 20 Comparison of Thrust [N] in QPROP with Experimental Data-at 15 m/s wind speed

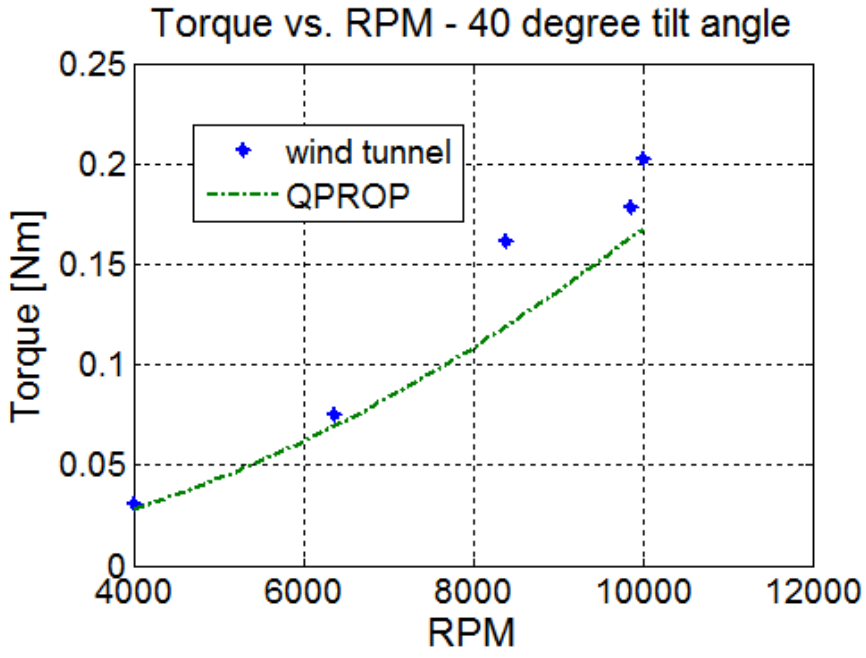

Figure 21 Comparison of Torque [Nm] in QPROP with Experimental Data-at 5 m/s wind speed

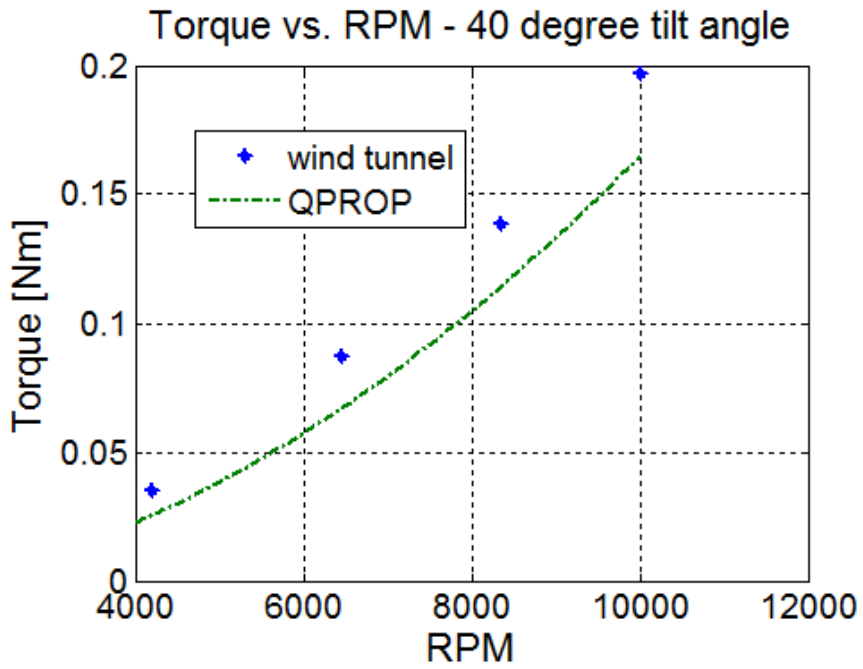

Figure 22 Comparison of Torque [Nm] in QPROP with Experimental Data-at 10 m/s wind speed

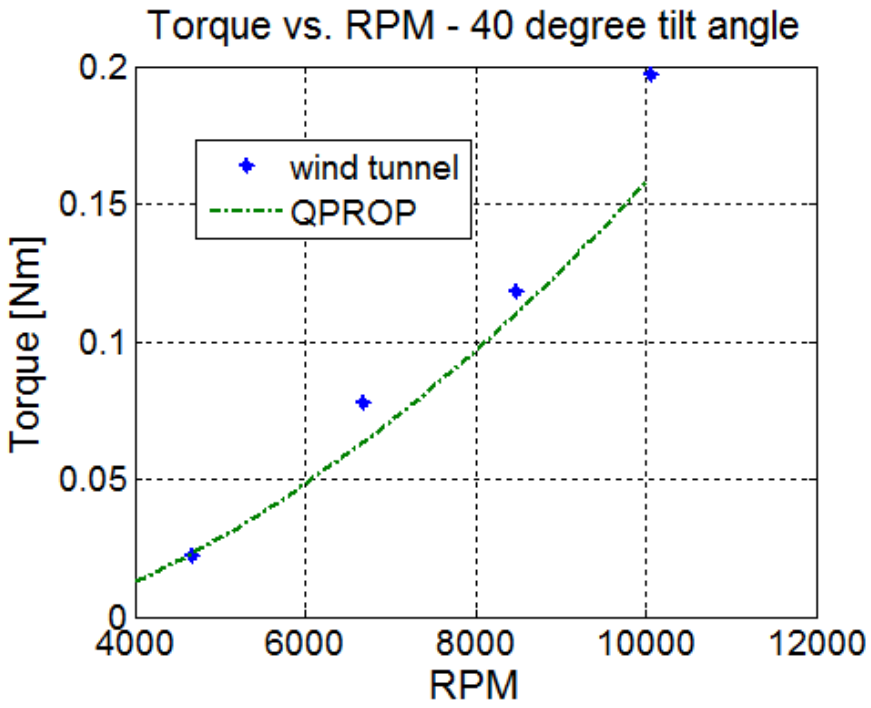

Figure 23 Comparison of Torque [Nm] in QPROP with Experimental Data-at 15 m/s wind speed

After verifying the results of the blade element formulation, the code is embedded into a function and used to find the thrust and torque values of the electric motor-propeller combination corresponding to different RPM values and axial velocities of the motor.

Throughout the study, due to the propulsive ineffectiveness and the inequality between three electric motors, the motor-propeller combination is revised. Three Axi 2826-10 electric motors and 11x4 wooden propellers are used. The geometric properties of 11x4 propeller are shown in Appendix A.

There are two more blocks in the propulsion subsystem block other than blade element formulation. One of them is used to convert the velocity of the air vehicle from body axis to the propeller axis to find the axial velocity facing each motor. The conversion is calculated from the body axis velocity of the aircraft and the tilt angles of the rotors.

The transformation matrix for front electric motors is shown in Eqn. (2) and for rear electric motor is shown in Eqn. (3).

$$T_1 = \begin{bmatrix} cos(90^o - \sigma) & 0 & -sin(90^o - \sigma) \\ 0 & 1 & 0 \\ sin(90^o - \sigma) & 0 & cos(90^o - \sigma) \end{bmatrix} \quad (2)$$

$$T_2 = \begin{bmatrix} 0 & 0 & -1 \\ sin(\delta) & cos(\delta) & 0 \\ cos(\delta) & -sin(\delta) & 0 \end{bmatrix} \quad (3)$$

The overall picture of the propulsion subsystem is shown in Figure 24.

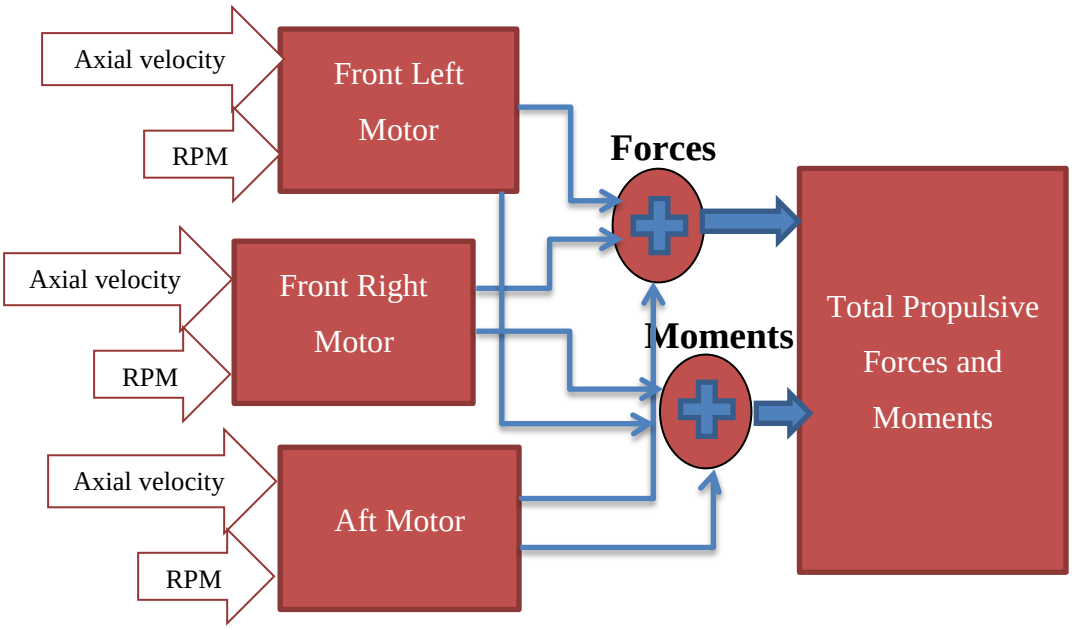

Figure 24 Propulsion System Model

3.1.3 Aerodynamics Model

The aerodynamics of the air vehicle is modeled for the transition and forward flight regimes. Aerodynamics model is obtained from the 3D Panel Method solutions. Panel method is based on incompressible potential flow field solutions. This method is most convenient for low speed aerodynamics with viscous effects neglected. The panel method is fast and solutions may be obtained for wide range of geometries rapidly. Potential flow is governed by Laplace's equation. Since, Laplace's equation is linear; superposition of several solutions may be used. The solutions that are used are source, doublet and vortex. The general solution is found by distributing source, doublet and vortex of unknown strength over discretized portions of the panels. Panels are created by dividing external surface of the geometry into smaller surfaces. The unknown strengths of the sources, doublets and vortex are found by solving a linear set of algebraic equations. [12] An open source 3D panel method code, XFLR5, is used to obtain solutions over the air vehicle. 3D Panel Method analysis is performed for the wing and tail separately. Analysis is

performed for different angles of attack, side slip angles and control surface deflections. It is assumed that the parameters do not change with the wind speed. The parameters used in the analysis are listed in Table 3 and Table 4 for the wing and the tail respectively. A sample solution for the wing and the tail are presented in Figure 25 and Figure 26 respectively.

Table 3 Input vectors for aerodynamic database – Wing

Parameter	Inputs
Control Surface Deflections (aileron)	$-20^o < \delta_{aileron} < 20^o$ $\Delta\delta_{aileron} = 10^o$
Angle of attack	$-16^o < \alpha < 16^o \quad \Delta\alpha = 2^o$
Beta	$-60^o < \beta < 60^o \quad \Delta\beta = 30^o$

Table 4 Input vectors for aerodynamic database – Tail

Parameter	Inputs
Control Surface Deflections (elevator)	$-20^o < \delta_{elev} < 20^o$ $\Delta\delta_{elev} = 10^o$
Control Surface Deflections (rudder)	$-20^o < \delta_{rudder} < 20^o$ $\Delta\delta_{rudder} = 10^o$
Angle of attack	$-16^o < \alpha < 16^o \quad \Delta\alpha = 2^o$
Beta	$-60^o < \beta < 60^o \quad \Delta\beta = 30^o$

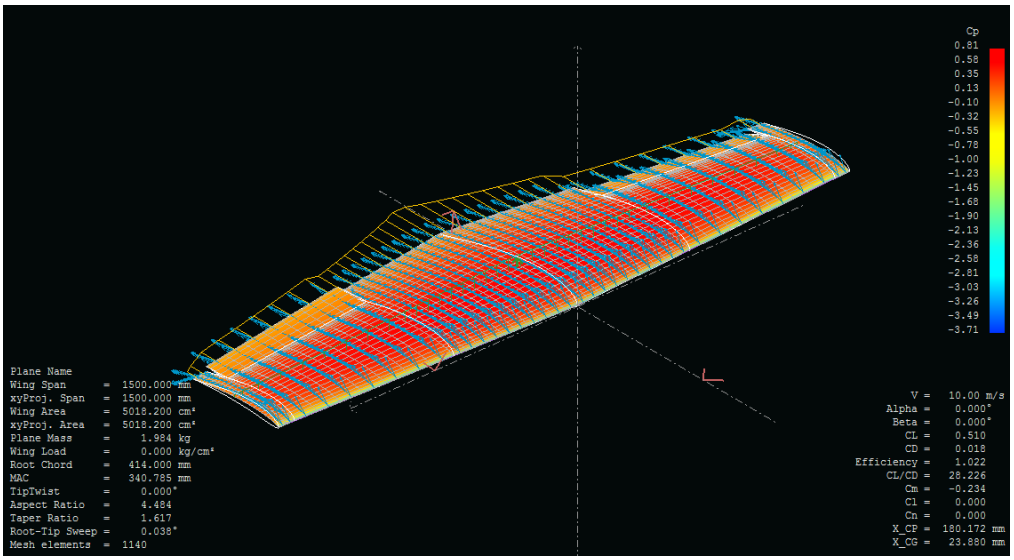

Figure 25 3D Panel Method Solution for Wing

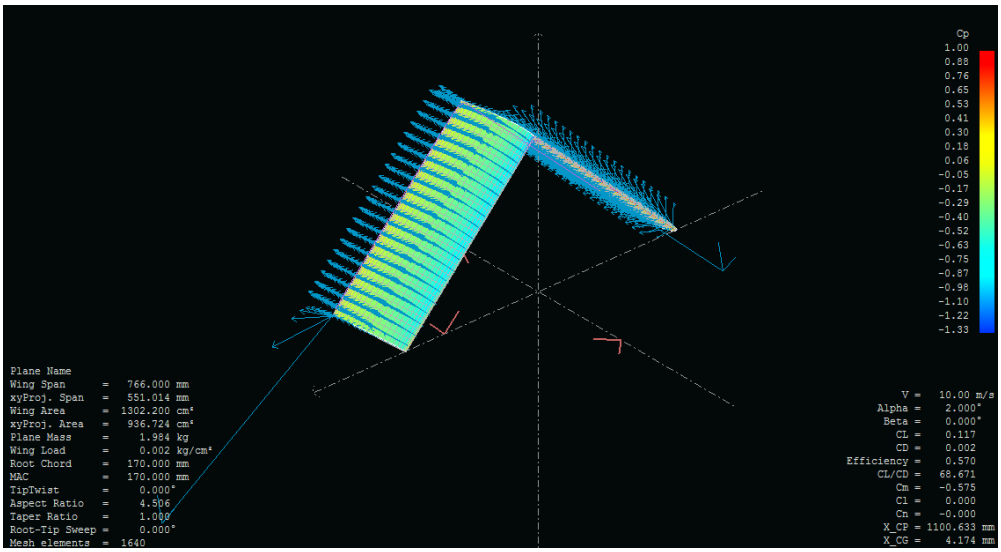

Figure 26 3D Panel Method Solution for Tail

Aerodynamic coefficients for the wing and tail shown in Table 5 are tabulated corresponding to the input values given in Table 3 and Table 4.

Table 5 Aerodynamic Coefficients

Aerodynamic Coefficients
$C_L, C_D, C_Y, C_l, C_m, C_n$

In order to improve the lateral stability, the variation of the rolling moment with the roll rate, and the variation of the yawing moment with the yaw rate are also added into the aerodynamic coefficient calculations. [13]
Hence, the aerodynamic coefficients are estimated in the model as given in Eqn. (4)-Eqn. (9).

$$C_L = C_{L_\alpha}\alpha + C_{L_\beta}\beta + C_{L_{\delta a}}\delta a + C_{L_{\delta e}}\delta e \tag{4}$$

$$C_D = C_{D_\alpha}\alpha + C_{D_\beta}\beta + C_{D_{\delta a}}\delta a + C_{D_{\delta e}}\delta e + C_{D_{\delta r}}\delta r \tag{5}$$

$$C_Y = C_{Y_\alpha}\alpha + C_{Y_\beta}\beta + C_{Y_{\delta a}}\delta a + C_{Y_{\delta r}}\delta r \tag{6}$$

$$C_l = C_{l_\alpha}\alpha + C_{L_\beta}\beta + C_{l_{\delta a}}\delta a + C_{l_{\delta r}}\delta r + C_{l_p}p \tag{7}$$

$$C_m = C_{m_\alpha}\alpha + C_{m_\beta}\beta + C_{m_{\delta a}}\delta a + C_{m_{\delta e}}\delta e \tag{8}$$

$$C_n = C_{n_\alpha}\alpha + C_{n_\beta}\beta + C_{n_{\delta a}}\delta a + C_{n_{\delta r}}\delta r + C_{n_r}r \tag{9}$$

By using aerodynamic coefficients a database is created and interpolation tables are used in MATLAB/Simulink. For the wing, a three dimensional interpolation table is used, whereas for the tail a four dimensional table is used that there is an additional control surface is taken into consideration. In total, thirty six tables are formed and part of the database is given as an example in Appendix B.

Local velocity of the wing and tail are calculated by adding the body velocity of the aircraft and the effect of the angular speed. The angular velocity of the aircraft is multiplied with the distance between the center of gravity of the aircraft and the aerodynamic center of the wing and tail.

After estimating the local velocities, forces and moments are estimated for wing and tail separately and summed up.

The overall aerodynamic model is shown in Figure 27.

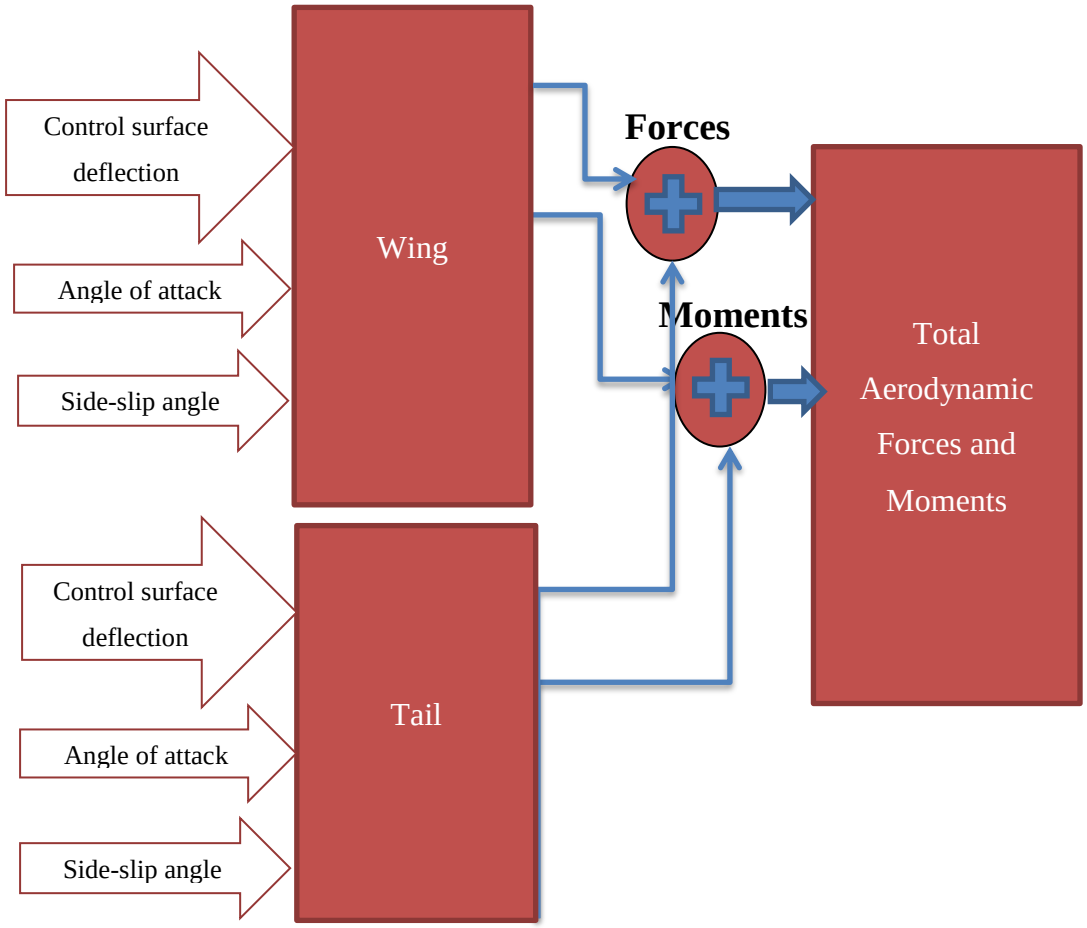

Figure 27 Aerodynamics Model

3.1.4 Gravity Model

Gravity model simply transforms the gravitational effect to the body axis frame by using Eqn. (10).

$$X_g = -mgsin\theta \quad Y_g = mgcos\theta sin\phi \quad Z_g = mgcos\theta cos\phi \tag{10}$$

The output forces of the model are directly added to the 6-DoF flight dynamics model.

3.1.5 6-DoF Flight Dynamics Model

6 DoF Flight Dynamics Model calculates the Euler angles, angular velocity, angular acceleration, position, velocity, acceleration of the aircraft by integrating the 6 DoF equations of motion in body axis. The motion of the air vehicle in both Body and Earth Fixed Frames are obtained.

Before introducing the general equations of motion, the axes transformations used in the model should be defined.

3.1.6.1. Axes Definitions

Inertial Axis System: A non-rotating reference system that has the origin at the center of the Earth.

Earth-Fixed Axis system: Defined by the axes along the Earth‘s polar axis. The Earth axis is rotating due to the Inertial frame with the rotational speed of the Earth.

Navigational System (NED): Located on the surface of the Earth such that the z axis is directed towards the center of the spherical Earth. Axes are all aligned with the directions of north, east and local vertical (down)

Body-Fixed Axis System: Is an orthogonal axis system centered at generally the center of gravity location fixed to the vehicle and aligned with the roll, pitch, yaw axes of the vehicle in which the navigation system is installed.

Wind Coordinate System: Has the origin at the center of gravity of the air vehicle where the x-axis is aligned with the velocity vector. The horizontal and lateral axes are defined in the perpendicular directions. Angle of attack and side-slip angle defines the orientation of the wind coordinate system. [14] The axes systems are shown in Figure 28.

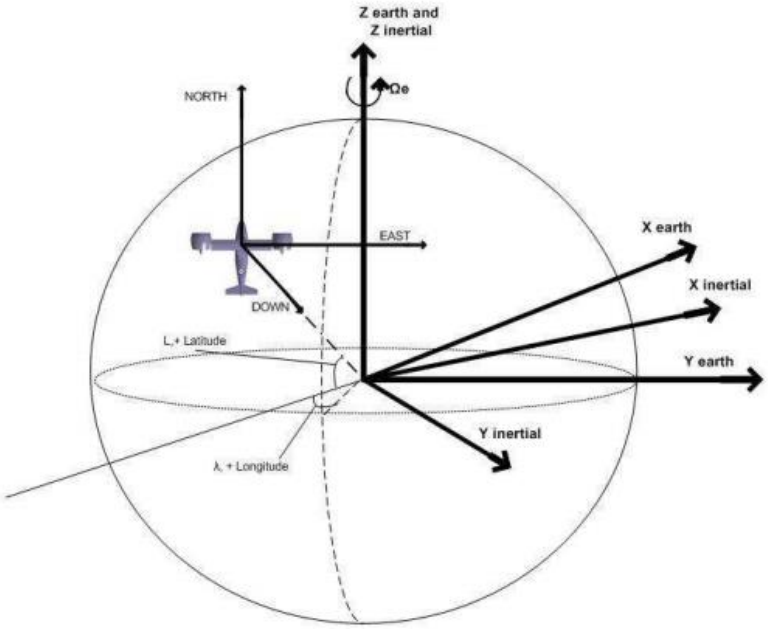

Figure 28 Inertial-Earth-Navigational axes systems [14]

3.1.6.2. Axes Transformations

Body-Fixed to Earth Axis

The transformation from body fixed axis system to earth axis system is done by taking the transpose of the Direction Cosine Matrix (DCM) which is a 3x3 matrix, the columns of which represent unit vectors in body axes projected along the reference axis. In DCM approach the transformation from one coordinate frame to another is defined by three rotations about different axes taken in turn which is shown in Figure 29. The Euler angles usage for the transformation is the most popular and simple technique to define the airplane motion relative to the Earth. [15] The transformation matrices are shown in Eqn.(11), Eqn. (12) and Eqn. (13).

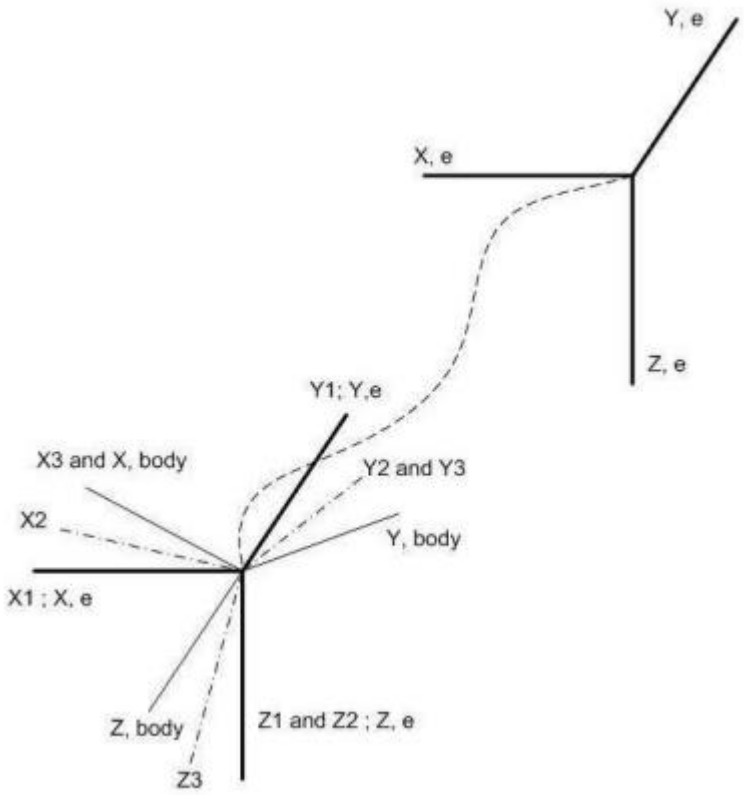

Figure 29 Euler Transformation

$$\begin{bmatrix} u \\ v \\ w \end{bmatrix}^E = DCM^T \begin{bmatrix} u \\ v \\ w \end{bmatrix}^B \tag{11}$$

$$DCM^T = \begin{bmatrix} c\psi & s\psi & 0 \\ -s\psi & c\psi & 0 \\ 0 & 0 & 1 \end{bmatrix} \begin{bmatrix} c\,\theta & 0 & -s\,\theta \\ 0 & 1 & 0 \\ s\,\theta & 0 & c\,\theta \end{bmatrix} \begin{bmatrix} 1 & 0 & 0 \\ 0 & c\,\phi & -s\,\phi \\ 0 & -s\,\phi & c\,\phi \end{bmatrix} \tag{12}$$

$$V^E = \begin{bmatrix} c\psi\, c\,\theta & -c\,\phi s\psi + s\,\phi\, s\,\theta c\psi & s\,\phi\, s\psi + c\,\phi\, s\,\theta c\psi \\ c\,\theta s\psi & c\,\phi c\psi + s\,\phi\, s\,\theta\, s\psi & s\,\phi c\psi + s\,\phi\, s\,\theta\, s\psi \\ -s\,\theta & s\,\phi\, c\,\theta & c\,\phi\, c\,\theta \end{bmatrix} V^B \tag{13}$$

where, “s” stands for sine and “c” stands for cosine trigonometric functions.

Wind Axis to Body-Fixed Axis

The orientation of the wind coordinate system is defined by the angle of attack and sideslip angle with respect to the body-fixed axis system that is shown in Figure 30. Hence, the transformation from wind axis to body-fixed axis is done with these angles as shown in Eqn. (14).

$$\begin{bmatrix} u \\ v \\ w \end{bmatrix} = \begin{bmatrix} cos\alpha\, cos\,\beta \\ sin\alpha \\ sin\alpha\, cos\,\beta \end{bmatrix} V^W \tag{14}$$

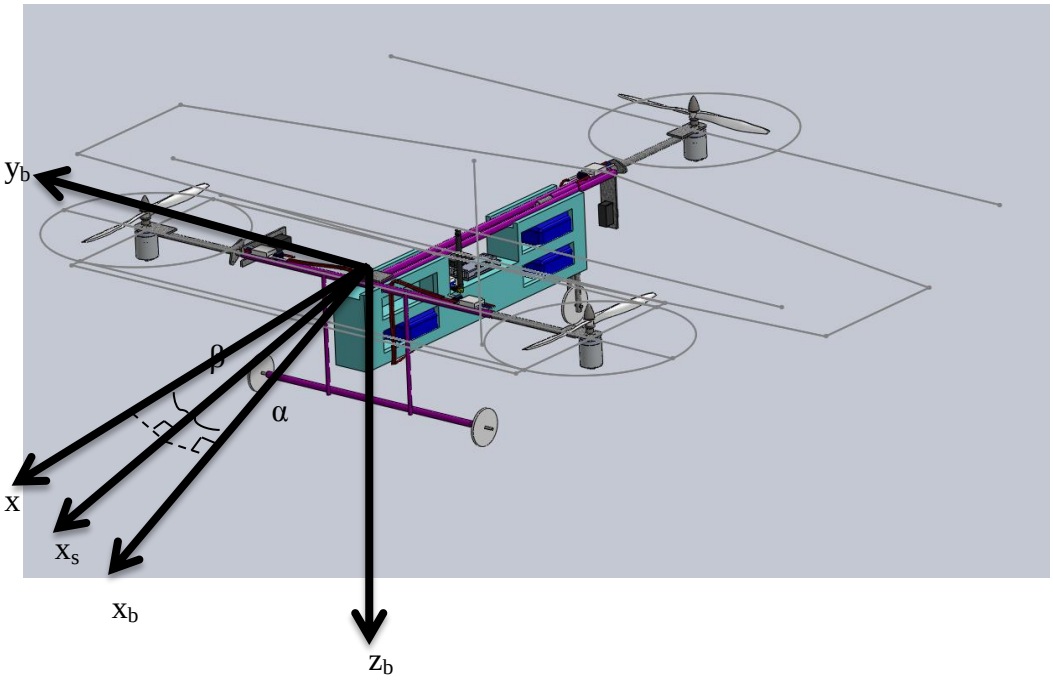

Figure 30 Stability-Wind and Body Fixed Axes Transformation

3.1.6.3. General Equations of Motion

6 DoF equations of motion are derived from Newton's law of motion for translational dynamics Eqn. (15) and Euler's law of motion for rotational dynamics Eqn. (16).

$$\sum \vec{F} = m\frac{\overrightarrow{dV}}{\overrightarrow{dt}} \tag{15}$$

$$\sum \vec{M} = I\frac{\overrightarrow{dH}}{\overrightarrow{dt}} \tag{16}$$

where, $\sum \vec{F}$ are the total external forces and $\sum \vec{M}$ are the total external moments acting on the system. $\frac{\overrightarrow{dV}}{\overrightarrow{dt}}$ is the change in translational speed and $\frac{\overrightarrow{dH}}{\overrightarrow{dt}}$ is the change in angular momentum. m is the mass of the air vehicle.

6 DoF equations of motion are derived as follows: [13]

$$\dot{u} = {}^{X}/_{m} - g\,sin\,\theta + rv + qw \tag{17}$$

$$\dot{v} = {}^{Y}/_{m} + g\,cos\,\theta\,sin\,\phi - ru + pw \tag{18}$$

$$\dot{w} = {}^{Z}/_{m} + g\,cos\,\theta\,cos\,\phi + qu - pv \tag{19}$$

$$\dot{p} = \frac{\left(I_{zz}L + I_{xz}N - \left\{I_{xz}\left(I_{yy} - I_{xx} - I_{zz}\right)p + \left[I_{xz}^2 + I_{zz}\left(I_{zz} - I_{yy}\right)\right]r\right\}q\right)}{(I_{xx}I_{zz} - I_{xz}^2)} \tag{20}$$

$$\dot{q} = \frac{1}{I_{yy}}[M - (I_{xx} - I_{zz})pr - I_{xz}(p^2 - r^2)] \tag{21}$$

$$\dot{r} = \frac{\left(I_{xz}L + I_{xx}N - \left\{I_{xz}\left(I_{yy} - I_{xx} - I_{zz}\right)r + \left[I_{xz}^2 + I_{xx}\left(I_{xx} - I_{yy}\right)\right]p\right\}q\right)}{(I_{xx}I_{zz} - I_{xz}^2)} \tag{22}$$

The kinematic equations are given as follows:

$$\dot{\phi} = p + q\tan\theta\sin\phi + r\tan\theta\cos\phi \tag{23}$$

$$\dot{\theta} = q\cos\phi - r\sin\phi \tag{24}$$

$$\dot{\psi} = q\sec\theta\sin\phi + r\sec\theta\cos\phi \tag{25}$$

The navigational equations are given as follows:

$$\dot{x} = u\,c\,\psi\,c\,\theta + v(-s\,\psi\,c\,\phi + c\,\phi\,s\,\theta\,s\,\phi) + w(s\,\psi\,s\,\phi + c\,\psi\,s\,\theta\,c\,\phi) \tag{26}$$

$$\dot{y} = u\,s\,\psi\,c\,\theta + v\,(c\,\psi\,c\,\phi + s\,\psi\,s\,\theta\,s\,\phi) + w(-c\,\psi\,s\,\phi + s\,\psi\,s\,\theta\,c\,\phi) \tag{27}$$

$$\dot{z} = -u\,s\,\theta + v(c\,\theta\,s\,\phi) + w(c\,\theta\,c\,\phi) \tag{28}$$

where, "s" stands for sine and "c" stands for cosine trigonometric functions $\begin{bmatrix} X \\ Y \\ Z \end{bmatrix}$ and $\begin{bmatrix} L \\ M \\ N \end{bmatrix}$ are the resultant aerodynamic and propulsive force and moment vectors acting on the air vehicle center of gravity expressed in the body coordinate frame respectively. It is assumed that gravitational acceleration, g in the equations do not vary and are constant.

$$X = X_a + X_t + X_{other} \tag{29}$$

$$Y = Y_a + Y_t + Y_{other} \tag{30}$$

$$Z = Z_a + Z_t + Z_{other} \tag{31}$$

where subscripts "a" and "t" stands for the aerodynamic and propulsive forces respectively. Subscript "other" stands for the forces that cannot be predicted in advance.

$$X_t = (T_1 + T_2)\sin(-\sigma) \tag{32}$$

$$Y_t = (T_3)\sin\delta \tag{33}$$

$$Z_t = -(T_1 + T_2)\cos\sigma - (T_3)\cos\delta \tag{34}$$

where, T_1, T_2 and T_3 are the thrust forces of the front left, front right and aft electric motors respectively. σ is the tilt angle of the front motors around pitch axis. δ is the tilt angle of the aft motor around roll axis. σ is taken to be zero when the front electric motors are positioned vertically and is taken as positive when the electric motors are turning to level position.

$$L = L_a + L_t + L_{other} \tag{35}$$

$$M = M_a + M_t + M_{other} \tag{36}$$

$$N = N_a + N_t + N_{other} \tag{37}$$

$$L_t = (T_1 - T_2)\cos\sigma r_y + (T_3)\sin\delta r_z^{aft} + (Q_2 - Q_1)\sin(-\sigma) \tag{38}$$

$$M_t = (T_1 + T_2)\cos\sigma r_x - (T_3)\cos\delta r_x^{aft} - (T_1 + T_2)\sin(-\sigma)\, r_z - (Q_3)\sin\delta \tag{39}$$

$$N_t = (T_1 - T_2)\sin(-\sigma)\, r_x - (T_3)\sin\delta r_x^{aft} + (Q_2 - Q_1)\cos\sigma + (Q_3)\cos\delta \tag{40}$$

where, Q_1, Q_2 and Q_3 are the reactive torque values of the front left, front right and aft electric motor respectively. “Subscript “other” stands for the moments that cannot be predicted in advance. r_x, r_y, r_z are the distances between the front electric motors and the air vehicle center of gravity in x, y and z axis respectively. r_x^{aft} *and* r_z^{aft} are the distances between the aft electric motor and air vehicle center of gravity in x and

z axis respectively. All electric motors are above the center of gravity location in z-axis.

The dominant forces and moments are coming from propulsion system in hover. If the tilt angle of the aft electric motor is taken as zero, the reactive torque value of the aft electric motor should be equal to the difference between the reactive torque values of the first and second electric motors in order to compensate the yawing moment. However, if the tilt angle of the aft electric motor is increased, it results in a rolling moment. Hence, the controller that is to be designed should be able to regulate the torque values of the three motors by changing the rpm values and the tilt angle of the aft motor at the same time in hover position.

3.2 Model Inputs, Outputs and States

The inputs, outputs and states of the model are shown below.

Inputs of the model :

Throttle rate for the maximum allowable thrust of front left electric motor [%]: δ_{th1}

Throttle rate for the maximum allowable thrust of front right electric motor [%]: δ_{th2}

Throttle rate for the maximum allowable thrust of aft electric motor [%]: δ_{th3}

Tilt angle for the front electric motor [rad] : σ

Tilt angle for the aft electric motor [rad] : δ

Deflection of the elevator [rad] : δ_{elev}

Deflection of the aileron [rad] : δ_{aile}

Deflection of the rudder [rad] : δ_{rud}

Outputs of the model :

Velocity vector components in Earth fixed Frame : V_x^E, V_y^E, V_z^E

Velocity vector components in Body Frame: u, v, w

Angular acceleration components in Body Frame: $\dot{p}, \dot{q}, \dot{r}$

Translational acceleration components in Body Frame: $\dot{u}, \dot{v}, \dot{w}$

Rotational velocity components in Body Frame : p, q, r

Euler angles : ϕ, θ, φ

Positions in Earth Frame : X^E, Y^E, Z^E

States of the model :

Euler angles : ϕ, θ, φ

Angular velocity components in Body Frame : p, q, r

Velocity vector components in Body Frame: u, v, w

Positions in Earth fixed Frame : X^E, Y^E, Z^E

CHAPTER 4

TRIMMING AND LINEARIZATION

This chapter is about the linearization process of the nonlinear model that is explained in the previous chapter. The linearization is essential in order to determine the stability characteristics of the system, and then to design linear controllers.

The linearization of the nonlinear dynamic systems is done around specific local equilibrium points by using the equations of motion of the relevant system. Trimming is to find the equilibrium points about which the linearization of the relevant nonlinear equations is done.

Throughout the chapter, trimming methods and trim points of the system and the linearization method for the nonlinear air vehicle model is explained. The trim points that are found in this chapter are used in linear model analysis and control design in the following chapter.

4.1 Trimming Methodology

Trimming is done with the help of MATLAB/Simulink Linear Analysis Toolbox. Nonlinear least squares optimization method is used with Levenberg-Marquardt algorithm. Nonlinear least squares methods involve an iterative improvement to parameter values in order to reduce the sum of the squares of the errors between the function and the measured data points. The Levenberg-Marquardt curve-fitting method is actually a combination of two minimization methods: the gradient descent

method and the Gauss-Newton method. In the gradient descent method, the sum of the squared errors is reduced by updating the parameters in the direction of the greatest reduction of the least squares objective. In the Gauss-Newton method, the sum of the squared errors is reduced by assuming the least squares function is locally quadratic, and finding the minimum of the quadratic. The Levenberg-Marquardt method acts more like a gradient-descent method when the parameter are far from their optimal value and acts more like the Gauss-Newton method when the parameters are close to their optimal value [15].

The number of iterations, function evaluations, parameter and function tolerances are all selectable to reach the required equilibrium states, inputs and outputs.

4.1.1 Trimming Specifications

In trimmed flight, the air vehicle is defined to have zero angular and translational acceleration and constant control inputs.

$$\dot{p} = \dot{q} = \dot{r} = \dot{u} = \dot{v} = \dot{w} = 0 \tag{41}$$

4.1.2 Trim Results

After the iterative solution, the trimming results are obtained with maximum error in the order of 10^{-12}. For hover, the aircraft has a zero velocity in trim, whereas for forward flight the trim results are presented for different velocities. The results are shown in Table 6 for hover and in Table 7 for forward flight.

Table 6 Trim results for hover

$V\ (m/s)$	δ_{th1} (%)	δ_{th2} (%)	δ_{th3} (%)	$\delta\ (rad)$
0	88.6098	73.553	81.1803	0.0400

Table 7 Trim results for forward flight

$V(m/s)$	δ_{th} (%)	$u\,(m/s)$	$w\,(m/s)$	δ_{elev} (deg)	$\theta\,(deg)$
10	59.39	10.70	1.11	2.65	3.27
11	59.22	11.44	0.91	2.48	2.75
12	59.15	12.23	0.71	2.28	2.18
13	59.26	13.10	0.50	2.05	1.55
14	59.01	14.03	0.26	1.84	0.86
15	58.84	14.99	0.03	1.63	0.11
16	58.75	15.99	-0.18	1.77	-0.63
17	58.84	16.99	-0.40	1.63	-1.31
18	59.40	17.98	-0.61	1.49	-1.95
19	62.12	18.94	-0.75	1.82	-2.29
20	64.52	19.92	-0.93	1.75	-2.69
21	67.92	20.86	-1.08	1.85	-2.86
22	73.88	21.42	-1.06	2.69	-2.23
23	77.90	22.31	-1.2	2.55	-2.18
24	82.04	23.25	-1.37	2.34	-2.18

The trim point corresponding to the cruise speed of the aircraft that is 15 m/s is used in linearizing the system.

4.2 Linearization

4.2.1 Linearization Methodology

While linearizing the nonlinear model, MATLAB/Simulink Linear Analyses Toolbox is used. The inputs and outputs of the model that are stated in 3.2 are used for the analysis inputs and outputs and the trim point that is found in the previous part is used as an operating point. Numerical perturbation is used as a linearization

algorithm and ‘linoptions’ is the command that is used to define in the MATLAB code. After defining the type of the algorithm, ‘linearize’ command is used to linearize the system around the specified operating point.

The system is linearized around that operating point with the classical Taylor series approach and after linearizing the 6 DoF equations of motion, a continuous time state-space model is obtained as shown through (42) and (49).

$$\dot{x} = f(x,u) \tag{42}$$

$$y = g(x,u) \tag{43}$$

$$A = \left.\frac{\partial f}{\partial x}\right|_{(x_0,u_0)} = \begin{bmatrix} \left.\frac{\partial f_1}{\partial x_1}\right|_{(x_0,u_0)} & \cdots & \left.\frac{\partial f_1}{\partial x_n}\right|_{(x_0,u_0)} \\ \cdots & \cdots & \cdots \\ \left.\frac{\partial f_n}{\partial x_1}\right|_{(x_0,u_0)} & \cdots & \left.\frac{\partial f_n}{\partial x_n}\right|_{(x_0,u_0)} \end{bmatrix} \tag{44}$$

$$B = \left.\frac{\partial f}{\partial u}\right|_{(x_0,u_0)} = \begin{bmatrix} \left.\frac{\partial f_1}{\partial u_1}\right|_{(x_0,u_0)} & \cdots & \left.\frac{\partial f_1}{\partial u_m}\right|_{(x_0,u_0)} \\ \cdots & \cdots & \cdots \\ \left.\frac{\partial f_n}{\partial u_1}\right|_{(x_0,u_0)} & \cdots & \left.\frac{\partial f_n}{\partial u_m}\right|_{(x_0,u_0)} \end{bmatrix} \tag{45}$$

$$C = \left.\frac{\partial g}{\partial x}\right|_{(x_0,u_0)} = \begin{bmatrix} \left.\frac{\partial g_1}{\partial x_1}\right|_{(x_0,u_0)} & \cdots & \left.\frac{\partial g_1}{\partial x_n}\right|_{(x_0,u_0)} \\ \cdots & \cdots & \cdots \\ \left.\frac{\partial g_n}{\partial x_1}\right|_{(x_0,u_0)} & \cdots & \left.\frac{\partial g_n}{\partial x_n}\right|_{(x_0,u_0)} \end{bmatrix} \tag{46}$$

$$D = \left.\frac{\partial g}{\partial u}\right|_{(x_0,u_0)} = \begin{bmatrix} \left.\frac{\partial g_1}{\partial u_1}\right|_{(x_0,u_0)} & \cdots & \left.\frac{\partial g_1}{\partial u_m}\right|_{(x_0,u_0)} \\ \cdots & \cdots & \cdots \\ \left.\frac{\partial g_n}{\partial u_1}\right|_{(x_0,u_0)} & \cdots & \left.\frac{\partial g_n}{\partial u_m}\right|_{(x_0,u_0)} \end{bmatrix} \tag{47}$$

$$\dot{\Delta x} = A\Delta x + B\Delta u \tag{48}$$

$$\Delta y = C\Delta x + D\Delta u \tag{49}$$

4.2.2 Linearization Results

The matrices obtained after linearizing at trim values of Table 6 and Table 7 are given in Appendix C.

CHAPTER 5

CONTROLLER DESIGN

5.1 Concept of Operations (CONOPS)

The concept of operations defines the specifications of flight. The air vehicle that is studied has mainly three flight phases that are hover, transition and forward flight phase. In all phases, the pilot can transmit commands to the air vehicle via remote controller and the controller inside the board in the air vehicle stabilizes the states of the system. This type of flight is named as pilot in the loop structure. In this thesis, hover and forward flight cases are studied.

5.1.1 Hover Case

In hover case the pilot has four inputs in the remote controller that are the throttle, pitch, roll and yaw inputs. As it can be seen in Figure 31, by using the throttle command stick the pilot can take-off, land or increase/decrease altitude during hover. By using the pitch command stick, the pilot can make pitch up or down. By using the roll command stick the pilot can make rolling motion. Lastly, by using the yaw command stick, the pilot can change the heading of the air vehicle. [16]

Figure 31 Remote Controller for Hover

The commands of the pilot are taken as angle commands and the error between the Euler angles and the pilot commands are used in the controller. The controller gives four inputs to the air vehicle that are the throttle values of the electric motors and the angle of the aft electric motor. The control surfaces are not effective in this phase.

The schematic is shown in Figure 32.

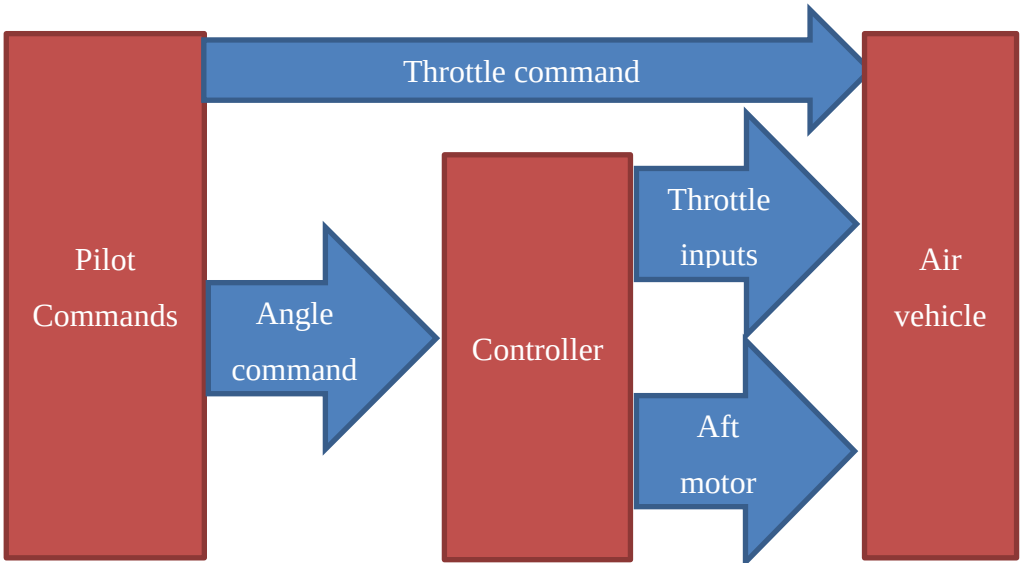

Figure 32 Control Schematic in Hover

5.1.2 Forward Flight Case

In forward flight case the pilot has four inputs in the remote controller that are the throttle, pitch, roll and yaw inputs. As it can be seen in Figure 33, by using the throttle command stick the pilot can increase/decrease forward speed during forward flight. By using the pitch command stick, the pilot can make pitch up or down. By using the roll command stick the pilot can make rolling motion. Lastly, by using the yaw command stick, the pilot can change the heading of the air vehicle.

Figure 33 Remote Controller for Forward Flight

The commands of the pilot are taken as angle commands and the error between the Euler angles and the pilot commands are used in the controller as in the hover case. The controller gives four inputs to the air vehicle that are the throttle value of the front electric motors and control surface deflections namely, aileron, elevator and rudder. The differential thrust control is not present in this phase. Unlike hover control, the heading input of the pilot is given directly in forward flight. That is, the heading angle is no controlled in forward flight.

The schematic is shown in Figure 34.

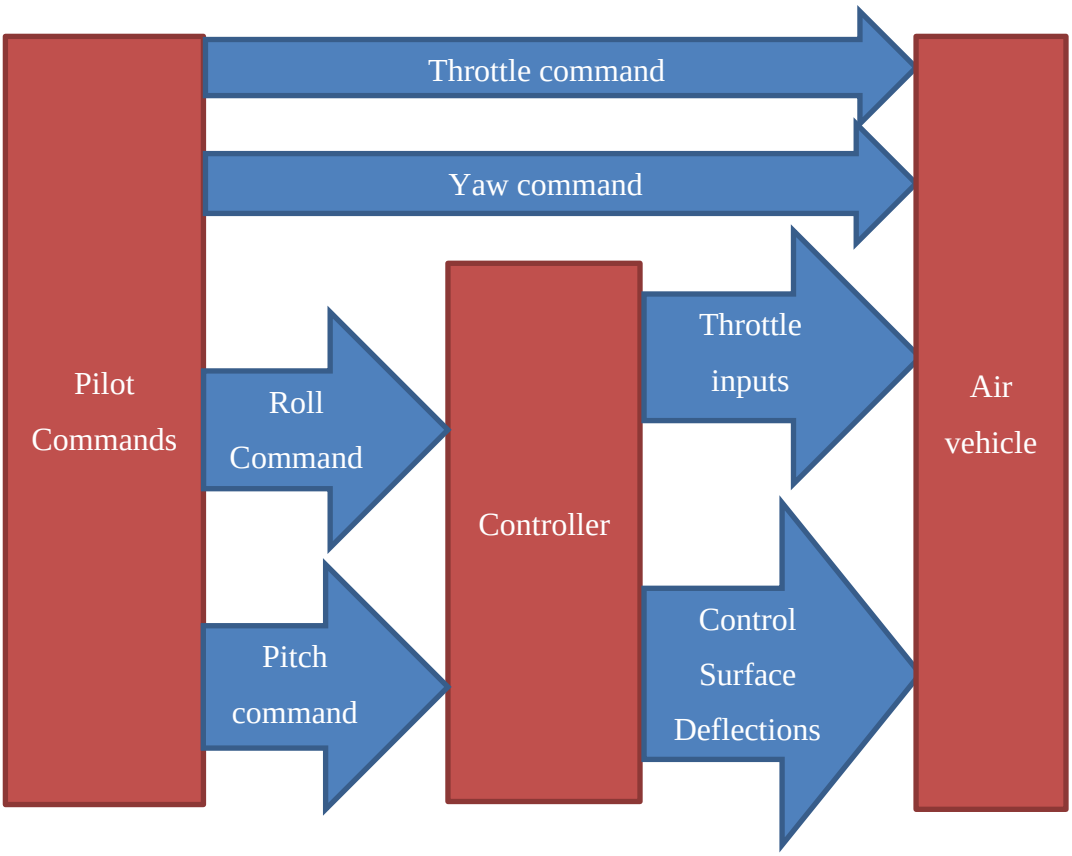

Figure 34 Control Schematic in Forward Flight

5.2 Controller

5.2.1 Linear System Specifications

As explained in the previous chapter, the linear system matrices are obtained. In linear controller design phase, the system matrices are simplified and 6 states are used instead of 12 in hover flight, and 5 states are used in the forward flight. The controlled states are given in Table 8 and Table 9 for hover and forward flight respectively.

Table 8 Hover Flight – Controlled States

p	q	r	ϕ	θ	φ

Table 9 Forward Flight – Controlled States

p	q	r	ϕ	θ

Correspondingly, the system matrices are reduced to A_{sys} [6X6] and B_{sys} [6X4] for hover and A_{sys} [5X5] and B_{sys} [5X4] for forward flight respectively that are shown in Appendix C.

The controller configuration is shown in Figure 35.

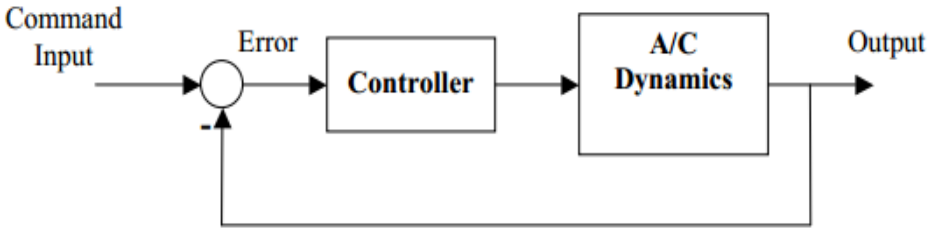

Figure 35 Controller Configuration

5.2.2 Stability Characteristics

Before designing a controller, the stability characteristics of the system should be observed, in addition with the controllability.

In order to determine the stability characteristics, the eigenvalues of the system matrix are observed for both hover and forward flight phase. It is seen that, the system has unstable poles in hover Eqn. (50). This stems from the fact that there is no damping effect in hover unlike the forward flight. In order to compare the simulation results with the flight test results the inertial and aerodynamic effects of

the wing and tail are not included in hover because the flight tests that are mentioned in Chapter 7 are performed without the wing and tail.

$$
\begin{aligned}
\mathrm{e}ig(Asys)_{hover} &= 10^{-7}\begin{bmatrix} 0 \\ -0.0015 + 0.1350i \\ -0.0015 - 0.1350i \\ 0.0000 \\ -0.0000 + 0.0000i \\ -0.0000 - 0.0000i \end{bmatrix} \\
\mathrm{e}ig(Asys)_{forward\ flight} &= \begin{bmatrix} -10.0119 \\ -2.3104 \\ -5.3069 \\ -0.0000 + 0.0000i \\ -0.0000 - 0.0000i \end{bmatrix}
\end{aligned}
\tag{50}
$$

5.2.3 Controllability

Controllability of an LTI system measures the capability of an external input to move the internal state of a system from any initial state to any other final state in a finite time interval. [17] Since the controllability matrix has full row rank, the system is controllable.

5.2.4 Linear Quadratic (LQ) Problem

The case where the system dynamics are described by a set of linear differential equations and the cost is described by a quadratic function is called “LQ problem”. [18] The solution to this problem is the state feedback controller. The linearized system that is explained in the previous chapter is reduced from 12 states to 6 states that are the angular rates and Euler angles for hover. The pilot’s commands are taken as angle commands and pass through the controller before actuating the air vehicle. Unlike hover, the system is reduced from 12 states to 5 states that are the angular rates, roll and pitch angles in forward flight because the heading angle is not controlled and the pilot yaw command is given directly to the actuator. Roll and pitch commands are given as angle commands and pass through the controller before actuating the system.

5.2.4.1. Linear Quadratic Regulator (LQR)

In LQR, the cost function is the weighted sum of the squares of states and inputs as given in Eqn. (51).

$$J = \frac{1}{2}\int_0^\infty \left(x(t)^T Q x(t) + u(t)^T R u(t)\right) dt \tag{51}$$

where, Q and R are state and control weighting matrices respectively.

Selection of the weighting matrices, Bryson's approach is employed. [19]

$$Q_{ii} = \frac{1}{maximum\ acceptable\ value\ of x_i^2} \tag{52}$$

$$R_{ii} = \frac{1}{maximum\ acceptable\ value\ of u_i^2} \tag{53}$$

For hover case, the maximum acceptable value of the states are taken as 90 deg/sec for angular rates and 90 deg for Euler angles. The maximum acceptable value of the throttle inputs is taken as 40% and 90 deg for aft motor angle.

For forward flight case, the maximum acceptable value of the states are taken as 90 deg/sec for angular rates and 90 deg for Euler angles. The maximum acceptable value of the throttle input is taken as 40% and 20 deg for control surface deflections. These values are selected after a trial-and-error process.
Q and R matrices are estimated accordingly for hover and forward flight cases and given in Appendix D.

The solution of the LQ problem is formed from the algebraic Riccati equation given in Eqn. (54). The state feedback gain matrix is given in Eqn. (55).

$$A_{sys}{}^{T}S + SA_{sys} - SB_{sys}R^{-1}B_{sys}{}^{T}S + Q = 0 \tag{54}$$

$$K = R^{-1}B_{sys}{}^{T}S \tag{55}$$

The gain matrices for hover and forward flight are shown in Appendix D.

The reduced form is shown in Eqn. (56) for the hover phase.

$$\begin{bmatrix} \dot{p} \\ \dot{q} \\ \dot{r} \\ \dot{\phi} \\ \dot{\theta} \\ \dot{\varphi} \end{bmatrix} = [A_{sys}] \begin{bmatrix} p \\ q \\ r \\ \phi \\ \theta \\ \varphi \end{bmatrix} + [B_{sys}] \begin{bmatrix} \delta_{th1} \\ \delta_{th2} \\ \delta_{th3} \\ \delta_{aft} \end{bmatrix} \tag{56}$$

The closed loop system is presented in Eqn. (57).

$$\begin{bmatrix} \dot{p} \\ \dot{q} \\ \dot{r} \\ \dot{\phi} \\ \dot{\theta} \\ \dot{\varphi} \end{bmatrix} = [A_{sys} - B_{sys}K] \begin{bmatrix} p \\ q \\ r \\ \phi \\ \theta \\ \varphi \end{bmatrix} + [B_{sys}K] \begin{bmatrix} 0 \\ 0 \\ 0 \\ \phi_{com} \\ \theta_{com} \\ \varphi_{com} \end{bmatrix} \tag{57}$$

K is the gain matrix that is already obtained from the Ricatti equation solution, and ϕ_{com}, θ_{com} and φ_{com} are the pilot commands. The eigenvalues of the closed loop system matrix is shown in Eqn. (58).

$$\mathrm{e}ig\left(A_{closed\ loop}\right) = \begin{bmatrix} -25.2602 \\ -21.4266 \\ -9.6712 \\ -1.0054 \\ -1.0011 \\ -1.0008 \end{bmatrix} \tag{58}$$

The reduced form is shown in Eqn. (59) for forward flight phase.

$$\begin{bmatrix} \dot{p} \\ \dot{q} \\ \dot{r} \\ \dot{\phi} \\ \dot{\theta} \end{bmatrix} = \left[A_{sys-forward}\right] \begin{bmatrix} p \\ q \\ r \\ \phi \\ \theta \end{bmatrix} + \left[B_{sys-forward}\right] \begin{bmatrix} \delta_{th} \\ \delta_{aileron} \\ \delta_{elevator} \\ \delta_{rudder} \end{bmatrix} \tag{59}$$

The closed loop system is shown in Eqn. (60).

$$\begin{bmatrix} \dot{p} \\ \dot{q} \\ \dot{r} \\ \dot{\phi} \\ \dot{\theta} \end{bmatrix} = \left[A_{sys} - B_{sys}K\right] \begin{bmatrix} p \\ q \\ r \\ \phi \\ \theta \end{bmatrix} + \left[B_{sys}K\right] \begin{bmatrix} 0 \\ 0 \\ 0 \\ \phi_{com} \\ \theta_{com} \end{bmatrix} \tag{60}$$

Similarly, with *K*, the gain matrix obtained from Ricatti equation solution and ϕ_{com} and θ_{com} are the pilot commands. The eigenvalues of the closed loop system in this case are presented in Eqn. (61).

$$eig\left(A_{closed\ loop}\right) = \begin{bmatrix} -46.8933 \\ -17.1730 \\ -9.9978 \\ -0.9990 \\ -0.9527 \end{bmatrix} \tag{61}$$

5.2.4.2. Linear Quadratic Tracking (LQT)

In LQT, the cost function is the weighted sum of the squares of errors and inputs as given in Eqn. (62). [20]

$$J = \frac{1}{2}\int_0^\infty \left(e(t)^T Q e(t) + u(t)^T R u(t)\right) dt \tag{62}$$

where, e is the difference between the commands and the commanded states that is given in Eqn. (63) and Eqn. (64) for hover and forward flight respectively.

$$e_{hover} = \begin{bmatrix} \phi_{com} \\ \theta_{com} \\ \varphi_{com} \end{bmatrix} - \mathrm{C}_{hover} \begin{bmatrix} p \\ q \\ r \\ \phi \\ \theta \\ \varphi \end{bmatrix} \tag{63}$$

$$e_{forward} = \begin{bmatrix} \phi_{com} \\ \theta_{com} \end{bmatrix} - \mathrm{C}_{forward} \begin{bmatrix} p \\ q \\ r \\ \phi \\ \theta \end{bmatrix} \tag{64}$$

$$C_{hover} = \begin{bmatrix} 0 & 0 & 0 & 1 & 0 & 0 \\ 0 & 0 & 0 & 0 & 1 & 0 \\ 0 & 0 & 0 & 0 & 0 & 1 \end{bmatrix} \tag{65}$$

$$C_{forward} = \begin{bmatrix} 0 & 0 & 0 & 1 & 0 \\ 0 & 0 & 0 & 0 & 1 \end{bmatrix} \tag{66}$$

Q and R are the state and control weighting matrices respectively and the same weighting matrices presented above are used.

Fore the trackign problem, a slightly different algebraic Riccati equation is used (Eqn. (54)). The gain matrices are given in Eqn.(68) and Eqn. (69).

$$A_{sys}{}^{T} S + S A_{sys} - S B_{sys} R^{-1} B_{sys}{}^{T} S + C^{T} Q C = 0 \tag{67}$$

$$K = R^{-1} B_{sys}{}^{T} S \tag{68}$$

$$K_z = R^{-1} B_{sys}{}^{T} \left[S B_{sys} R^{-1} B_{sys}{}^{T} - A_{sys}{}^{T} \right]^{-1} C^{T} Q \tag{69}$$

$$u_{hover} = -K\begin{bmatrix} p \\ q \\ r \\ \phi \\ \theta \\ \varphi \end{bmatrix} + K_z \begin{bmatrix} \phi_{com} \\ \theta_{com} \\ \varphi_{com} \end{bmatrix} \tag{70}$$

$$u_{forward} = -K\begin{bmatrix} p \\ q \\ r \\ \phi \\ \theta \end{bmatrix} + K_z \begin{bmatrix} \phi_{com} \\ \theta_{com} \end{bmatrix} \tag{71}$$

The gain matrices for hover and forward flight are shown in Appendix D.

The reduced form is shown in Eqn. (72) for hover phase.

$$\begin{bmatrix} \dot{p} \\ \dot{q} \\ \dot{r} \\ \dot{\phi} \\ \dot{\theta} \\ \dot{\varphi} \end{bmatrix} = [A_{sys}] \begin{bmatrix} p \\ q \\ r \\ \phi \\ \theta \\ \varphi \end{bmatrix} + [B_{sys}] \begin{bmatrix} \delta_{th1} \\ \delta_{th2} \\ \delta_{th3} \\ \delta_{aft} \end{bmatrix} \tag{72}$$

The closed loop system is shown in Eqn. (73).

$$\begin{bmatrix} \dot{p} \\ \dot{q} \\ \dot{r} \\ \dot{\phi} \\ \dot{\theta} \\ \dot{\varphi} \end{bmatrix} = [A_{sys} - B_{sys}K] \begin{bmatrix} p \\ q \\ r \\ \phi \\ \theta \\ \varphi \end{bmatrix} + [B_{sys}K_z] \begin{bmatrix} \phi_{com} \\ \theta_{com} \\ \varphi_{com} \end{bmatrix} \tag{73}$$

K is the gain matrix obtained for state feedback and K_z is the gain matrix for the pilot commands. The eigenvalues of the closed loop system matrix is shown in Eqn. (58).

$$\mathrm{e}ig\left(A_{closed\ loop}\right) = \begin{bmatrix} -3.5553 + 3.5553i \\ -3.5553 - 3.5553i \\ -3.2749 + 3.2749i \\ -3.2749 - 3.2749i \\ -2.2049 + 2.2049i \\ -2.2049 - 2.2049i \end{bmatrix} \tag{74}$$

The reduced form is shown in Eqn. (75) for forward flight phase.

$$\begin{bmatrix} \dot{p} \\ \dot{q} \\ \dot{r} \\ \dot{\phi} \\ \dot{\theta} \end{bmatrix} = \left[A_{sys-forward}\right] \begin{bmatrix} p \\ q \\ r \\ \phi \\ \theta \end{bmatrix} + \left[B_{sys-forward}\right] \begin{bmatrix} \delta_{th} \\ \delta_{aileron} \\ \delta_{elevator} \\ \delta_{rudder} \end{bmatrix} \tag{75}$$

In this case, the eigenvalues of the closed loop system matrix are presented in Eqn. (76).

$$eig\left(A_{closed\ loop}\right) = \begin{bmatrix} -4.9730 + 4.6943i \\ -4.9730 - 4.6943i \\ -10.0095 \\ -3.9009 + 1.0655i \\ -3.9009 - 1.0655i \end{bmatrix} \tag{76}$$

CHAPTER 6

SIMULATION RESULTS

The designed linear controllers, LQR and LQT are examined throughout the nonlinear simulation code explained previously. This chapter describes the configuration parameters of the simulation, the response of the controllers to pilot commands.

6.1 Configuration Parameters

The simulation step size is taken as 20 ms. The ordinary differential equations are solved using 4th order Runge Kutta method.
The simulation is run at the trim flight conditions and it was verified that the system stays at the trim conditions with the controller.
In order to observe the performance of the controllers, pilot commands that pass through the controller before actuating the air vehicle are given separately and the response of the air vehicle is examined both for hover and forward flight phases.

The simulation results are obtained for LQR and LQT controllers separately. In addition the effect of a washout filter is investigated with LQR controller that is shown in Figure 36. In the first case a washout filter for the body rates of the aircraft is not used; however in the second case a washout filter is used for the body rates in order to avoid the struggle between the between the autopilot and the pilot commands. The time constant used in the washout filter is chosen to be 4 after a trial-

and-error process. In selecting the time constant the settling time of the response is the governor.

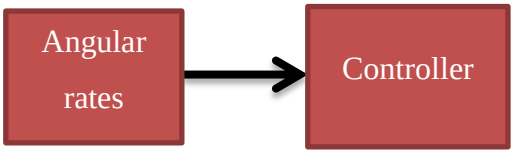

Case 1 – No filter

Case 2 – Washout filter

Figure 36 Hover simulation cases for LQR

The transfer function of the washout filter is given in Eqn. (77)

$$TF = \frac{s}{s + 0.25} \tag{77}$$

6.2 Hover Simulation Results

6.2.1 Roll Command

The roll command is given as 30 deg roll angle as a pulse input between 1-9 seconds and the response of the aircraft is shown in Figure 37-Figure 39 for LQR without and with the washout filter and for LQT respectively. Comparing Figure 37 and Figure 38 it may be observed that the LQR controller with washout filters has almost half the rise time than the one without the washout filters. However, it overshoots as well as undershoots. On the other hand the response with LQT controller has the lowest rise time and follows the commands quite more closely (Figure 39). The controller

inputs are also given in Figure 40-Figure 48. These results show that the throttle requirements are reasonable and may easily be realized by the engines. Similar observation may be made about the aft throttle tilt angle.

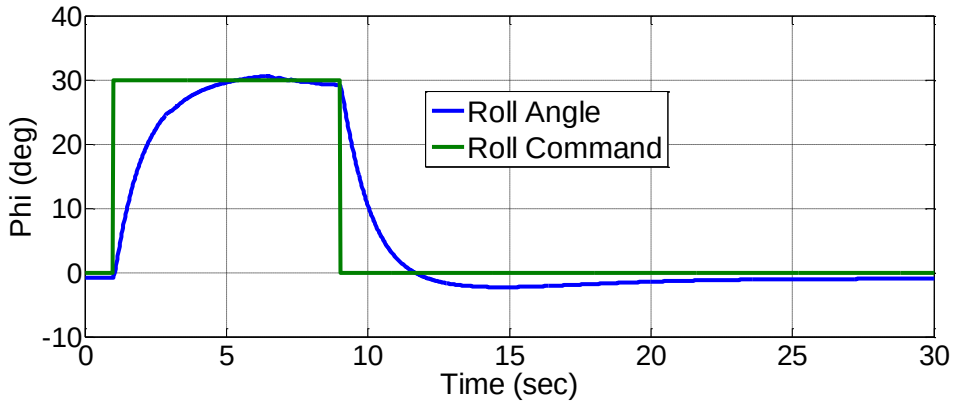

Figure 37 Roll angle and roll command time histories without washout filter (LQR)

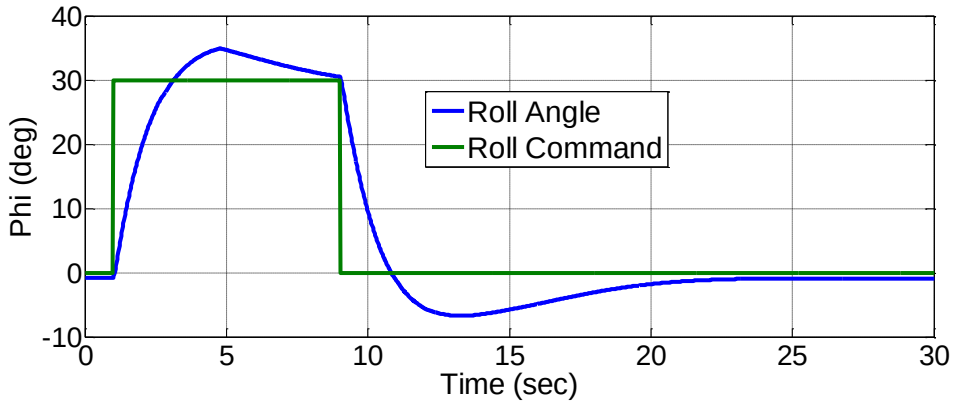

Figure 38 Roll angle and roll command time histories with washout filter (LQR)

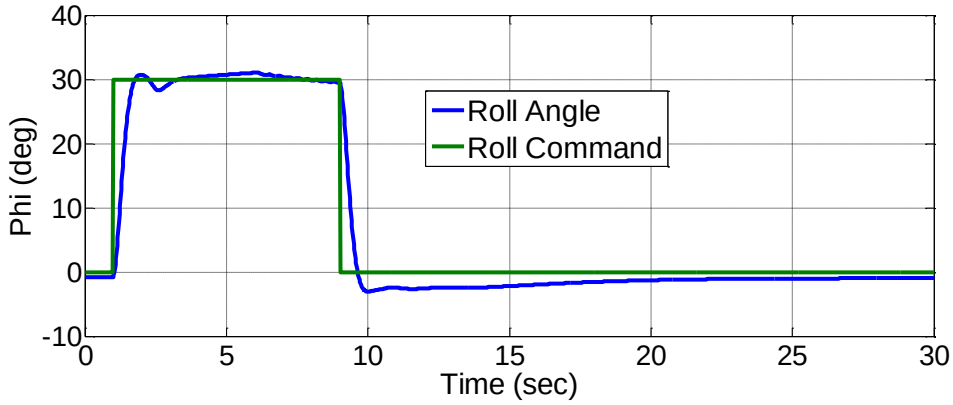

Figure 39 Roll angle and roll command time histories (LQT)

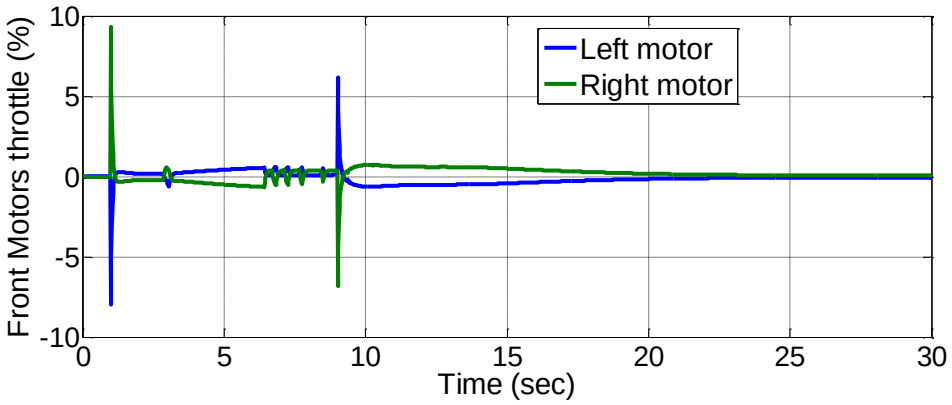

Figure 40 Front motors throttle percentage time histories without washout filter (LQR)

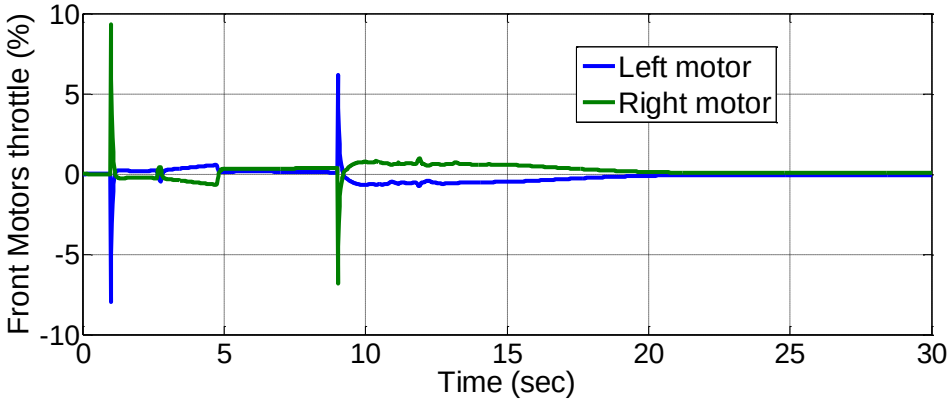

Figure 41 Front motors throttle percentage time histories with washout filter (LQR)

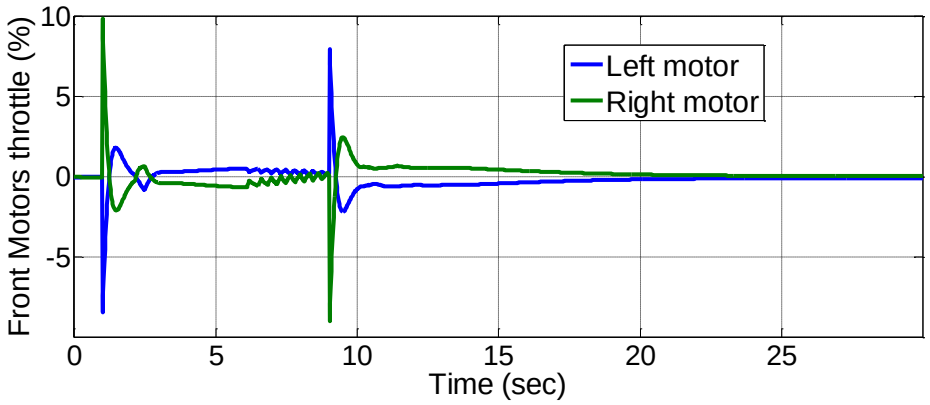

Figure 42 Front motors throttle percentage time histories (LQT)

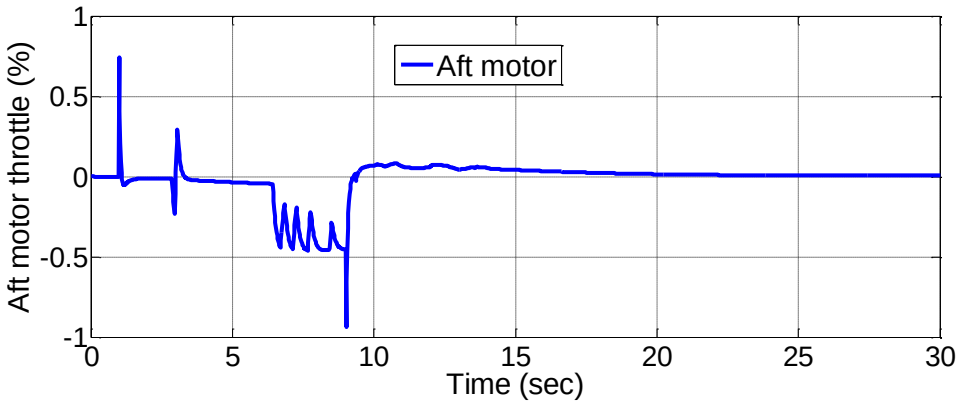

Figure 43 Aft motor throttle percentage time histories without washout filter (LQR)

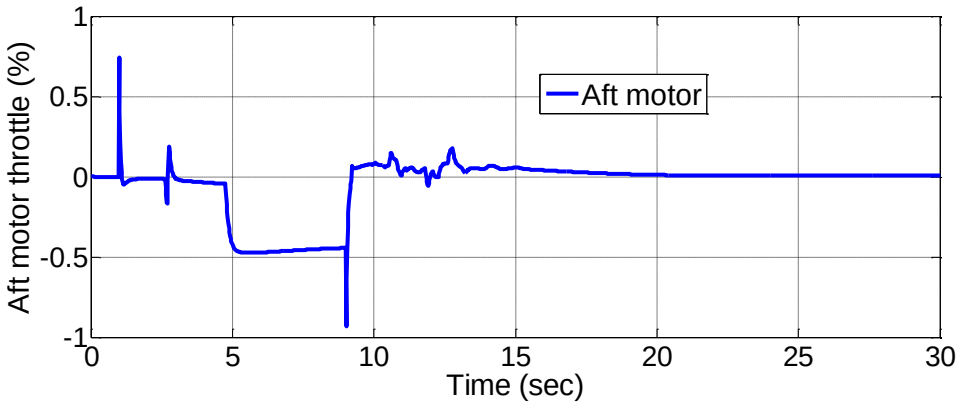

Figure 44 Aft motor throttle percentage time histories with washout filter (LQR)

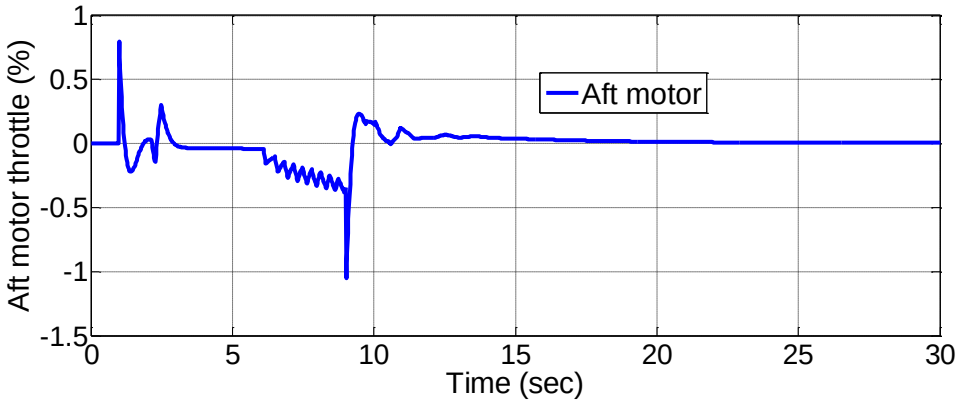

Figure 45 Aft motor throttle percentage time histories (LQT)

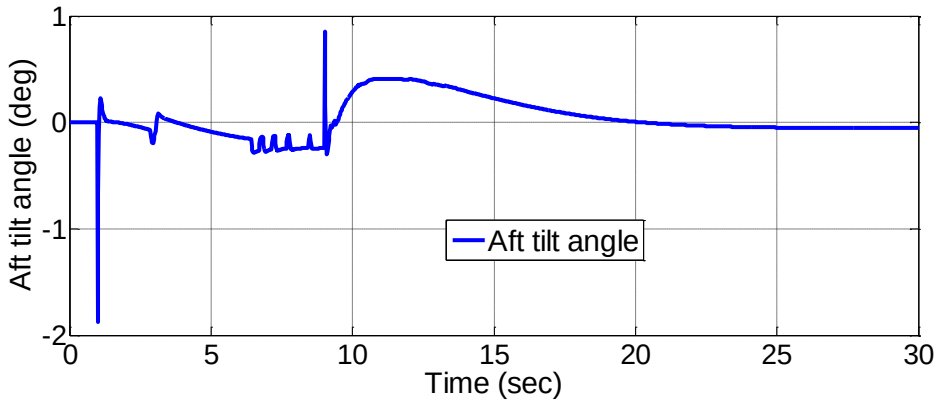

Figure 46 Aft motor tilt angle time histories without washout filter (LQR)

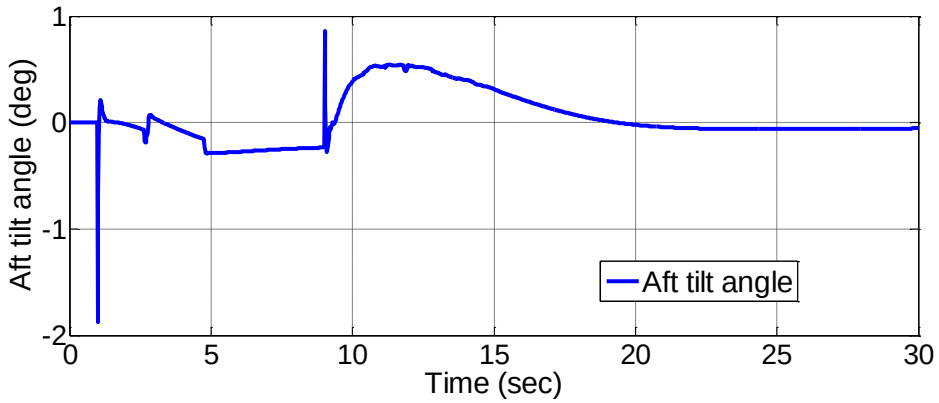

Figure 47 Aft motor tilt angle time histories with washout filter (LQR)

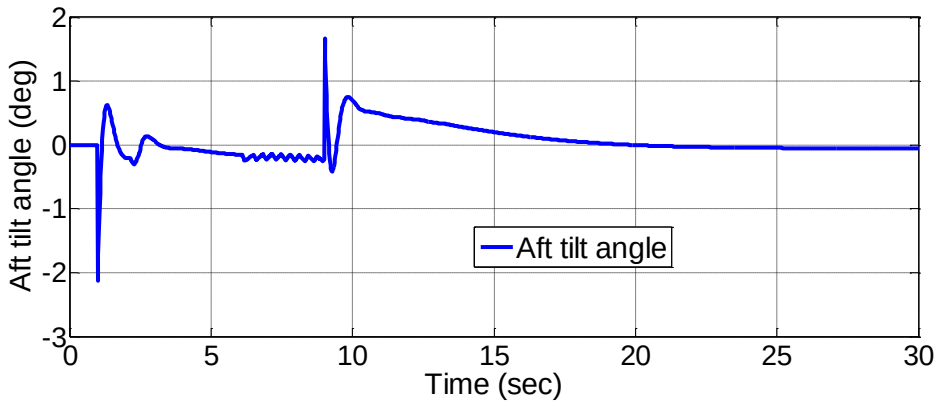

Figure 48 Aft motor tilt angle time histories (LQT)

6.2.2 Pitch Command

A 30 deg pitch angle as a pulse input between 1-9 seconds and the response of the aircraft is shown in Figure 49-Figure 51 for LQR without and with the washout filter and for LQT respectively. Similar responses as the roll command are obtained. Thus, the LQR controller without washout responds much slower compared with the LQR controller with washout. There are again overshoots and undershoots in the response of the LQR with washout. The LQT controller has again the lowest rise time and follows the input closely. The controller inputs are also given in Figure 52-Figure 57. Examination of these inputs indicates that these commands are reasonable and may easily be realized by the engines.

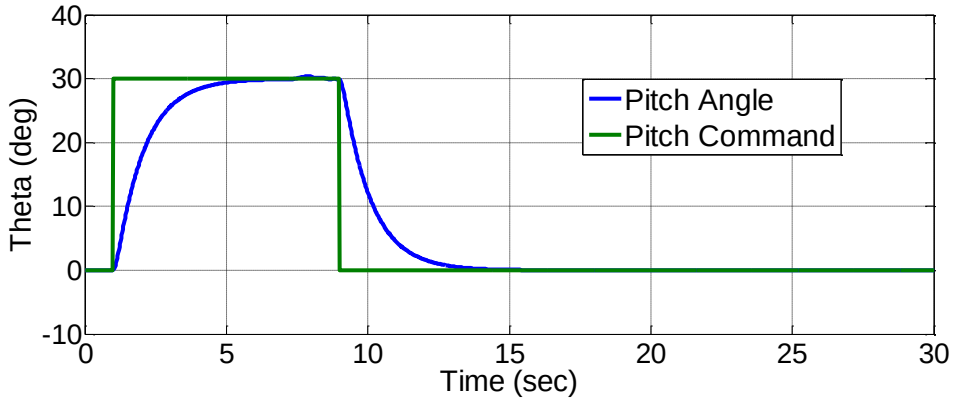

Figure 49 Pitch angle and pitch command time histories without washout filter (LQR)

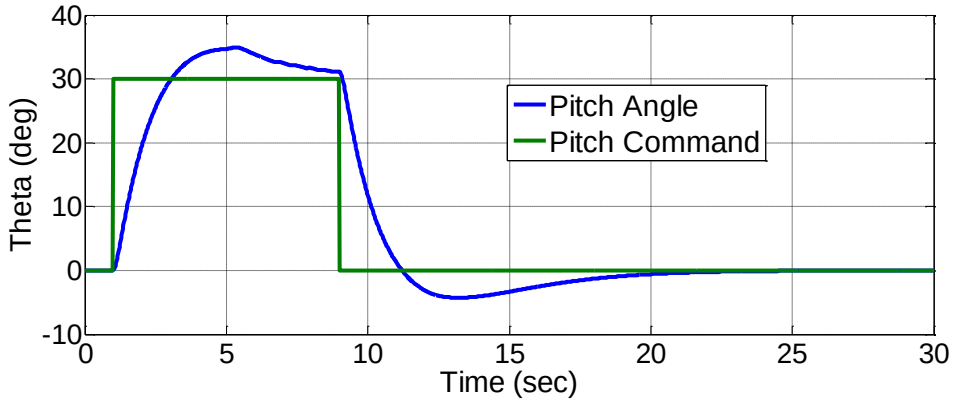

Figure 50 Pitch angle and pitch command time histories with washout filter (LQR)

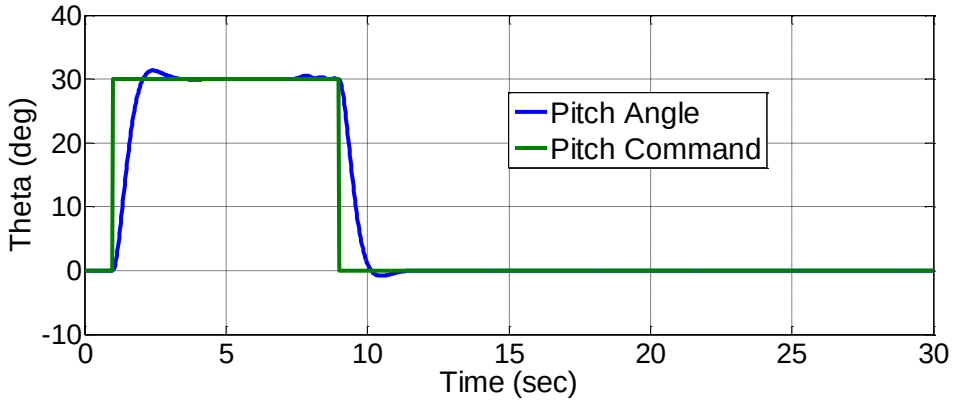

Figure 51 Pitch angle and pitch command time histories (LQT)

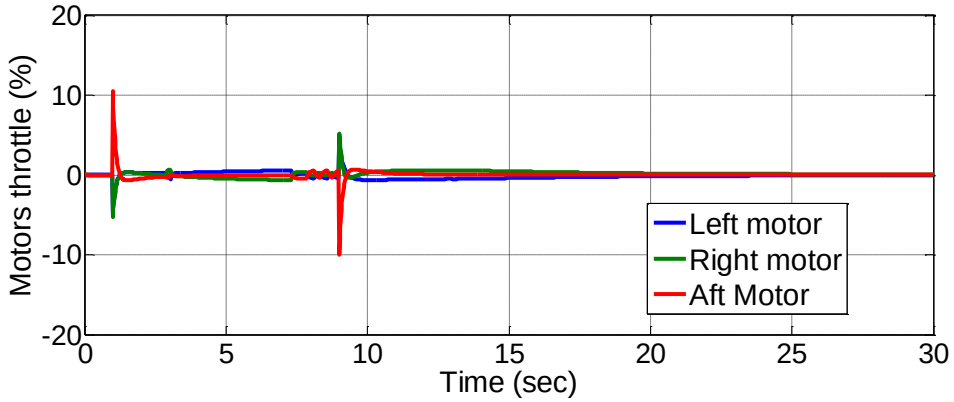

Figure 52 Motors throttle percentage time histories without washout filter (LQR)

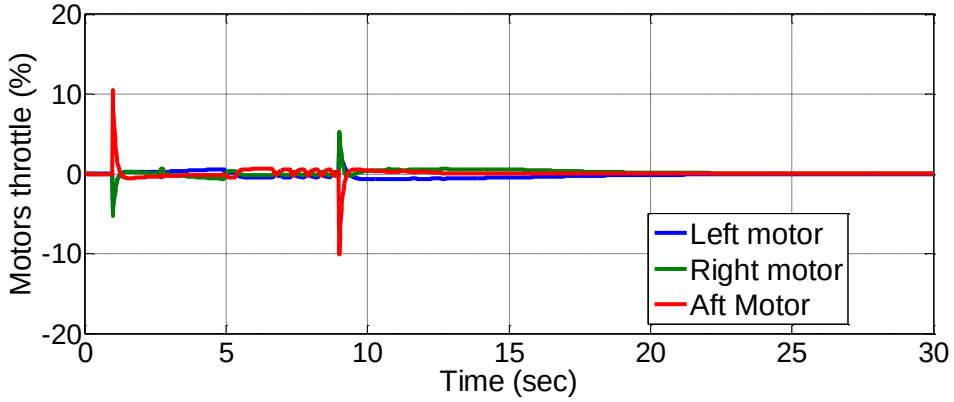

Figure 53 Motors throttle percentage time histories with washout filter (LQR)

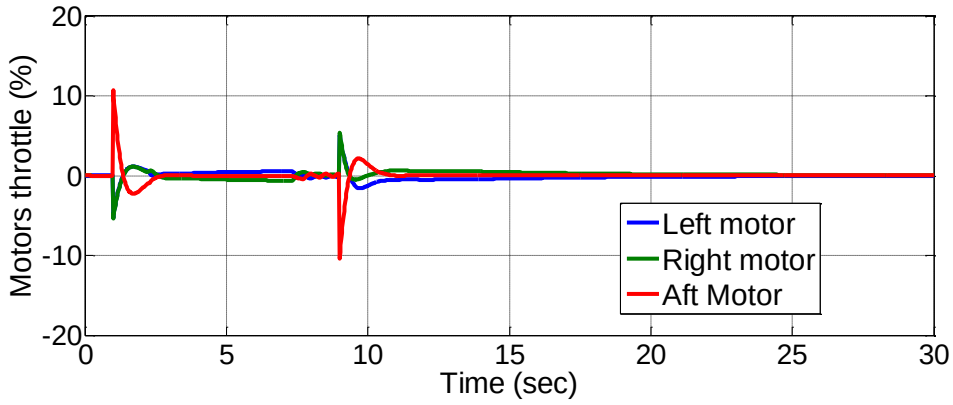

Figure 54 Motors throttle percentage time histories (LQT)

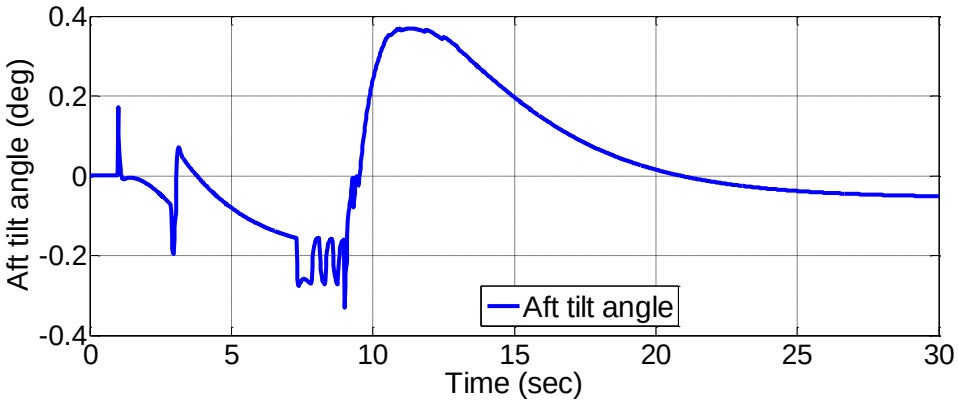

Figure 55 Aft motor tilt angle time histories without washout filter (LQR)

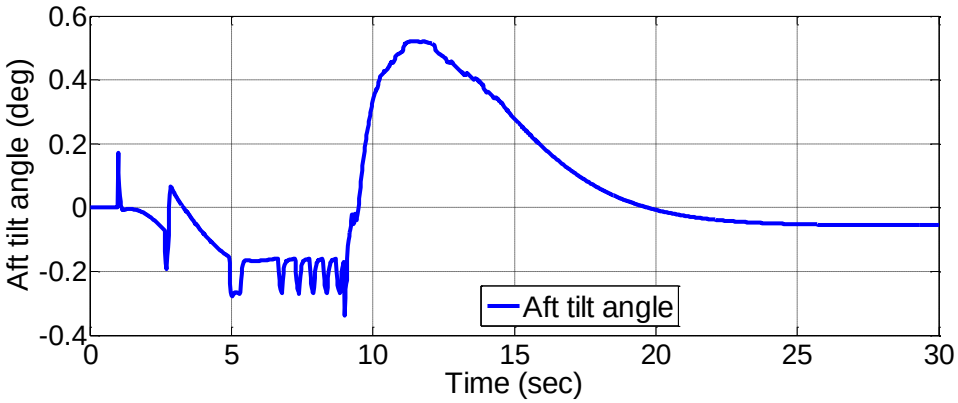

Figure 56 Aft motor tilt angle time histories with washout filter (LQR)

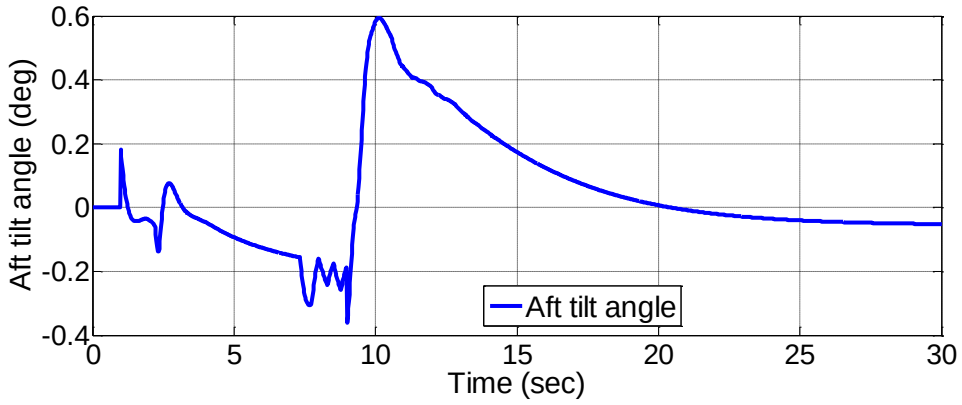

Figure 57 Aft motor tilt angle time histories (LQT)

6.2.3 Yaw Command

A 30 deg yaw angle command in the form of a pulse is applied for eight seconds, and the response of the aircraft is shown in Figure 58-Figure 60 for LQR without and with the washout filter and for LQT respectively. The results are similar to the previous simulation results given for the roll and pitch responses. Thus, the LQT controller has the lowest rise time, follows the commands closely. LQR with washout has overshoots and undershoots. The LQR alone has the longest rise time. The controller inputs are also given in Figure 61-Figure 66. Realizable commands are observable from these figures as before.

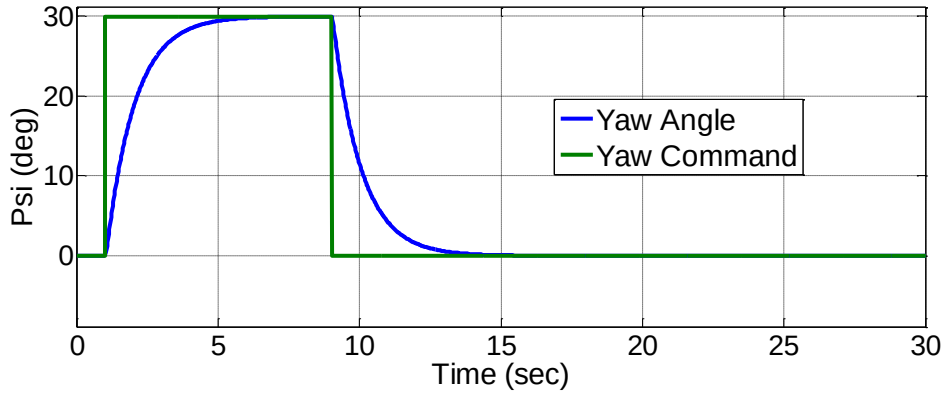

Figure 58 Yaw angle and yaw command time histories without washout filter (LQR)

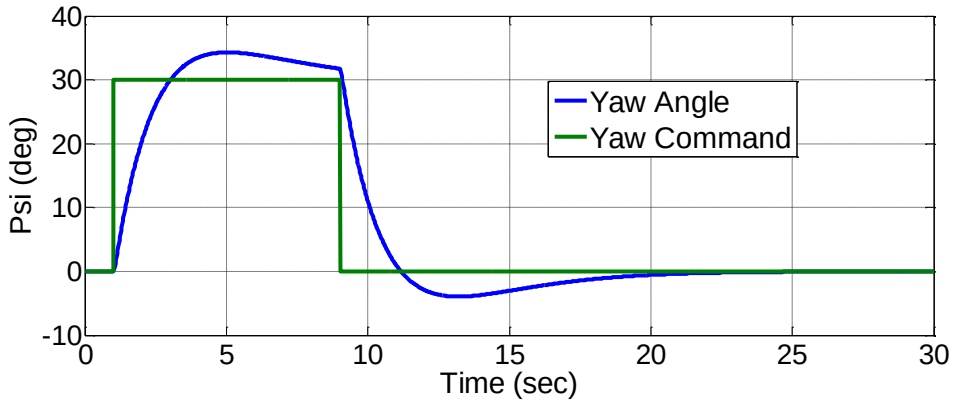

Figure 59 Yaw angle and yaw command time histories with washout filter (LQR)

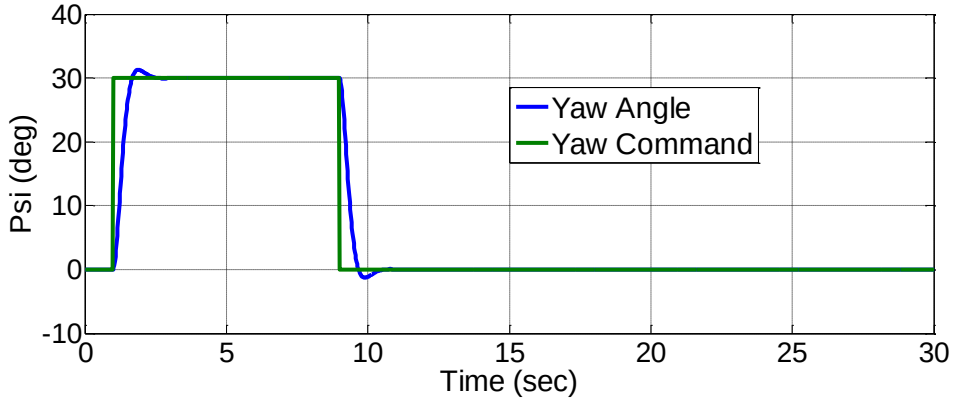

Figure 60 Yaw angle and yaw command time histories (LQT)

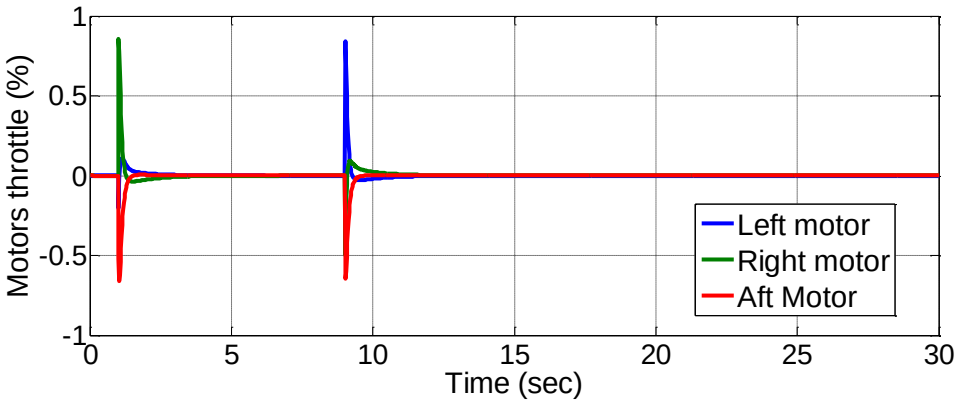

Figure 61 Motors throttle percentage time histories without washout filter (LQR)

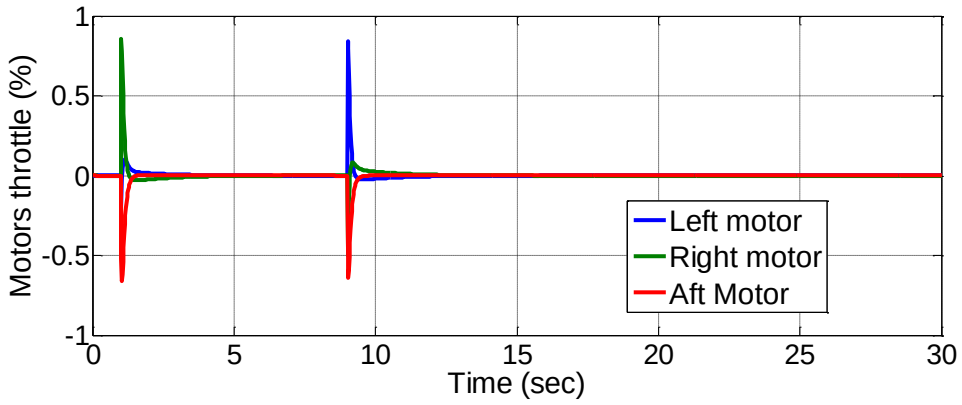

Figure 62 Motors throttle percentage time histories with washout filter (LQR)

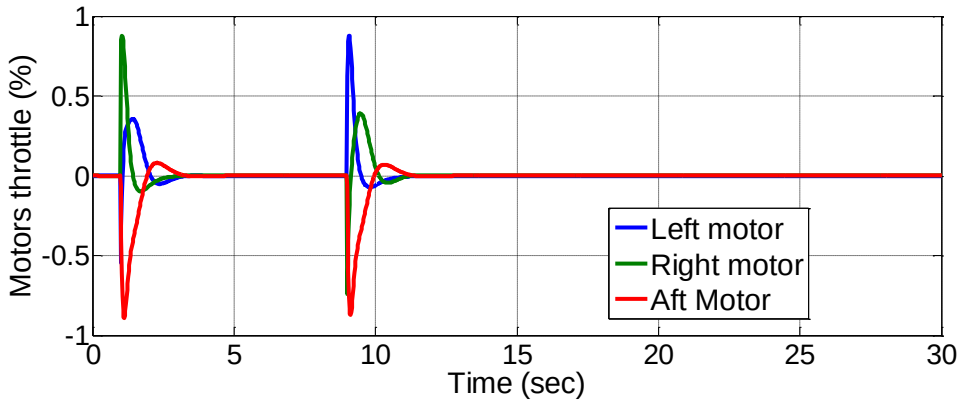

Figure 63 Motors throttle percentage time histories (LQT)

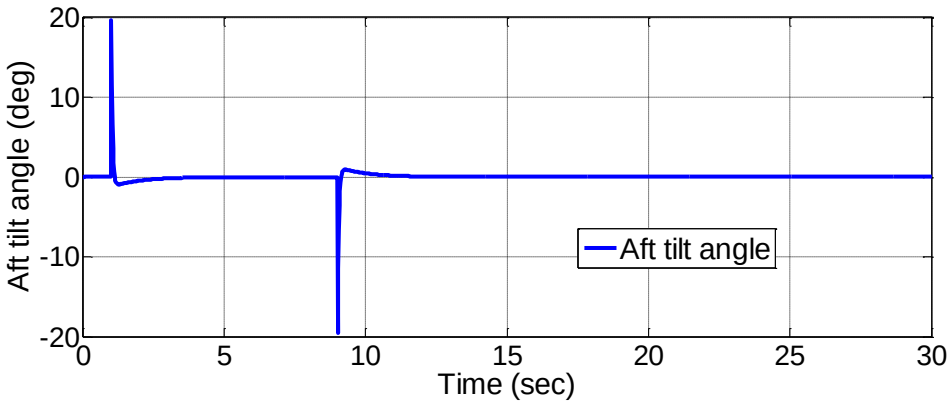

Figure 64 Aft motor tilt angle time histories without washout filter (LQR)

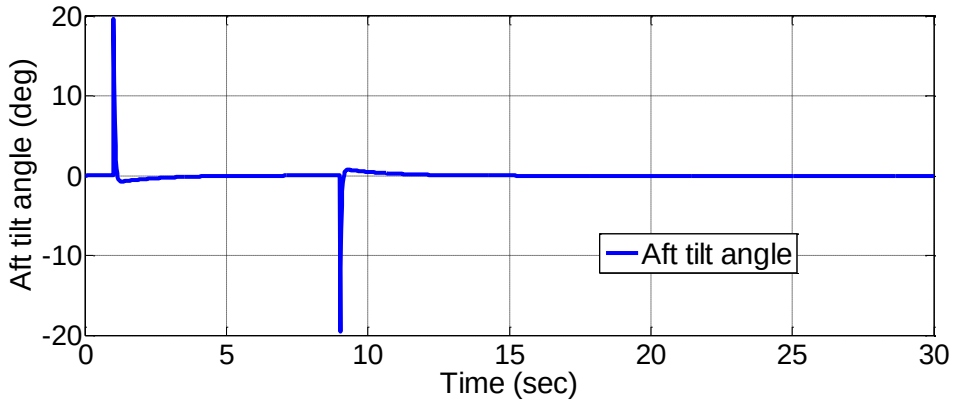

Figure 65 Aft motor tilt angle time histories with washout filter (LQR)

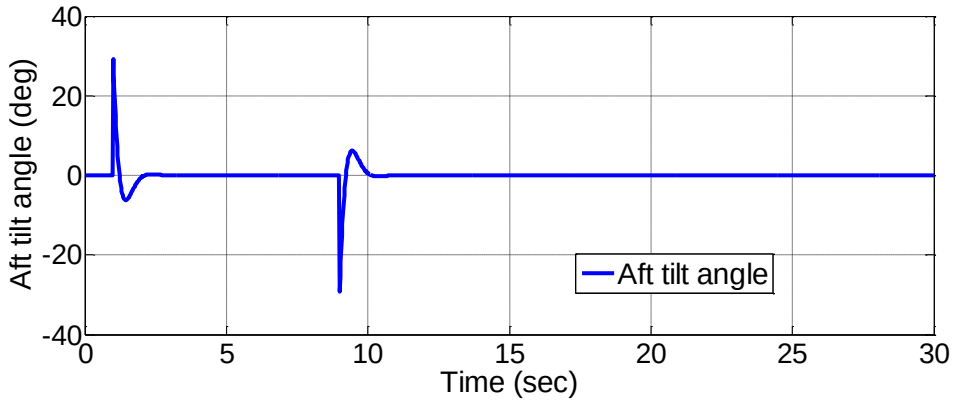

Figure 66 Aft motor tilt angle time histories (LQT)

In rolling motion a differential thrust between the right and left electric motors is observable. In pitching motion also differential thrust control between front and aft electric motors are commanded. In yawing motion on the other hand is mainly realized by tilting the aft engine. The washout filter effects the system in such a way that the rise time is reduced, and the response first overshoots and then goes to zero with an undershoot when compared with the no filter response. The overshoot is tolerable. The filter proposed in the s-domain transferred to the z-domain, using Tustin approximation and hover tests are performed with the installed hardware. The test results are presented in Chapter 7.

6.3 Forward Flight Simulation Results

6.3.1 Roll Command

Similar roll, pitch and yaw simulation results are presented in this section. Note that for the forward flight phase, the classical aileron, rudder and elevator control surfaces are used. The thrust is generated with the two front engines with forward looking propellers. The roll command is given as 30 deg roll angle as a pulse input of two seconds duration. The responses of the aircraft are shown in Figure 67-Figure 68 for LQR and LQT respectively. The controller inputs are also given in Figure 69-Figure 76. In each of these cases, similar observations as those presented in hover flight may be made. In all cases, LQR controller without washout filter falls short from the commanded angle in the specified command duration, while the simulation with the linear tracking control on the other hand tracks the input faster. In all cases, the required control surface deflections are realizable. Unlike hover the heading angle is not controlled in forward flight.

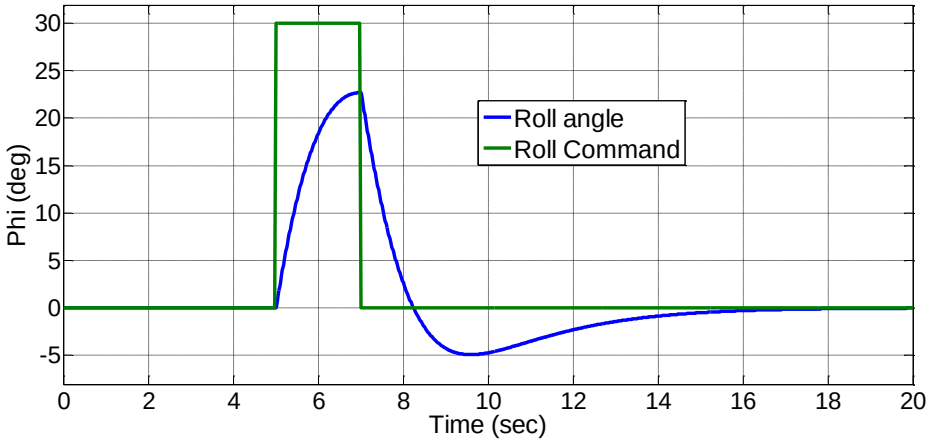

Figure 67 Roll angle and roll command time histories (LQR)

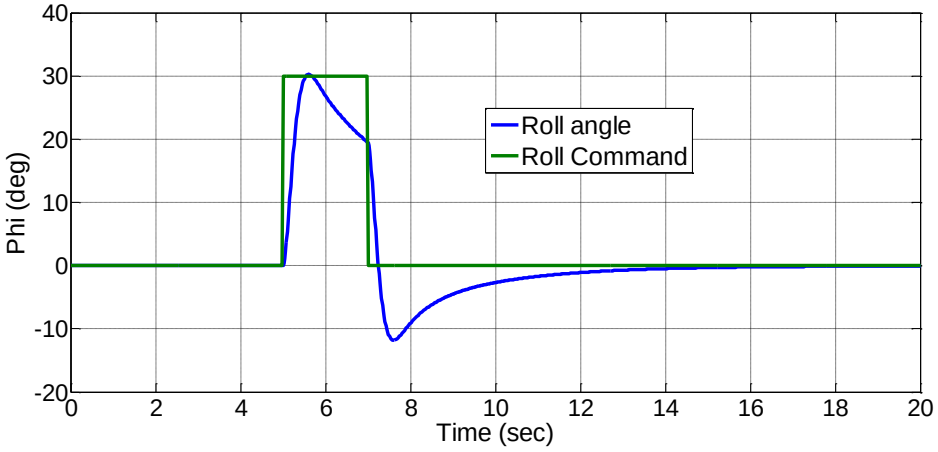

Figure 68 Roll angle and roll command time histories (LQT)

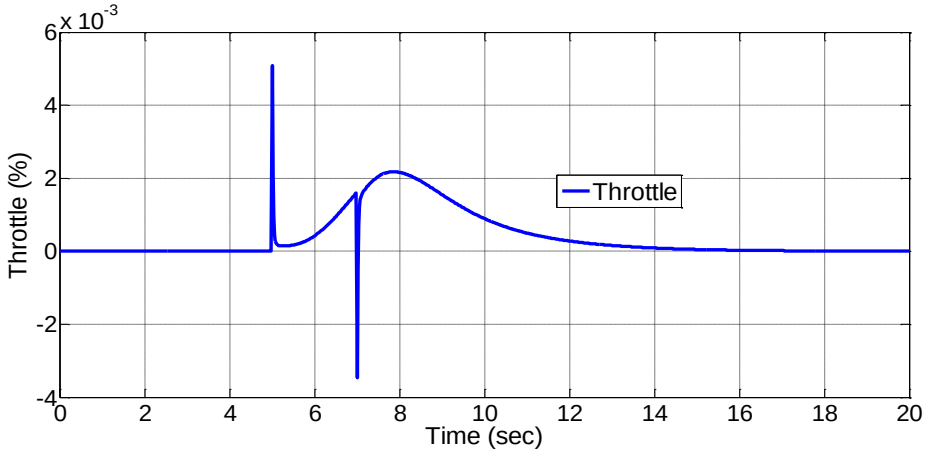

Figure 69 Throttle percentage time histories (LQR)

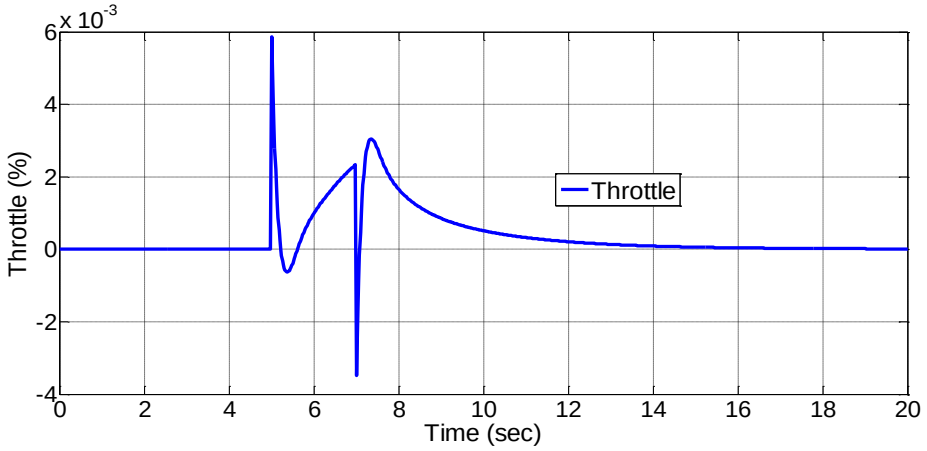

Figure 70 Throttle percentage time histories (LQT)

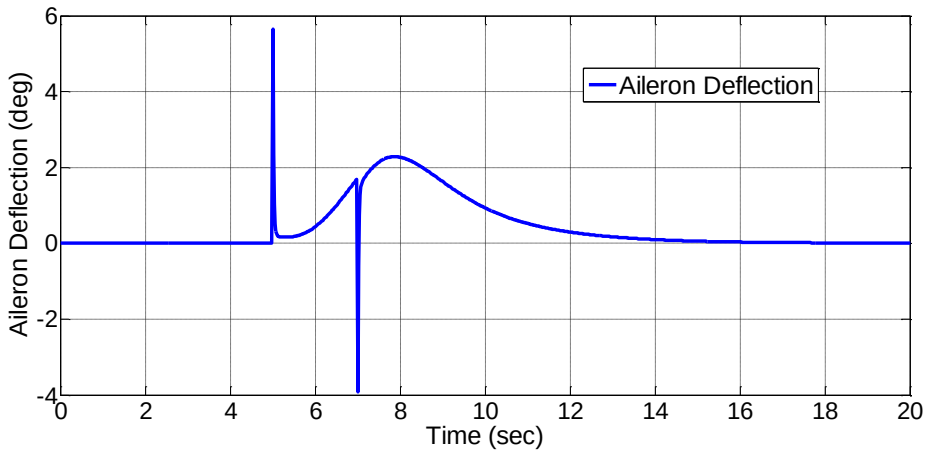

Figure 71 Aileron deflection time histories (LQR)

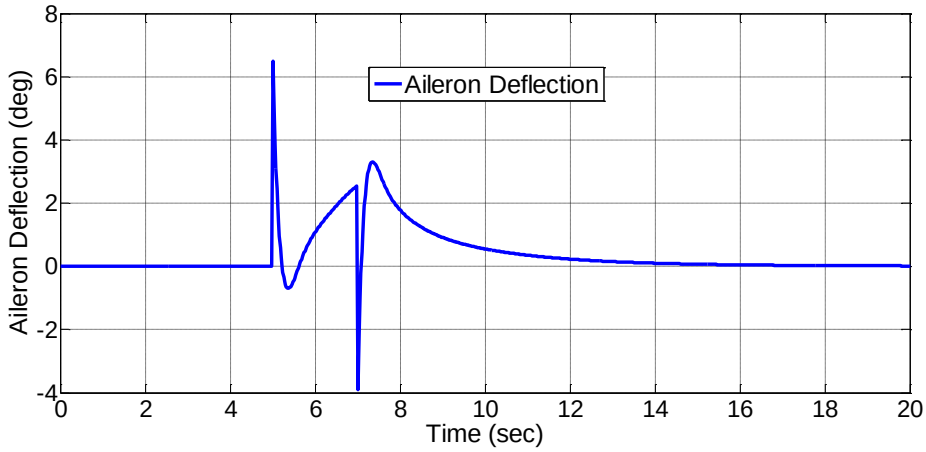

Figure 72 Aileron deflection time histories (LQT)

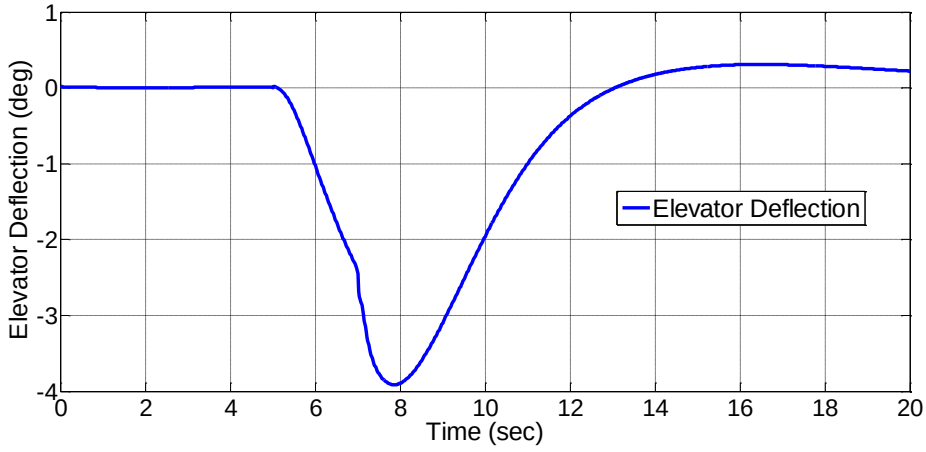

Figure 73 Elevator deflection time histories (LQR)

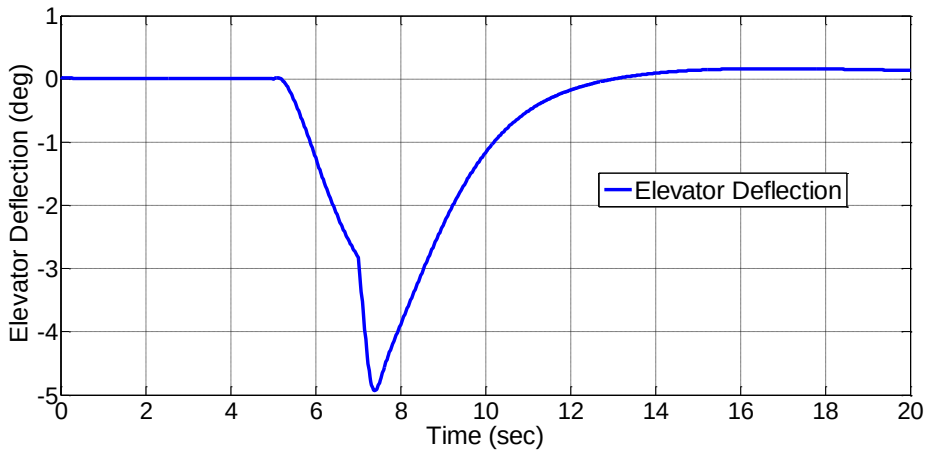

Figure 74 Elevator deflection time histories (LQT)

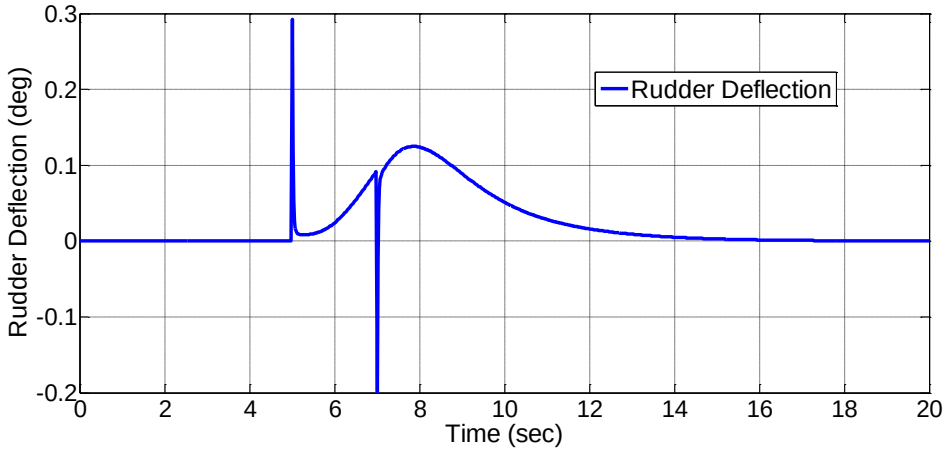

Figure 75 Rudder deflection time histories (LQR)

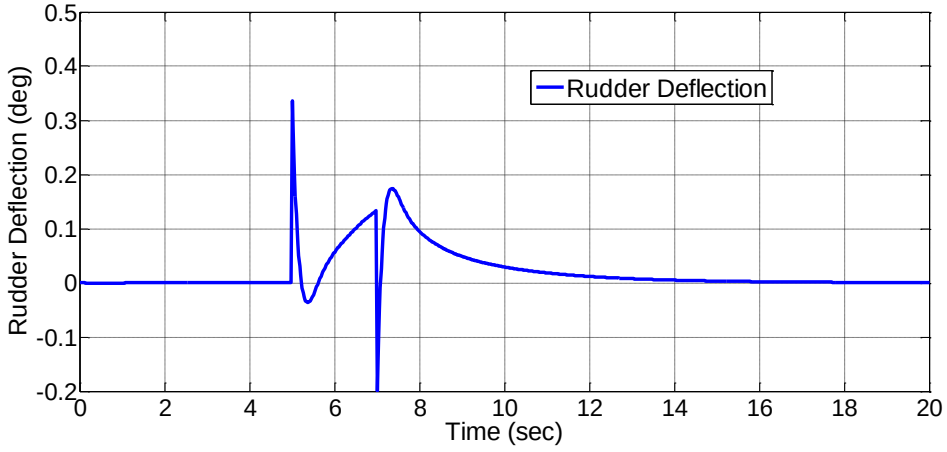

Figure 76 Rudder deflection time histories (LQT)

6.3.2 Pitch Command

The pitch command is given as 30 deg roll angle as a pulse input between 5-7 seconds and the response of the aircraft is shown in Figure 77-Figure 78 for LQR and LQT respectively. The controller inputs are also given in Figure 79-Figure 86.

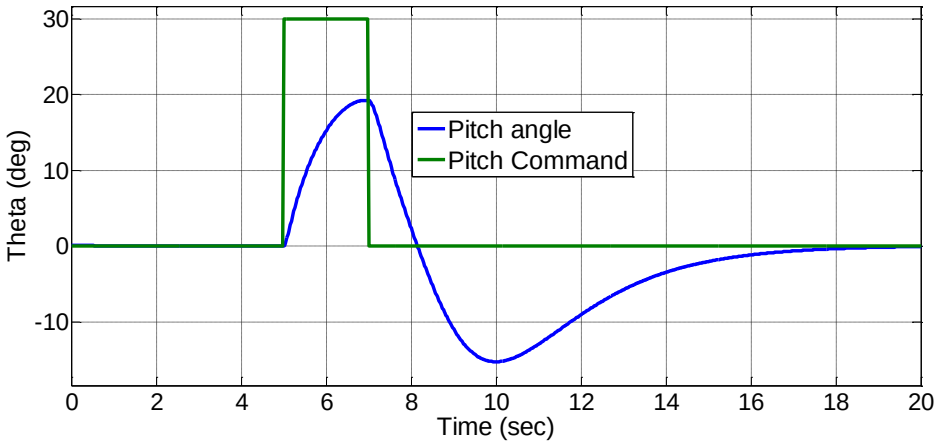

Figure 77 Pitch angle and pitch command time histories (LQR)

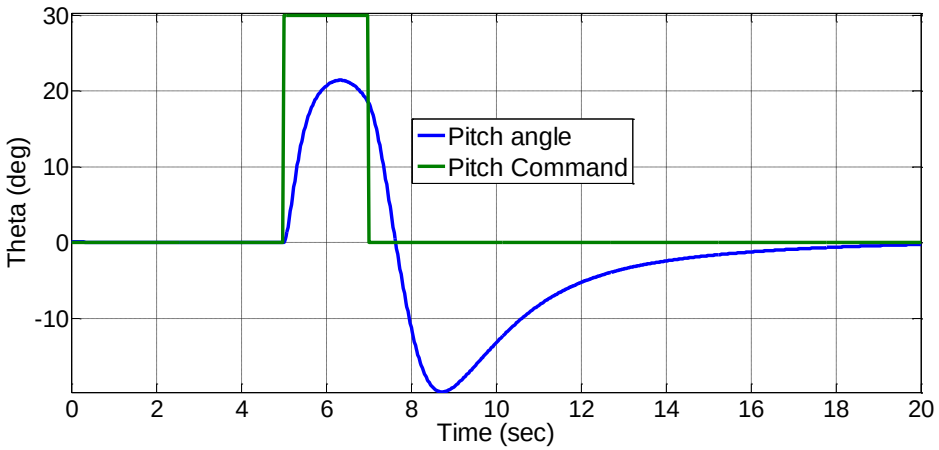

Figure 78 Pitch angle and pitch command time histories (LQT)

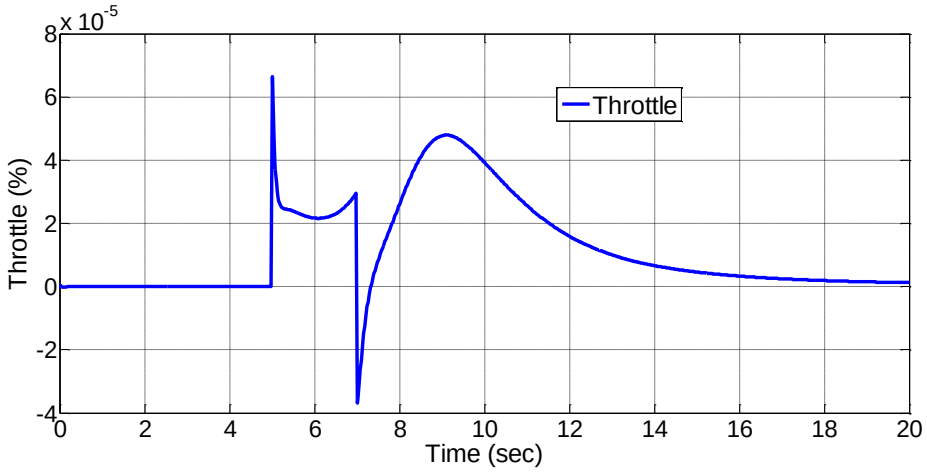

Figure 79 Throttle percentage time histories (LQR)

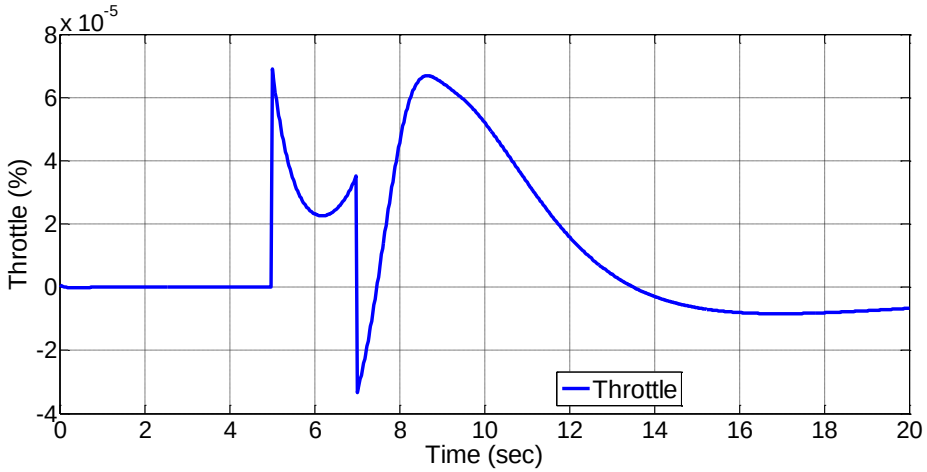

Figure 80 Throttle percentage time histories (LQT)

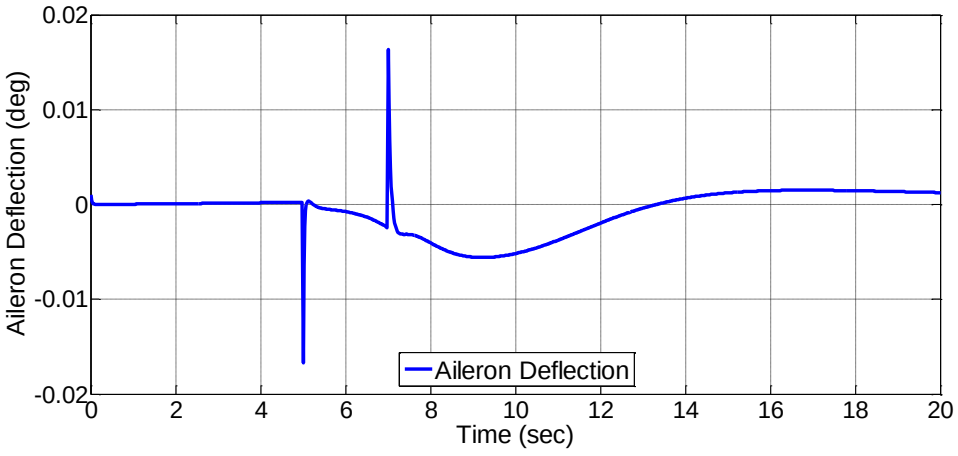

Figure 81 Aileron deflection time histories (LQR)

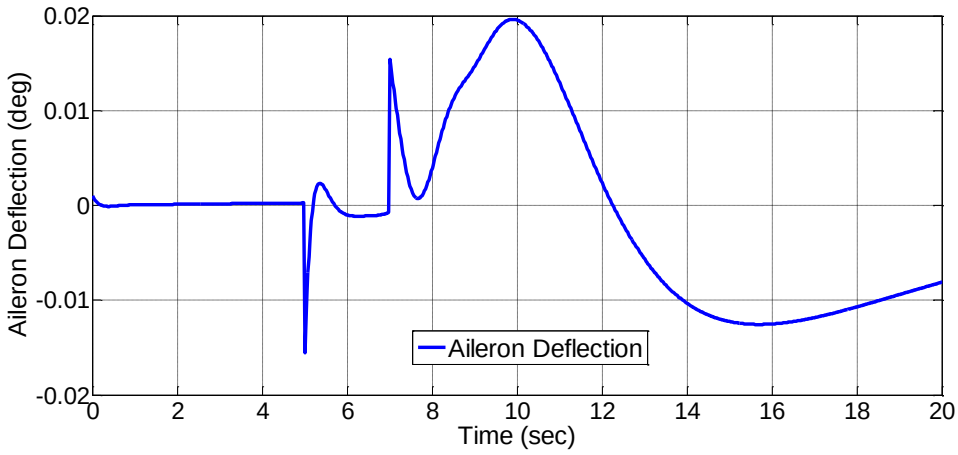

Figure 82 Aileron deflection time histories (LQT)

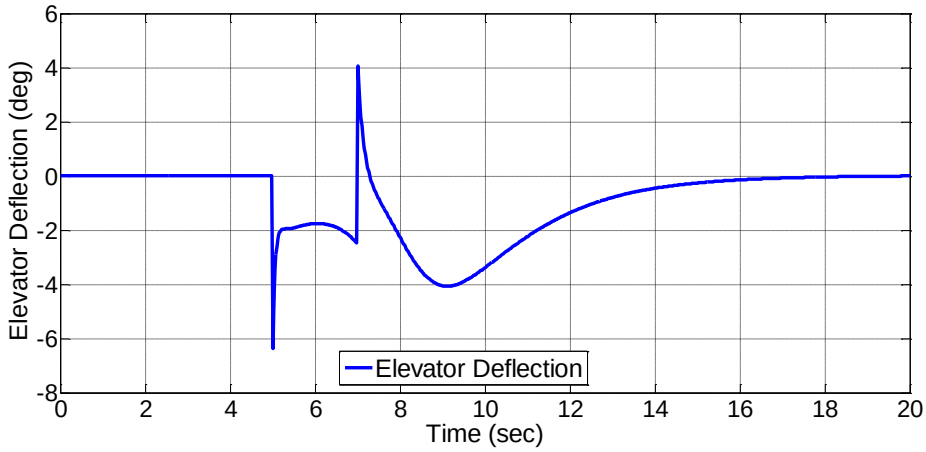

Figure 83 Elevator deflection time histories (LQR)

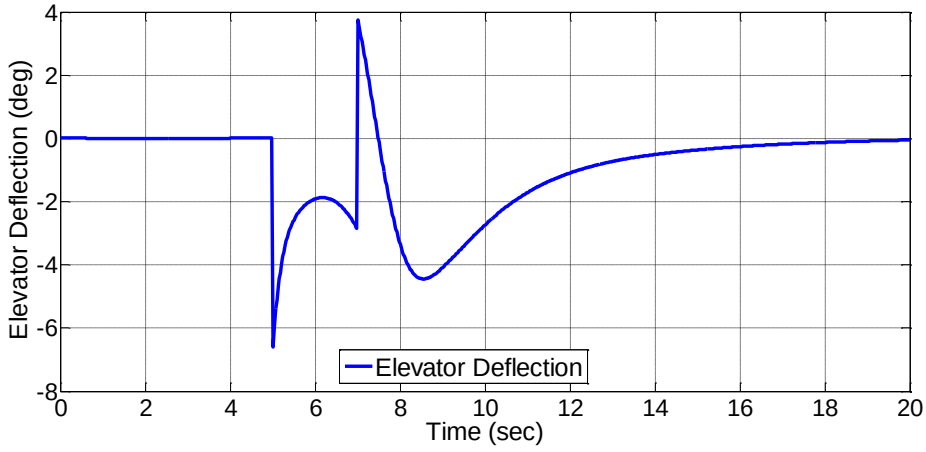

Figure 84 Elevator deflection time histories (LQT)

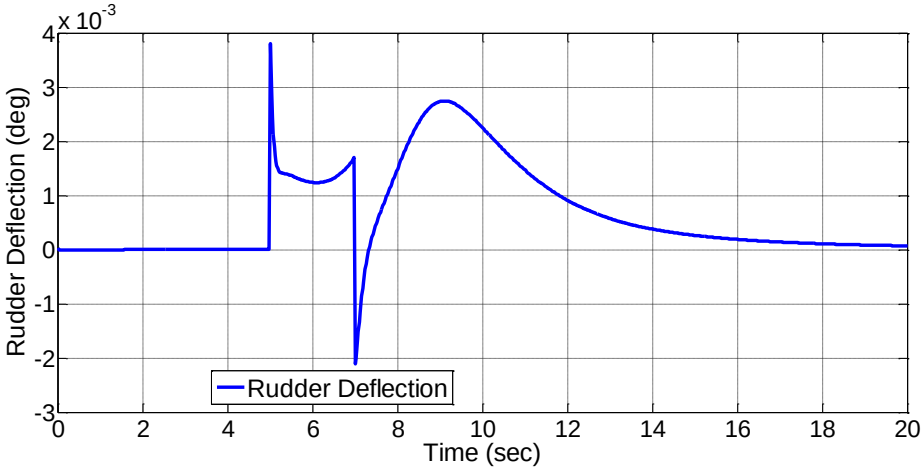

Figure 85 Rudder deflection time histories (LQR)

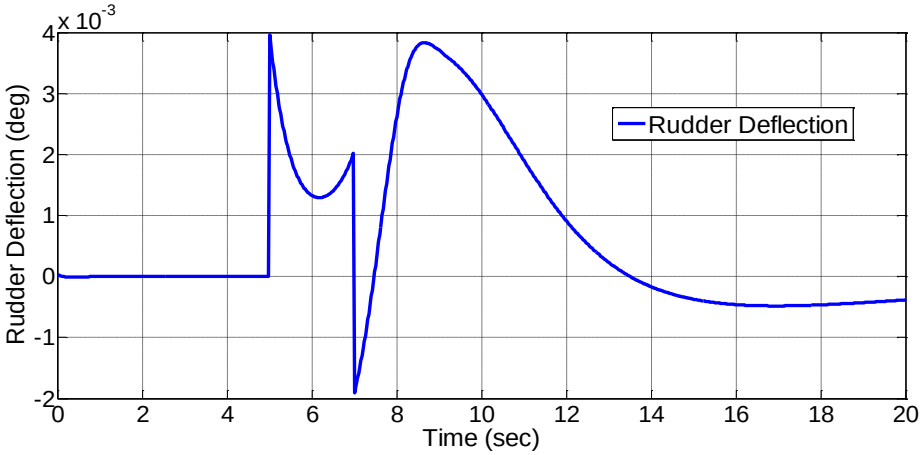

Figure 86 Rudder deflection time histories (LQT)

6.3.3 Yaw Command

The yaw command is given as 10 deg of a 2 second duration that is shown in Figure 87 and the response of the aircraft is shown in Figure 88-Figure 89 for LQR and LQT respectively. The controller inputs are also given in Figure 90-Figure 97. Unlike roll and pitch, yaw angle is not controlled and the heading angle is changing to a certain extent as expected. However, the yaw rate is controlled, that is why the change in the heading angle decreases with time.

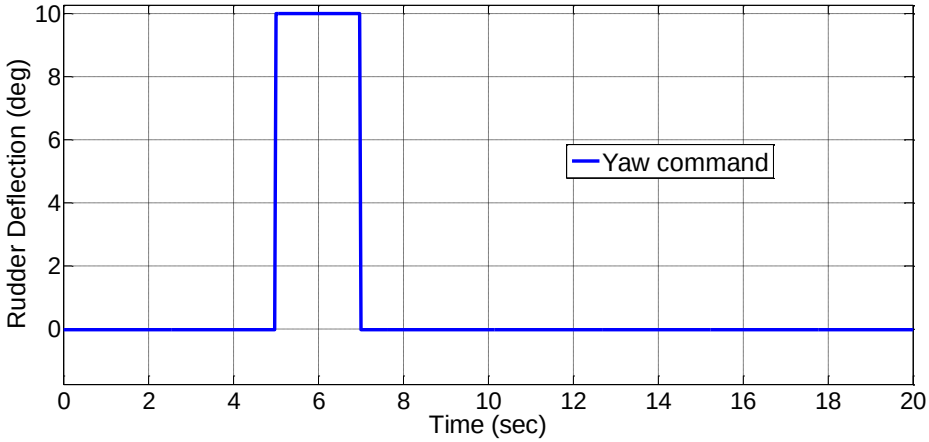

Figure 87 Yaw command input time histories

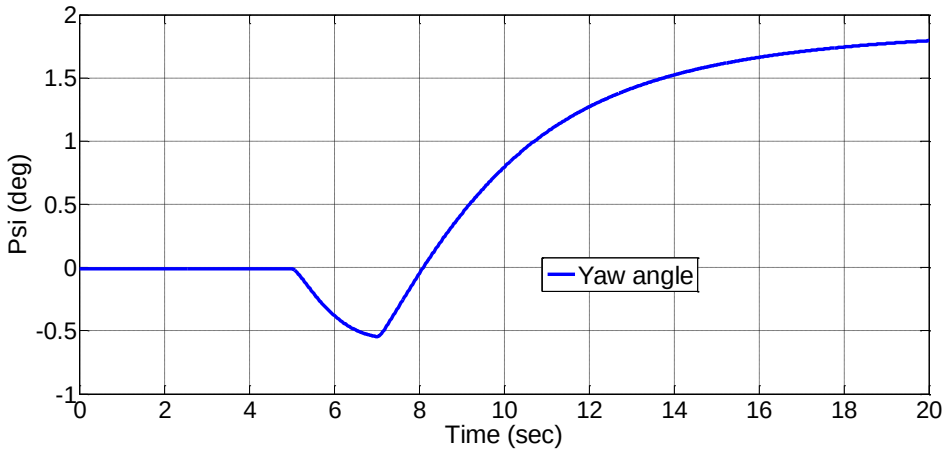

Figure 88 Yaw angle time histories (LQR)

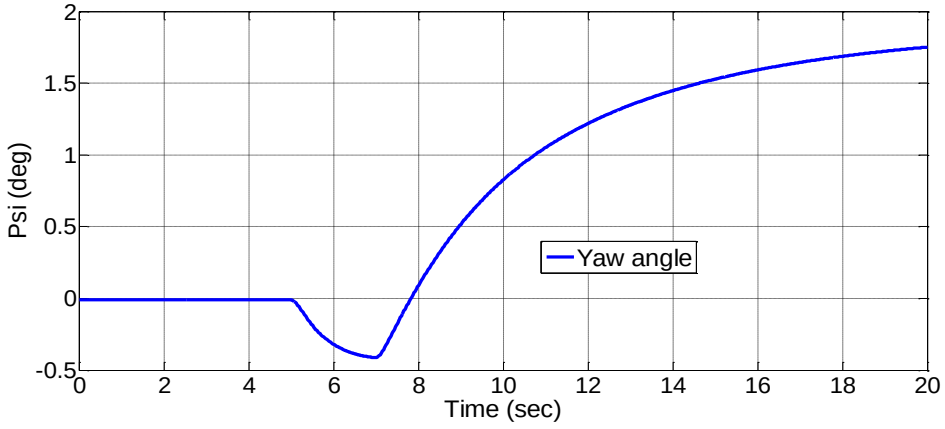

Figure 89 Yaw angle time histories (LQT)

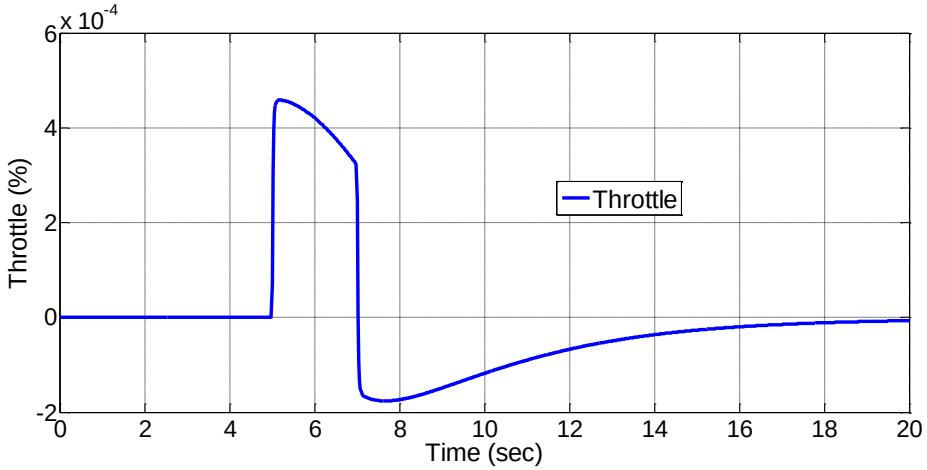

Figure 90 Throttle percentage time histories (LQR)

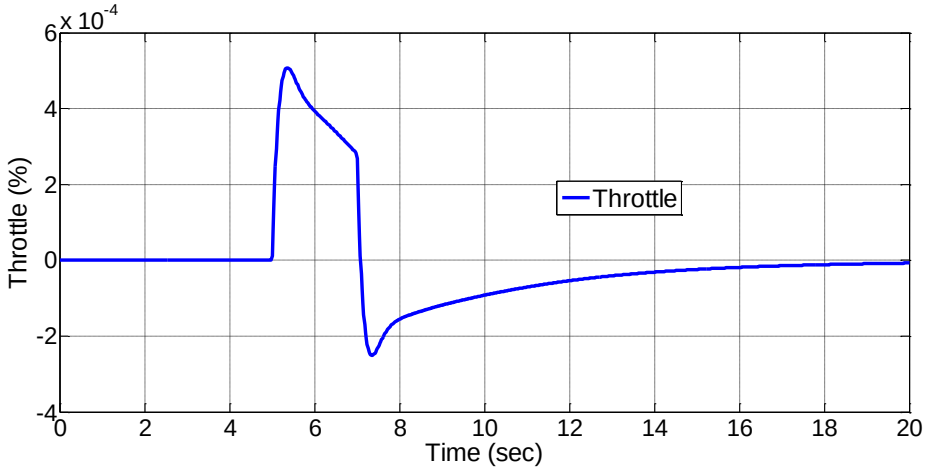

Figure 91 Throttle percentage time histories (LQT)

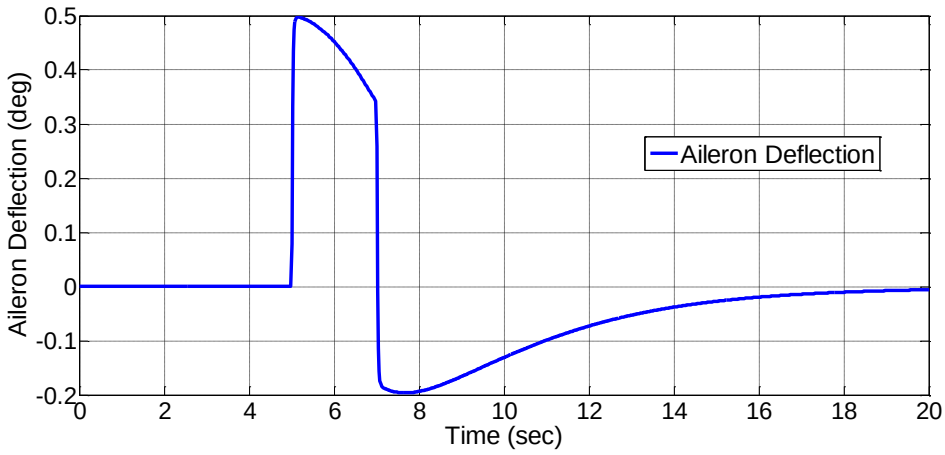

Figure 92 Aileron Deflection time histories (LQR)

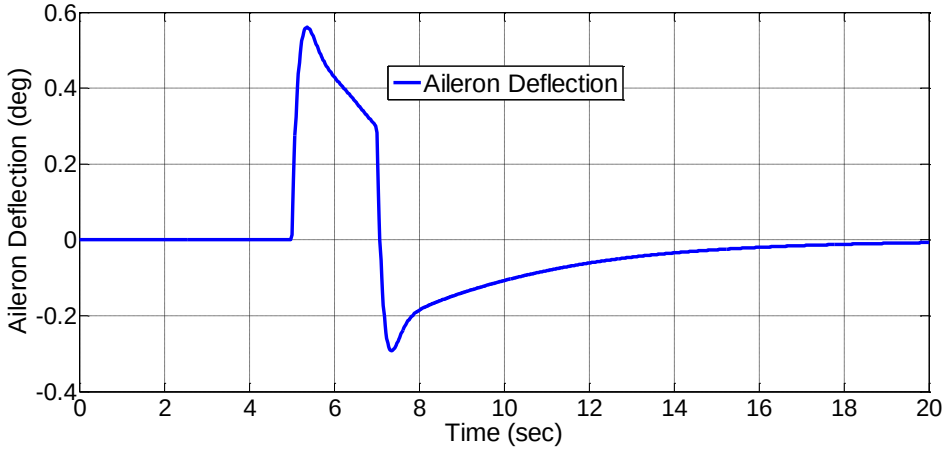

Figure 93 Aileron Deflection time histories (LQT)

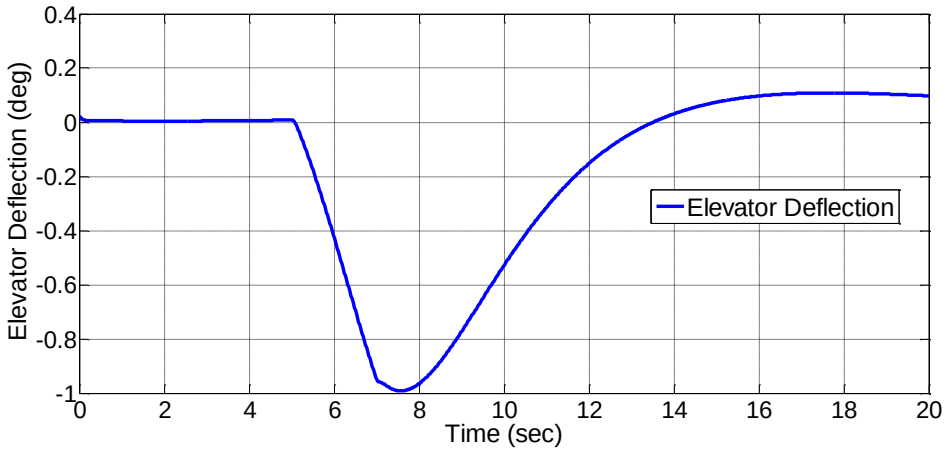

Figure 94 Elevator Deflection time histories (LQR)

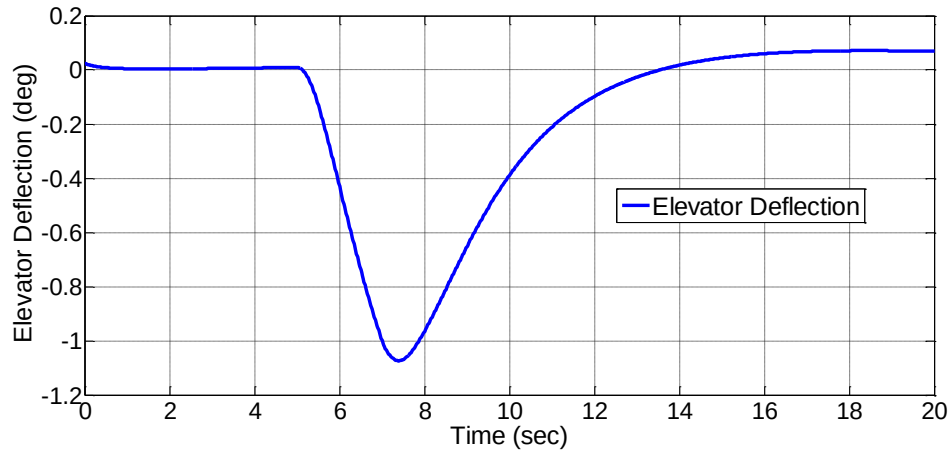

Figure 95 Elevator Deflection time histories (LQT)

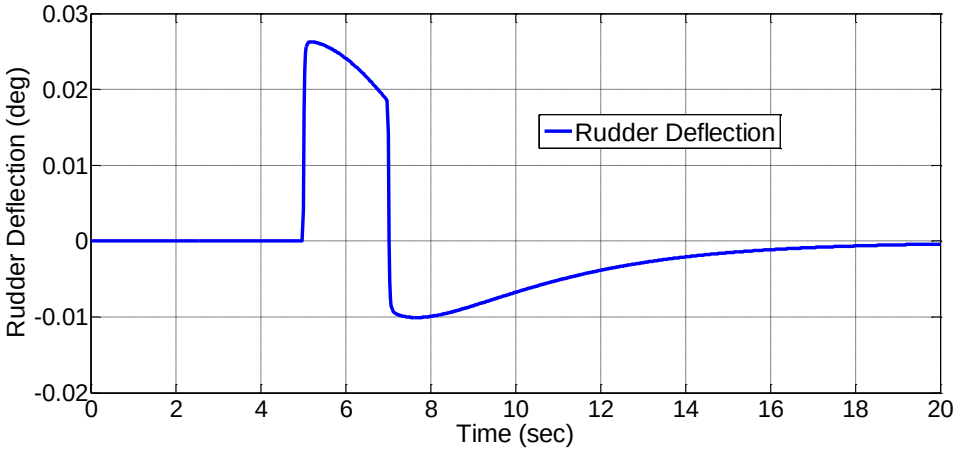

Figure 96 Rudder Deflection time histories (LQR)

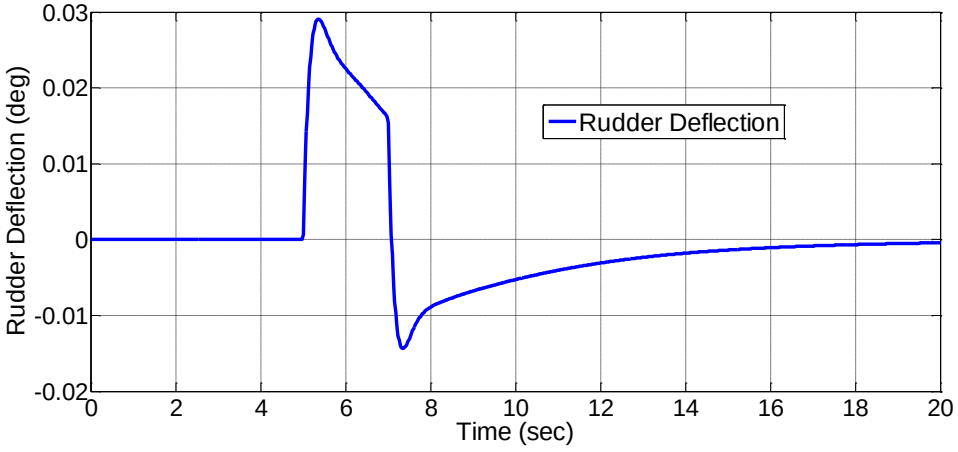

Figure 97 Rudder Deflection time histories (LQT)

The lateral stability of the aircraft is improved by adding the relation between the roll rate and the rolling moment, and the relation between the yaw rate and yawing moment as stated in the aerodynamics model section. In rolling motion the controller adjusts the aileron deflection to stabilize the system. In pitching motion the dominant actuator is the elevator in stabilizing the system. In yawing motion ailerons are working with the rudder.

The throttle input is the least dominant term among all inputs in stabilizing the rotational dynamics as expected. In yawing motion, unlike roll and pitch the pilot gives the actuator input directly. As it can be seen from Figure 87-Figure 88, a pulse input with a magnitude of 10 degree and duration of 2 seconds makes the aircraft yaw for 1.5 degree. The relation between the pilot input and the actuator can be tuned after performing forward flight tests in the future if the response of the aircraft in heading is thought to be unsatisfactory. Unlike the hover case, a washout filter is not used for the angular rates. Instead, only LQT results are compared with LQR results. The main difference between LQR and LQT controller is that, the rise time is reduced in LQT and the commands are very closely tracked by the aircraft in LQT. In rolling motion, the comparison between Figure 67-Figure 68 shows that the command is tracked by the aircraft in a successful way in LQT when compared with LQR. In pitching motion, when Figure 77-Figure 78 are compared, the aircraft again has a better command tracking performance in LQT; however, the aircraft is stiffer in pitching dynamics compared with the rolling dynamics. The tracking of the command can be improved by reducing the pitch stiffness of the aircraft or by tuning the gains. In yawing motion, as the heading of the aircraft is not controlled, the controller inputs are more or less the same for LQR and LQT.

CHAPTER 7

FLIGHT TESTING

The best way to verify the controller that is designed in Chapter 5 is performing real flight tests. The controller may also be fine-tuned as a result of these tests. Hence, testing the hardware is a milestone in design.

In this study the flight testing of the attitude control algorithms are carried out. The aircraft is first tested in the laboratory while hanging from the bar attached to the ceiling. Then the actual flight tests are performed.

7.1 The Test Equipment

The test equipment shown in Figure 98 is composed of a sliding bar attached to the ceiling of the test room at one end to the center of gravity of the air vehicle at the other end. Mechanism is simply working as a pendulum when the weight of the aircraft is not balanced by the thrust. The air vehicle can move and rotate freely with the test setup within the mechanical limits of the mechanism which lets one investigate the rolling, pitching and yawing motion of the air vehicle.

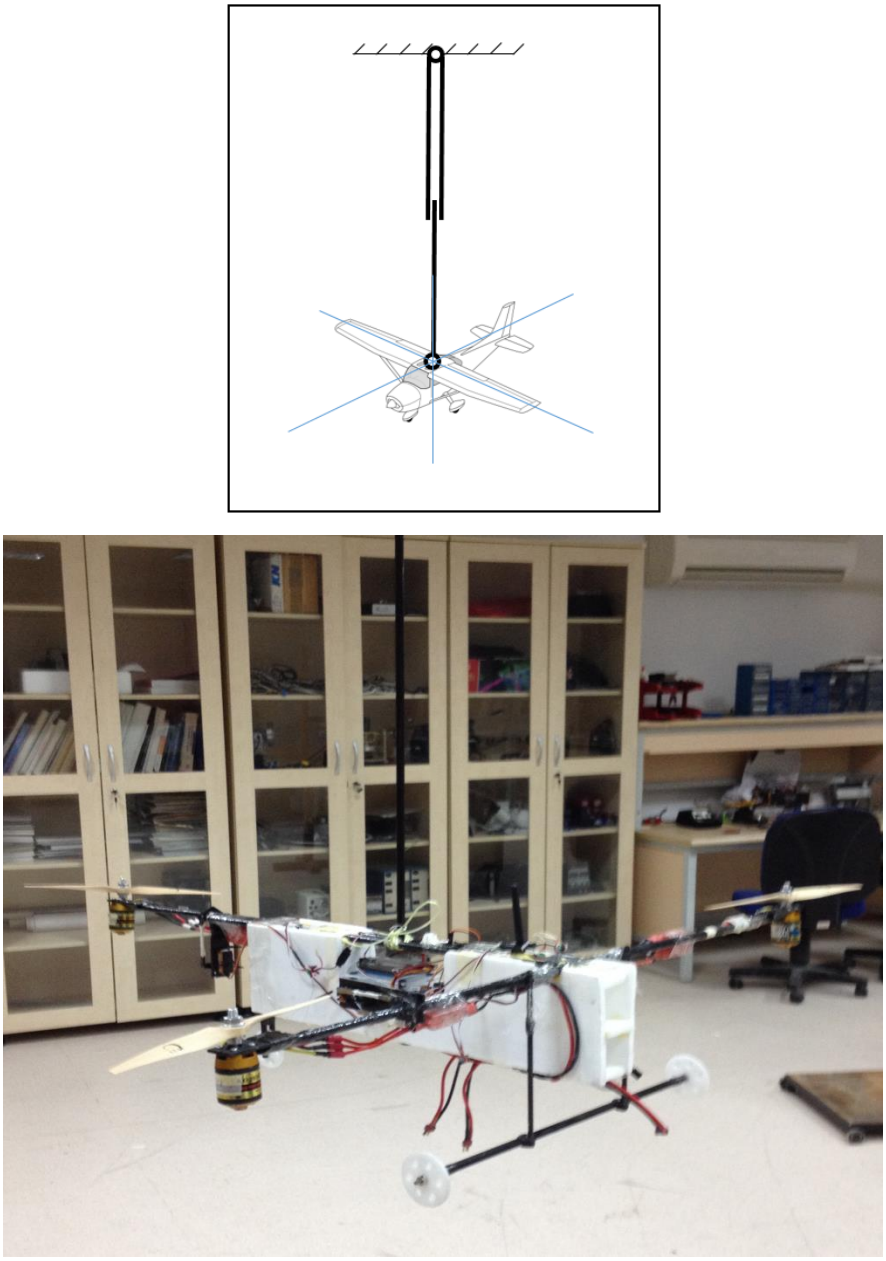

Figure 98 Test equipment

The data is gathered through a PC based ground station. The ground control station consists of a ground control computer, an RC transmitter and telemetry system. Ground control computer is an ultra-book which can run ArduPilot user-interface Mission Planner. Real time flight data was monitored on the ground computer by the 3 DR 433 MHz telemetry link. Flight data recording starts when the telemetry link between APM 2.6 and ground control computer establishes. Telemetry transmitter on APM 2.6 communicates with autopilot via UART interface and the receiver connects

to the computer via Micro-USB port. Both telemetries are configurable and have 117 dBm receive sensitivity. Due to the noise, possible obstacles and distance in the range data loss is avoided by error correction that can correct up to 25% of bit errors. The ground station is shown in Figure 99.

Figure 99 Ground Station

7.2 Avionics

The platform that has been used to implement the control algorithm is ArduPilot mega 2.6 microcontroller. It is chosen since it has open source software updated continuously and the source code may be edited by the user. The hardware of the system includes ArduPilot with three-axis gyro, accelerometer, magnetic compass and telemetry.

System provides gyro data and RC inputs that are used under control algorithm. The control outputs are given to each ESC (Electronic speed controller) and aft-servo that is used to stabilize the air vehicle in hover, as pulse-width modulated signals. In this way, the required speeds for each propeller and angle of the aft motor can be realized.

ArduPilot Mega is using ATmega 2560 microcontroller that uses 256kB flash memory program with operating speed of 16 MHz. An onboard 4 Mb data-flash chip is used for data-logging. It operates between 4.5-5.5 volts range. It can communicate

with sensors, telemetry, and it can drive servo motors through PWM, 4 USARTs, byte oriented 2-wire serial interface, 16-channel 10-bit A/D converter. [21] The system is sufficiently fast enough in handling on board sensor reading and managing motor outputs. [21] The platform software is Arduino. The code for the system is developed by using ArduCopter.

7.2.1 Sensors

7.2.2.1. Gyro and Accelerometer

The MPU-6000/6050 is a sensor combines three angular rate gyros with three orthogonal accelerometers with an onboard Digital Motion Processor (DMP) that processes complex algorithms for six axes.

Both the gyro and the accelerometer are user-programmable. Gyro range can be selected within the values of ±250°/sec, ±500°/sec, ±1000°/sec and ±2000°/sec and for the accelerometer the range can be selected between ±2g, ±4g, ±8g, and ±16g. [20] Besides these benefits, the sensor has a small size (4x4x0.9mm) with low power consumption. The sensor architecture is shown in Figure 100.

Figure 100 Sensor Architecture

7.2.2.2. Compass

HMC5883L is a surface mount, multi-chip module device that contains three - axis magneto resistive sensors which are designed for low field magnetic sensing with I^2C digital interface for applications such as low-cost compassing and magnetometer. It has a small size of 3.0x3.0x0.9mm surface and it can operate at a voltage range

between 2.16V and 3.6V. These functionalities can be enabled via its libraries, and additionally it has auto calibration library for ease of use. It supports heading capacity with an accuracy of 1 to 2 degrees. [21]

7.3. Washout Filter Discretization

The washout filter used in the simulation in Chapter 6.1 is discretized by using the Tustin approximation [22] and embedded into the code before performing the flight tests. The transfer function of the washout filter in continuous time is shown in Eqn. (78).

$$TF = \frac{\tau s}{\tau s + 1} \tag{78}$$

where τ is the time constant and taken as 4 as explained in Chapter 6.1.
Let s be repserented by z-equivalent, Bilinear Transform;

$$s \approx \frac{2}{T} \times \frac{z-1}{z+1} \tag{79}$$

where T is the sampling period. The installed hardware has an inertial measurement unit with a sampling frequency of 100 Hz. Hence, the sampling period T is taken as 0.01s. After rearranging the transfer function with the Bilinear Transform and then applying the incerse z-Transform, the discretized form of the high pass filter is preseted in Eqn. (80) [22]

$$y(n) = \frac{(2\tau - T)}{(2\tau + T)} y(n-1) + \frac{2\tau}{(2\tau + T)} x(n) - \frac{2\tau}{(2\tau + T)} x(n-1) \tag{80}$$

where $y(n)$ is the current output value and $y(n-1)$ is the previous output value, $x(n)\ and\ x(n-1)$ are the current and previous input values (body rates) respectively.

7.3 Tests and Results

7.3.1 Tests with the test equipment

The controller that is installed on the onboard microcontroller is tested with the test equipment. The electric motors are rotating at a specified throttle value and the response of the system is observed against pilot commands.

The electric motors are rotating at 50% throttle initially and pilot commands are given in roll, pitch and yaw respectively. The results are shown in Figure 101-Figure 103.

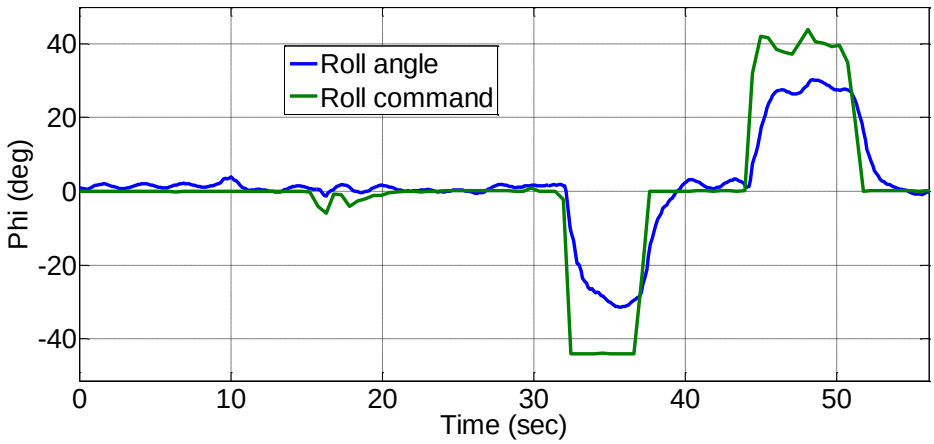

Figure 101 Roll attitude and roll command as a function of time

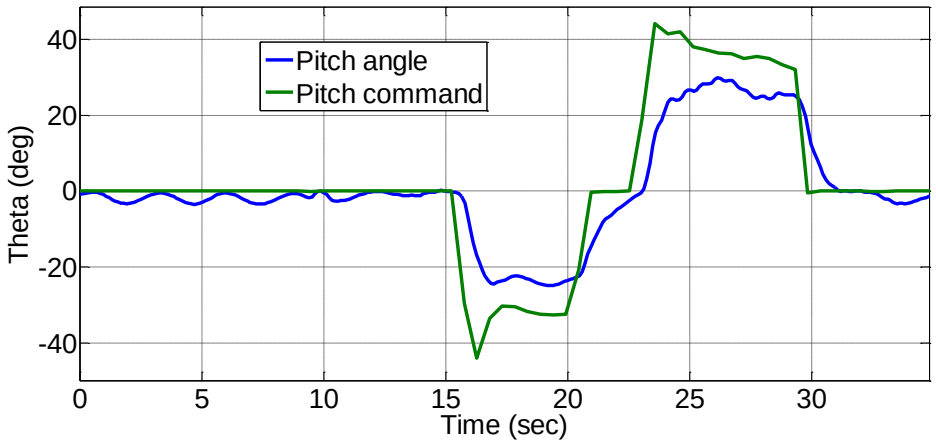

Figure 102 Pitch attitude and pitch command as a function of time

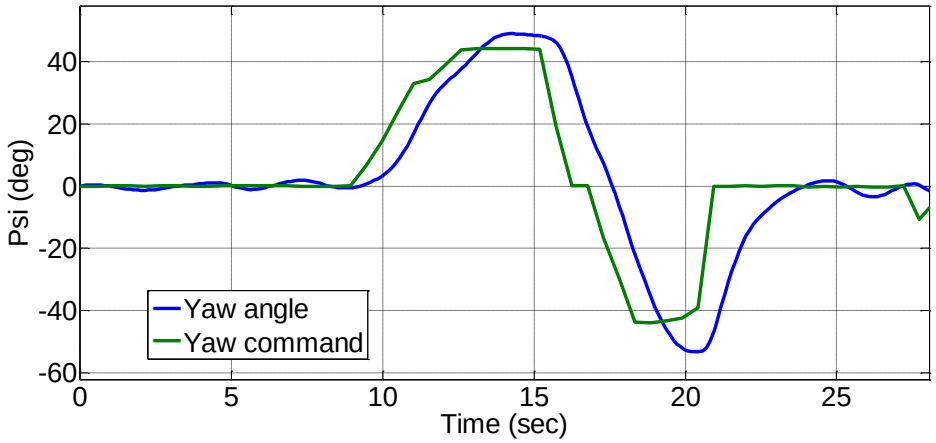

Figure 103 Yaw attitude and yaw command as a function of time

From the test results shown in Figure 101-Figure 103, it may be observed that the pilot commands are followed by the aircraft immediately and as the command is nulled the states converge to their steady state value as it was previously observed through the simulation results in Figure 37-Figure 66. After verifying the controller with the installed hardware on the test equipment, the aircraft is tested in free hover flight without any test equipment and data is gathered during the flight tests. The flight test results are presented in the following chapter.

7.3.2 Flight Tests

In addition to the tests with the test equipment, the aircraft is tested in hover for three different cases. First, LQR is used without the washout filter, then, LQR is used with the washout filter and finally, LQT is used as the attitude controller. Flight test data is gathered in all tests and the results are shown in Figure 105-Figure 113. An example photo from the flight tests is shown in Figure 104.

Figure 104 Flight test photo

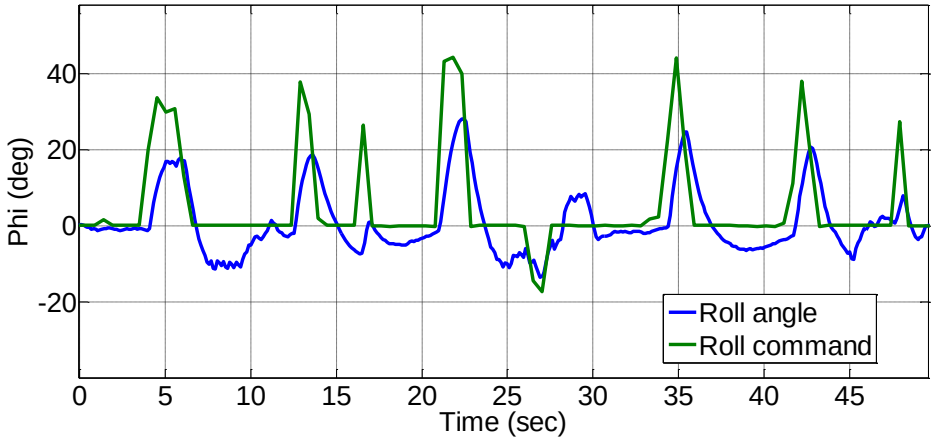

Figure 105 Commanded and realized roll angles with LQR controller without washout filter

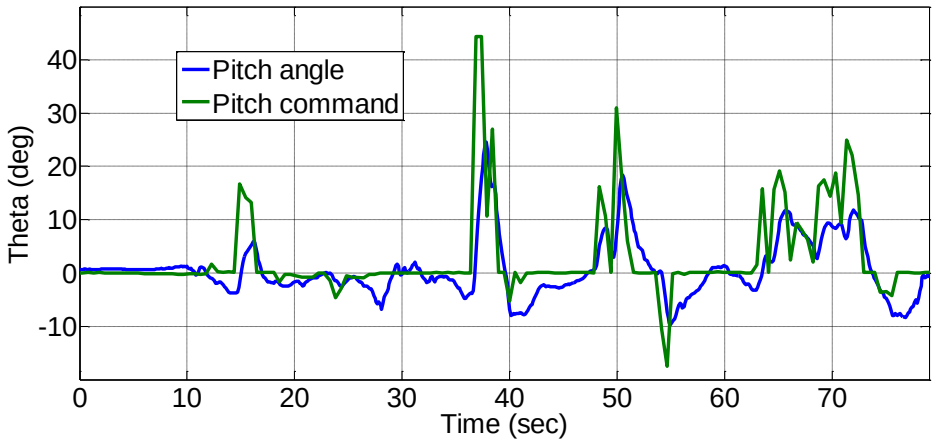

Figure 106 Commanded and realized pitch angles with LQR controller without washout filter

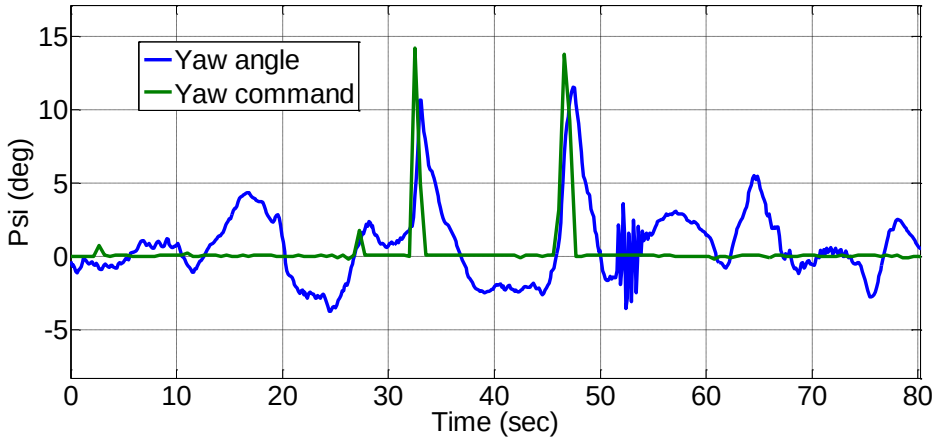

Figure 107 Commanded and realized yaw angles with LQR controller without washout filter

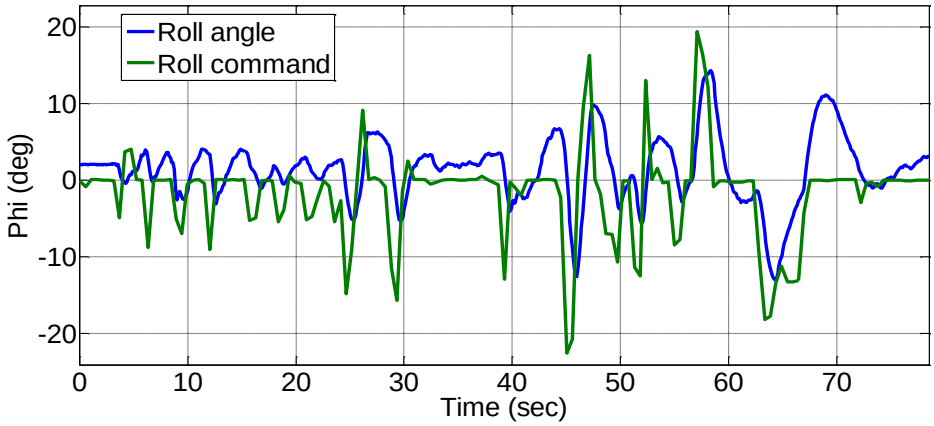

Figure 108 Commanded and realized roll angles with LQR controller with washout filter

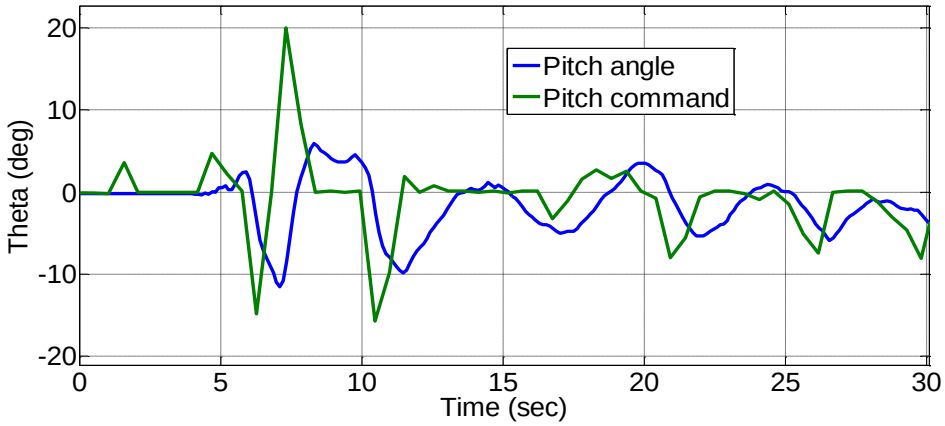

Figure 109 Commanded and realized pitch angles with LQR controller with washout filter

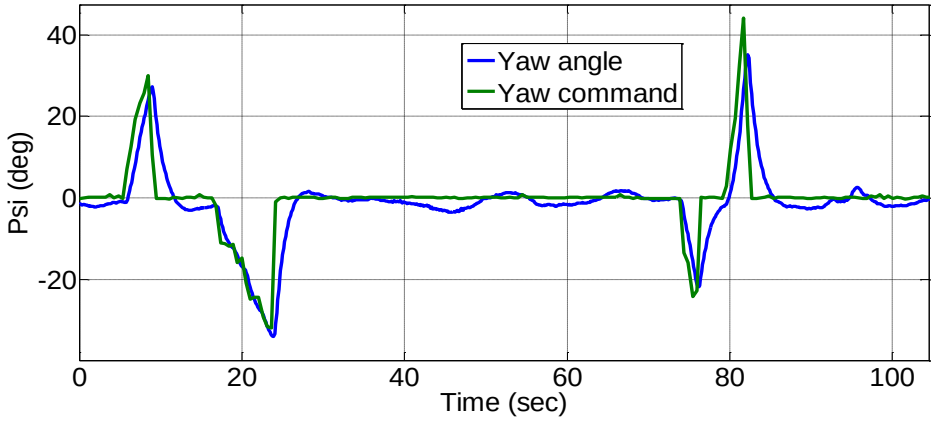

Figure 110 Commanded and realized yaw angles with LQR controller with washout filter

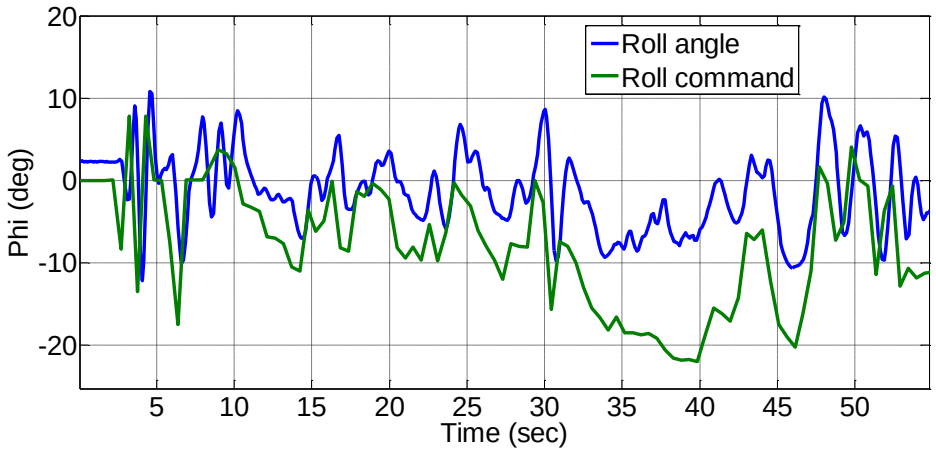

Figure 111 Commanded and realized roll angles with LQT controller

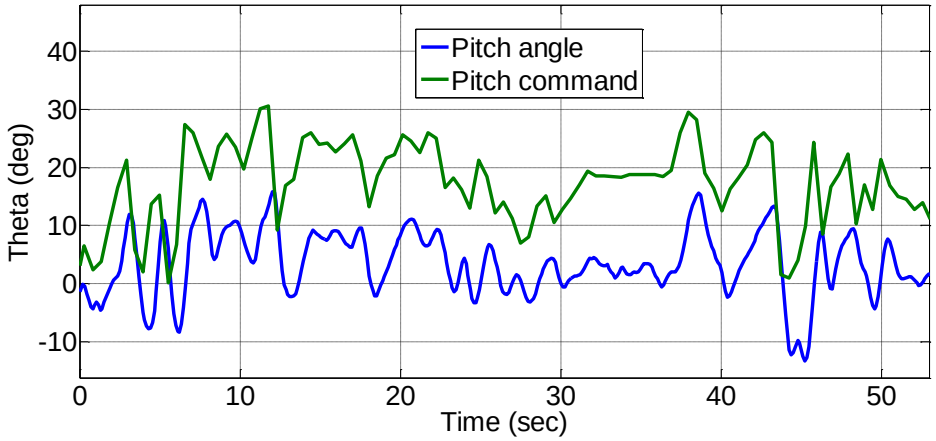

Figure 112 Commanded and realized pitch angles with LQT controller

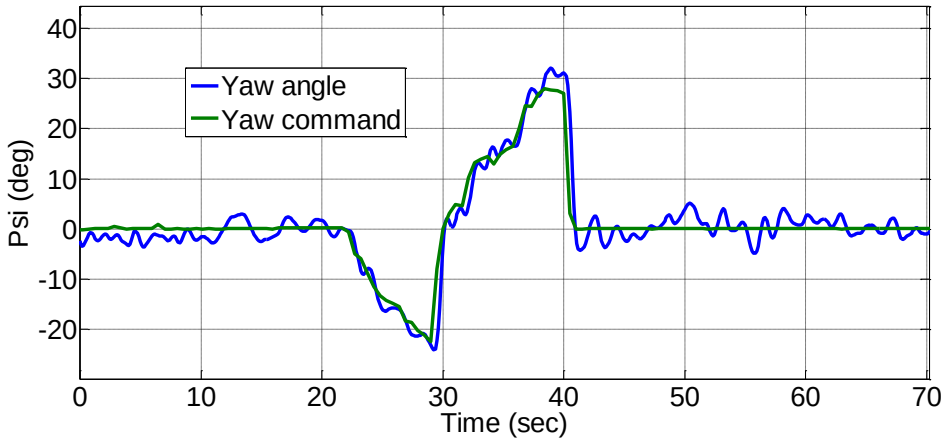

Figure 113 Commanded and realized yaw angles with LQT controller

The test results presented in Figure 105-Figure 107 show that the aircraft is not tracking the Euler angle commands as good as expected. The pilot also complained that the commands are obeyed with the aircraft and there was difficulty in steering the aircraft.

As a result of this initial test, washout filters are added to the angular velocity measurements. The test results are presented in Figure 108-Figure 110 show roll, pitch and yaw angles together with the commands send by the pilot. It may be observed from these results that the tracking of the commands are much better with the washout filter. Especially almost a perfect fit is observable on the yaw channel (Figure 110). Pilot also commented that he could steer the aircraft without any difficulty.

Since LQT controller is easier to be implemented than a washout filter in the autopilot, it is also implemented and flight tests are carried out. The associated results on commanded and realized Euler angles are presented in Figure 111-Figure 113. In the roll and pitch channels, the commands are being followed by an offset. In the yaw channel on the other hand, the tracking is almost perfect. During the flight tests there was substantial wind blowing. In spite of this adverse effect, pilot indicated that it was easy to pilot the aircraft. The effect of wind is more pronounced in the roll and pitch channels. In the yaw channel, it had a lesser effect. Thus, it may be concluded that LQT controller is easier to implement and also quite successful in controlling the aircraft attitude.

CHAPTER 8

CONCLUSIONS

In this thesis a nonlinear model of a small tilt rotor VTOL aircraft is developed. The air vehicle has a tricopter configuration and is capable of taking-off and landing vertically. After taking off, it shall start a forward flight by tilting the propellers forward. The nonlinear simulation model of the air vehicle that describes the physical properties in detail is created in the MATLAB/Simulink environment, which consists of a propulsion model, aerodynamics model, gravity model and the translational and rotational equations of motion. While developing the model, experimental studies and numerical analyses are carried out.

A linear model of the aircraft is also obtained. For this purpose, appropriate trim conditions are specified for hover and forward flight phases separately. Linear Quadratic Regulator (LQR), with and without washout filters and Linear Quadratic Tracking (LQT) controllers are designed for hover and forward flight phases. The performance of the controllers against pilot commands is analyzed through nonlinear simulations and the results are compared. The aircraft with proper hardware is built and tested in hover phase. The test results show that the controller developed successfully keeps its commended Euler angles. A high pass filter (washout filter) is used both in simulation and flight tests with LQR controller and the effect of the filter is observed and discussed. Moreover LQT is also used in the flight tests and the results are compared with LQR. Based on the simulations and flight tests, it may be concluded that the response of the LQT controller is the fastest.

In this study vertical takeoff and landing of the aircraft is mainly considered. The future study should include transition and forward flight phases with altitude and speed controllers, as well as its flight tests. Nonlinear controllers shall also be

developed in the future and the performances shall be compared against the linear controllers presented in this study.

REFERENCES

[1] Kurtuluş Bozdemir, D. F., Şenipek, M., Yayla, M., Rouzbar, R., Kozan, E., Kalkan, U., Hoş, B., Ceylan, E., Sarsılmaz, B., Özdemir, V., Yosheph, Y., Limon, A. U., Akel, E., Özlav, C., Uzunlar, İ. Ö., Güngör, O., Şenol, N., Usta, A., Middle East Technical University, Aerospace Engineering Department, Competition Design Report, *AIAA/DBF(Design Build and Fly), 2013.*

[2] Israel Aerospace Industries Ltd., *Business Areas Unmanned Air Systems Panther Family*, Retrieved from http://www.iai.co.il/2013/35673-en/BusinessAreas_UnmannedAirSystems_PantherFamily.aspx, 2002. [Last accessed on January 2014]

[3] Aerovel Corporation, Flexrotor Retrieved from http://www.aerovelco.com/Flexrotor.html, 2013. [Last accessed on January 2014]

[4] Schmittle, H. The Floating Wings That Automatically Cancel Turbulence, Retrieved from http://www.freewing.com, 2013. [Last accessed on January 2014]

[5] Muraoka, K.., Okada, N., Kubo, D., Sato, M., Transition Flight Of Quad Tilt Wing VTOL UAV, *International Congress of the Aeronautical Sciences*, 2012.

[6] Johnson, E. N., Wu A., Neidhoefer, J. C., Kannan, S. K., Turbe, M. A., Flight-Test Results of Autonomous Airplane Transitions Between Steady-Level and Hovering Flight, *Journal of Guidance, Control and Dynamics*, vol. 31, no. 2, pp. 358–370, Mar. 2008.

[7] Kim, B. M., Choi, K., Kim, B. S., Trajectory Tracking Controller Design Using Neural Networks for Tiltrotor UAV, *AIAA Guidance, Navigation and Control Conference and Exhibit*, 2007.

[8] Rudin, K., Schwesinger, U., Alexis, K., Siegwart, R., Verling, S., Zilly, J., Modeling and Control of a VTOL Glider, *Bachelor Thesis, ETH*, 2013.

[9] Barsk, K., Model Predictive Control of a Tricopter, *Thesis*, Department of Electrical Engineering, Linköping University, 2012.

[10] Drela, M, QPROP Formulation, Retrieved from: http://web.mit.edu/drela/Public/web/qprop, June, 2006. [Last accessed on March 2014]

[11] Önen, A. S., Şenipek, M., Mutlu, T., Cevher, L., Güngör, O., Kurtuluş Bozdemir, D. F., Tekinalp, O., The wind tunnel tests for the propulsion system of a VTOL UAV, *HİTEK*, Istanbul, Turkey, 18-19 June 2014.

[12] Deperrois, C. A., About XFLR5 calculations and experimental measurements, Retrieved from http://www.xflr5.com/docs/Results_vs_Prediction.pdf, October, 2009. [Last accessed on June 2014]

[13] Roskam, J., *Airplane Flight Dynamics and Automatic Flight Controls*, 3rd ed.,DAR Corporation, 2001.

[14] Ünlü, T., Flight Control Of A Tilt Duct UAV With Emphasis On The Over Actuated Transition Flight Phase, *Thesis*, Department of Aerospace Engineering, METU, 2009.

[15] Gavin, H. P., The Levenberg-Marquardt method for nonlinear least squares curve-fitting problems, *Dep. Civ. Environ. Eng. Duke Univ.*, 2013.

[16] Önen, A. S., Cevher, L., Mutlu, T., Özdemir, İ. Ö., Kurtuluş Bozdemir, D. F., Tekinalp, O., Conversion of a conventional UAV into a VTOL UAV, *SAVTEK*, Ankara, Turkey, 2014.

[17] Ogata, K., *Modern Control Engineering*, 3rd ed. Prentice-Hall, 1997.

[18] Hull, D. G., *Optimal Control Theory for Applications*. Springer, 2003.

[19] Hespanha, J. P., *Lecture notes on LQR / LQG controller design*, University of California, 2005.

[20] Prach, A., Tekinalp, O., Development of a State Dependent Riccati Equation Based Trracking Flight Controller for an Unmanned Aircraft, AIAA Guidance, Navigation and Control (GNC) Conference, Boston, MA, 19-22 August 2013

[21] Cuartielles, D., Arduino Mega 2560, Retrieved from http://arduino.cc/en/Main/ArduinoBoardMega2560, 2005. [Last accessed on July 2014]

[22] Haugen, F., Discrete-time signals and systems, Telemark University College, 17 February 2005.

APPENDIX A

PROPELLER GEOMETRIC DIMENSIONS

Table A1 10X5 Propeller Geometric Dimensions

Local Blade Chord (mm)	Local Blade Angle (deg)	Local Radius (mm)
22.2	32.2	22.02
25.1	27.7	32.23
28.0	24.3	41.92
29.8	21.7	51.07
29.7	19.6	59.69
27.8	18.1	67.78
24.8	16.8	75.34
21.5	15.8	82.37
18.5	15.0	88.87
16.1	14.3	94.84
14.2	13.7	100.28
12.6	13.2	105.18
11.2	12.7	109.56
9.97	12.3	113.41
8.76	11.9	116.72
7.63	11.6	119.51
6.62	11.3	121.76
5.78	11.1	123.49

Table A2 11X4 Propeller Geometric Dimensions

Local Blade Chord (mm)	**Local Blade Angle (deg)**	**Local Radius (mm)**
23.7	28.19	21.0
23.6	30.01	27.9
23.5	30.46	34.9
22.9	27.59	41.9
22.6	23.97	48.9
22.5	21.02	55.9
22.6	18.63	62.9
22.8	16.77	69.9
22.8	15.23	76.8
22.5	13.88	83.8
22.0	12.74	90.8
21.4	11.63	97.8
20.0	10.69	104.8
18.0	9.80	111.8
15.2	8.69	118.7
11.7	7.32	125.7
7.12	6.29	132.7
2.37	5.29	139.7

APPENDIX B

AERODYNAMIC COEFFICIENTS FOR WING AND TAIL

Table A3 Lift coefficient (C_L) of the wing for different angles of attack and side-slip angles at -20 degree aileron deflection

Side-slip angle (deg)

Angle of attack (deg)	-60	-30	0	30	60
-16	-0.250193	-0.408974	-0.457041	-0.427889	-0.222612
-14	-0.205387	-0.321028	-0.353444	-0.349301	-0.201668
-12	-0.159581	-0.2308	-0.246519	-0.266173	-0.175683
-10	-0.11336	-0.139022	-0.137	-0.179123	-0.144973
-8	-0.067314	-0.04644	-0.025646	-0.088809	-0.109914
-6	-0.022029	0.046191	0.086761	0.004072	-0.070929
-4	0.02192	0.138117	0.199427	0.098791	-0.02849
-2	0.063972	0.228592	0.311554	0.194599	0.016892
0	0.103592	0.316884	0.422349	0.290731	0.064669
2	0.140271	0.402286	0.531029	0.386418	0.114264
4	0.173537	0.484123	0.636833	0.48089	0.165078
6	0.202956	0.561755	0.739025	0.573386	0.216494
8	0.228138	0.63459	0.836909	0.663166	0.267887
10	0.248744	0.702085	0.929828	0.749511	0.318629
12	0.264486	0.763754	1.017174	0.83174	0.368094
14	0.275132	0.819173	1.098398	0.909208	0.415672
16	0.280509	0.867982	1.173009	0.981318	0.460767

Table A4 Lift coefficient (C_L) of the wing for different angles of attack and side-slip angles at 0 degree aileron deflection

Angle of attack (deg) \ Side-slip angle (deg)	-60	-30	0	30	60
-16	-0.320425	-0.535017	-0.582468	-0.535017	-0.320425
-14	-0.272778	-0.428118	-0.451534	-0.428118	-0.272778
-12	-0.22272	-0.31827	-0.317613	-0.31827	-0.22272
-10	-0.170649	-0.206076	-0.181376	-0.206076	-0.170649
-8	-0.116984	-0.092161	-0.043514	-0.092161	-0.116984
-6	-0.062161	0.022829	0.095259	0.022829	-0.062161
-4	-0.006627	0.138239	0.234223	0.138239	-0.006627
-2	0.04916	0.253408	0.372653	0.253408	0.04916
0	0.104742	0.367673	0.509827	0.367673	0.104742
2	0.159662	0.480383	0.645032	0.480383	0.159662
4	0.213469	0.590898	0.777576	0.590898	0.213469
6	0.265724	0.698599	0.906787	0.698599	0.265724
8	0.316003	0.802895	1.032025	0.802895	0.316003
10	0.363904	0.903226	1.152686	0.903226	0.363904
12	0.409049	0.999067	1.268208	0.999067	0.409049
14	0.451088	1.089941	1.378076	1.089941	0.451088
16	0.489706	1.175413	1.481826	1.175413	0.489706

Table A5 Drag coefficient (C_D) of the wing for different angles of attack and side-slip angles at 20 degree aileron deflection

Angle of attack (deg) \ Side-slip angle (deg)	-60	-30	0	30	60
-16	0.04841	0.054009	0.054653	0.050483	0.043864
-14	0.037313	0.041894	0.043679	0.038713	0.031293
-12	0.027416	0.032081	0.035455	0.029817	0.021204
-10	0.018976	0.024783	0.03013	0.023888	0.013634
-8	0.012229	0.020184	0.027811	0.020983	0.008591
-6	0.007394	0.018434	0.028573	0.021121	0.006049
-4	0.004662	0.019647	0.032451	0.024286	0.005956
-2	0.004203	0.023902	0.039443	0.030423	0.008225
0	0.006156	0.031241	0.049506	0.039442	0.012743
2	0.010632	0.041666	0.062563	0.051214	0.01937
4	0.01771	0.055142	0.078495	0.065581	0.027938
6	0.02744	0.071599	0.097153	0.082349	0.038258
8	0.039835	0.090925	0.118348	0.101295	0.050116
10	0.054879	0.112977	0.141863	0.122169	0.063281
12	0.072522	0.137574	0.167449	0.144695	0.077505
14	0.092682	0.164504	0.194831	0.168577	0.092526
16	0.115243	0.193526	0.223709	0.193499	0.108071

Table A6 Pitching moment coefficient (C_M) of the wing for different angles of attack and side-slip angles at 10 degree aileron deflection

Angle of attack (deg) \ Side-slip angle (deg)	-60	-30	0	30	60
-16	0.055614	0.066306	-0.241272	-0.085213	-0.020963
-14	0.049171	0.052445	-0.21328	-0.101405	-0.028332
-12	0.042045	0.037266	-0.185367	-0.118545	-0.036187
-10	0.034271	0.020844	-0.157671	-0.13655	-0.044491
-8	0.025886	0.003257	-0.130326	-0.155331	-0.053203
-6	0.016931	-0.015407	-0.103465	-0.174797	-0.062281
-4	0.007451	-0.035058	-0.077219	-0.194853	-0.07168
-2	-0.002509	-0.055601	-0.051717	-0.215401	-0.081354
0	-0.0129	-0.076935	-0.027081	-0.236342	-0.091257
2	-0.023672	-0.098957	-0.003433	-0.257573	-0.10134
4	-0.034772	-0.121559	0.019112	-0.278991	-0.111554
6	-0.046147	-0.14463	0.040445	-0.300492	-0.121849
8	-0.05774	-0.168059	0.060462	-0.32197	-0.132175
10	-0.069495	-0.191732	0.079065	-0.343322	-0.142482
12	-0.081355	-0.215533	0.096163	-0.364442	-0.15272
14	-0.093262	-0.239346	0.111674	-0.385229	-0.162838
16	-0.105158	-0.263055	0.125521	-0.405581	-0.172788

Table A7 Rolling moment coefficient (C_L) of the wing for different angles of attack and side-slip angles at -10 degree aileron deflection

Angle of attack (deg) \ Side-slip angle (deg)	-60	-30	0	30	60
-16	0.000961	-0.025084	-0.048281	-0.035255	-0.010732
-14	0.000108	-0.02535	-0.048678	-0.035166	-0.009475
-12	-0.00047	-0.025421	-0.049016	-0.035235	-0.008544
-10	-0.000797	-0.025311	-0.049292	-0.035451	-0.007923
-8	-0.000897	-0.025035	-0.049506	-0.035802	-0.007588
-6	-0.000798	-0.02461	-0.049659	-0.036271	-0.007515
-4	-0.00053	-0.024054	-0.04975	-0.03684	-0.007674
-2	-0.000125	-0.023388	-0.049778	-0.037491	-0.008035
0	0.000382	-0.022632	-0.049744	-0.038203	-0.008563
2	0.000957	-0.021808	-0.049648	-0.038953	-0.009222
4	0.001563	-0.020939	-0.049489	-0.039719	-0.009973
6	0.002164	-0.020045	-0.049267	-0.040477	-0.010778
8	0.002724	-0.019151	-0.048984	-0.041204	-0.011596
10	0.003207	-0.018278	-0.048639	-0.041874	-0.012386
12	0.003577	-0.017447	-0.048233	-0.042463	-0.01311
14	0.003802	-0.016681	-0.047766	-0.042949	-0.013726
16	0.003848	-0.015997	-0.047239	-0.043308	-0.014197

Table A8 Side force coefficient (C_Y) of the wing for different angles of attack and side-slip angles at 0 degree aileron deflection

Angle of attack (deg) \ Side-slip angle (deg)	-60	-30	0	30	60
-16	0.050833	0.055152	0	-0.055152	-0.050833
-14	0.040812	0.040469	0	-0.040469	-0.040812
-12	0.031389	0.027406	0	-0.027406	-0.031389
-10	0.02261	0.016028	0	-0.016028	-0.02261
-8	0.014517	0.006391	0	-0.006391	-0.014517
-6	0.007151	-0.00146	0	0.00146	-0.007151
-4	0.000546	-0.007485	0	0.007485	-0.000546
-2	-0.005264	-0.011656	0	0.011656	0.005264
0	-0.010252	-0.013952	0	0.013952	0.010252
2	-0.014393	-0.014361	0	0.014361	0.014393
4	-0.017667	-0.012883	0	0.012883	0.017667
6	-0.020058	-0.009523	0	0.009523	0.020058
8	-0.021554	-0.004299	0	0.004299	0.021554
10	-0.022149	0.002764	0	-0.002764	0.022149
12	-0.021839	0.011632	0	-0.011632	0.021839
14	-0.020626	0.022261	0	-0.022261	0.020626
16	-0.018515	0.0346	0	-0.0346	0.018515

Table A9 Yawing moment coefficient (C_N) of the wing for different angles of attack and side-slip angles at 20 degree aileron deflection

Angle of attack (deg) \ Side-slip angle (deg)	-60	-30	0	30	60
-16	-0.00895	-0.00374	0.00023	-0.005281	-0.00533
-14	-0.007352	-0.002984	0.000197	-0.005068	-0.005365
-12	-0.005834	-0.00228	0.000161	-0.004743	-0.005227
-10	-0.00443	-0.001647	0.000123	-0.004296	-0.004896
-8	-0.003172	-0.001105	8.2e-05	-0.003716	-0.004356
-6	-0.002087	-0.000671	3.9e-05	-0.002995	-0.003595
-4	-0.001205	-0.000361	-6e-06	-0.002127	-0.002599
-2	-0.00055	-0.000191	-5.2e-05	-0.001106	-0.001362
0	-0.000144	-0.000173	-9.9e-05	6.9e-05	0.000123
2	-6e-06	-0.000319	-0.000147	0.0014	0.001858
4	-0.000152	-0.000639	-0.000195	0.002886	0.003841
6	-0.000595	-0.00114	-0.000243	0.004524	0.006071
8	-0.001342	-0.001826	-0.00029	0.00631	0.008539
10	-0.0024	-0.002701	-0.000336	0.008237	0.011237
12	-0.00377	-0.003764	-0.00038	0.010297	0.014152
14	-0.005448	-0.005014	-0.000423	0.012479	0.017267
16	-0.007429	-0.006447	-0.000464	0.014772	0.020566

Table A10 Lift coefficient (C_L) of the tail for different angles of attack and control surface deflections

Angle of attack (deg) \ Control Surface Deflection (deg)	-20	-10	0	10	20
-16	0.088635	-0.209761	-0.534403	-0.876757	-1.22563
-14	0.160369	-0.138692	-0.466544	-0.814947	-1.172763
-12	0.232093	-0.06651	-0.396392	-0.749674	-1.115334
-10	0.303448	0.006436	-0.324266	-0.681201	-1.053526
-8	0.374075	0.079788	-0.250505	-0.609821	-0.987562
-6	0.443621	0.15318	-0.175462	-0.535853	-0.917699
-4	0.511741	0.226248	-0.099502	-0.459637	-0.844231
-2	0.578101	0.298629	-0.023	-0.381537	-0.767483
0	0.642381	0.369964	0.053665	-0.301931	-0.687806
2	0.70428	0.439904	0.13011	-0.221211	-0.605581
4	0.763516	0.508113	0.205956	-0.139779	-0.521207
6	0.819832	0.574267	0.28083	-0.058042	-0.435102
8	0.872993	0.638063	0.354366	0.02359	-0.3477
10	0.922796	0.699219	0.426212	0.10471	-0.259443
12	0.969063	0.757474	0.496033	0.184917	-0.17078
14	1.01165	0.812597	0.563509	0.263819	-0.082159
16	1.050442	0.864382	0.628346	0.341039	0.005971

Table A11 Pitching moment coefficient (C_M) of the tail for different angles of attack and control surface deflections

Angle of attack (deg) \ Control Surface Deflection (deg)	-20	-10	0	10	20
-16	-0.109211	-0.108454	-0.110123	-0.113486	-0.118131
-14	-0.093946	-0.093087	-0.094205	-0.096568	-0.099744
-12	-0.078804	-0.077852	-0.078417	-0.079772	-0.081462
-10	-0.063858	-0.062821	-0.062838	-0.063182	-0.063372
-8	-0.049182	-0.048068	-0.047542	-0.046877	-0.045564
-6	-0.034846	-0.033665	-0.032605	-0.030937	-0.028125
-4	-0.020921	-0.019682	-0.018098	-0.01544	-0.011139
-2	-0.007474	-0.006187	-0.004093	-0.000461	0.005312
0	0.005428	0.006754	0.009342	0.013927	0.021146
2	0.017724	0.019077	0.022141	0.027653	0.036287
4	0.029353	0.030724	0.034243	0.040651	0.050661
6	0.040259	0.041637	0.045588	0.052857	0.064198
8	0.050388	0.051763	0.056121	0.064212	0.076832
10	0.059691	0.061052	0.065791	0.074661	0.088501
12	0.068123	0.069461	0.074551	0.084153	0.099149
14	0.075643	0.076946	0.082358	0.092641	0.108724
16	0.082214	0.083473	0.089173	0.100085	0.117178

Table A12 Side force coefficient (C_Y) of the tail for different side slip angles and control surface deflections

Side-slip angle (deg) \ Control surface deflection (deg)	-20	-10	0	10	20
-60	0.844353	0.787785	0.731322	0.693196	0.646588
-30	0.754314	0.642611	0.534258	0.40995	0.27283
0	0.349781	0.171839	0	-0.171839	-0.349781
30	-0.27283	-0.40995	-0.534258	-0.642611	-0.754314
60	-0.646588	-0.693196	-0.731322	-0.787785	-0.844353

Table A13 Yawing moment coefficient (C_N) of the tail for side slip angles and control surface deflections

Side-slip angle (deg) \ Control surface deflection (deg)	-20	-10	0	10	20
-60	-0.075874	-0.069129	-0.061252	-0.054107	-0.046605
-30	-0.026555	-0.024089	-0.023188	-0.016834	-0.010596
0	-0.00574	-0.00272	0	0.00272	0.00574
30	0.010596	0.016834	0.023188	0.024089	0.026555
60	0.046605	0.054107	0.061252	0.069129	0.075874

APPENDIX C

C.1. LINEARIZED SYSTEM MATRICES FOR HOVER

Asys =

-0.0000	-0.0000	0.0000	0	0	0	0	0	-0.1402	0	0	0
0.0000	-0.0000	-0.0000	0	0	0	0	0	-0.0010	0	0	0
0.0000	-0.0000	-0.0000	0	0	0	0	0	-0.0304	0	0	0
1.0000	-0.0000	0.0000	0	0.0000	0	0	0	0	0	0	0
0	0.9999	0.0133	-0.0000	0	0	0	0	0	0	0	0
0	-0.0133	0.9999	-0.0000	0.0000	0	0	0	0	0	0	0
0	0.0000	0.0000	0	-9.8100	0	0	-0.0000	0.0000	0	0	0
-0.0000	0	0.0000	9.8091	0.0000	0	0.0000	0	0.0041	0	0	0
-0.0000	-0.0000	0	0.1308	-0.0000	0	-0.0000	0.0000	-0.3062	0	0	0
0	0	0	0	-0.0000	0.0000	1.0000	-0.0000	0.0000	0	0	0
0	0	0	0.0000	0	-0.0000	0	0.9999	0.0133	0	0	0
0	0	0	-0.0000	0.0000	0	-0.0000	-0.0133	0.9999	0	0	0

Bsys =

0.5652	-0.6503	-0.0617	3.1109
0.1610	0.1496	-0.3127	0.1744
0.0088	-0.0078	-0.0040	-24.6034
0	0	0	0
0	0	0	0
0	0	0	0
0	0	0	0
0	0	0.0027	3.2670
-0.0681	-0.0638	-0.0663	0.1309
0	0	0	0
0	0	0	0
0	0	0	0

Csys =

0	0	0	0	-0.0000	0.0000	1.0000	-0.0000	0.0000	0	0	0
0	0	0	0.0000	0	-0.0000	0	0.9999	0.0133	0	0	0
0	0	0	-0.0000	0.0000	0	-0.0000	-0.0133	0.9999	0	0	0
0	0	0	0	0	0	0	0	0	1.0000	0	0
0	0	0	0	0	0	0	0	0	0	1.0000	0
0	0	0	0	0	0	0	0	0	0	0	1.0000
0	0	0	1.0000	0	0	0	0	0	0	0	0
0	0	0	0	1.0000	0	0	0	0	0	0	0
0	0	0	0	0	1.0000	0	0	0	0	0	0
0	0	0	0	0	0	1.0000	0	0	0	0	0
0	0	0	0	0	0	0	1.0000	0	0	0	0
0	0	0	0	0	0	0	0	1.0000	0	0	0

```
Dsys =

     0     0     0     0
     0     0     0     0
     0     0     0     0
     0     0     0     0
     0     0     0     0
     0     0     0     0
     0     0     0     0
     0     0     0     0
     0     0     0     0
     0     0     0     0
     0     0     0     0
     0     0     0     0
```

C.2. LINEARIZED SYSTEM MATRICES FOR FORWARD FLIGHT

```
Asys =

  -0.3063   -0.0109   -1.0632         0   -0.0101    0.0271         0   -9.8100         0         0         0         0
   0.0001   -0.1971    0.0002    0.0285   -0.0000  -14.7380    9.8100    0.0000         0         0         0         0
  -1.2979    0.3462   -5.3483   -0.0021   14.6152    0.0069    0.0007   -0.0187         0         0         0         0
   0.0001   -0.3479   -0.0020   -2.3134   -0.0155    0.9607         0         0         0         0         0         0
   0.0024   -1.4011   -1.1458   -0.0028   -5.3069   -0.0142         0         0         0         0         0         0
   0.0000   -0.0814    0.0023    0.0239    0.0113  -10.0090         0         0         0         0         0         0
        0         0         0    1.0000   -0.0000    0.0019   -0.0000   -0.0000         0         0         0         0
        0         0         0         0    1.0000    0.0001    0.0000         0         0         0         0         0
        0         0         0         0   -0.0001    1.0000   -0.0000   -0.0000         0         0         0         0
   1.0000    0.0001    0.0019         0         0         0   -0.0000   -0.0001   -0.0001         0         0         0
  -0.0001    1.0000    0.0001         0         0         0   -0.0285    0.0000   15.0000         0         0         0
  -0.0019   -0.0001    1.0000         0         0         0    0.0021  -15.0000         0         0         0         0
```

```
Bsys =

    0.0703   -1.1355   -0.0793    0.1569
         0   -0.1234         0   -3.1683
         0    5.2925    6.6109   -0.0003
         0 -210.4362    0.2152  -10.8637
         0    0.7275   73.5970   -0.0160
         0    2.3372   -0.1571   -0.3845
         0         0         0         0
         0         0         0         0
         0         0         0         0
         0         0         0         0
         0         0         0         0
         0         0         0         0
```

Csys =

1.0000	0.0001	0.0019	0	0	0	-0.0000	-0.0001	-0.0001	0	0	0
-0.0001	1.0000	0.0001	0	0	0	-0.0285	0.0000	15.0000	0	0	0
-0.0019	-0.0001	1.0000	0	0	0	0.0021	-15.0000	0	0	0	0
0	0	0	0	0	0	0	0	0	1.0000	0	0
0	0	0	0	0	0	0	0	0	0	1.0000	0
0	0	0	0	0	0	0	0	0	0	0	1.0000
0	0	0	0	0	0	1.0000	0	0	0	0	0
0	0	0	0	0	0	0	1.0000	0	0	0	0
0	0	0	0	0	0	0	0	1.0000	0	0	0
1.0000	0	0	0	0	0	0	0	0	0	0	0
0	1.0000	0	0	0	0	0	0	0	0	0	0
0	0	1.0000	0	0	0	0	0	0	0	0	0
0	0	0	1.0000	0	0	0	0	0	0	0	0
0	0	0	0	1.0000	0	0	0	0	0	0	0
0	0	0	0	0	1.0000	0	0	0	0	0	0
0.0001	-0.3479	-0.0020	-2.3134	-0.0155	0.9607	0	0	0	0	0	0
0.0024	-1.4011	-1.1458	-0.0028	-5.3069	-0.0142	0	0	0	0	0	0
0.0000	-0.0814	0.0023	0.0239	0.0113	-10.0090	0	0	0	0	0	0
-0.3063	-0.0109	-1.0632	0	0.0184	0.0250	0	-9.8100	0	0	0	0
0.0001	-0.1971	0.0002	0	-0.0000	0.2620	9.8100	0.0000	0	0	0	0
-1.2979	0.3462	-5.3483	0	-0.3848	0.0069	0.0007	-0.0187	0	0	0	0

Dsys =

0	0	0	0
0	0	0	0
0	0	0	0
0	0	0	0
0	0	0	0
0	0	0	0
0	0	0	0
0	0	0	0
0	0	0	0
0	0	0	0
0	0	0	0
0	0	0	0
0	0	0	0
0	0	0	0
0	0	0	0
0	-210.4362	0.2152	-10.8637
0	0.7275	73.5970	-0.0160
0	2.3372	-0.1571	-0.3845
0.0703	-1.1355	-0.0793	0.1569
0	-0.1234	0	-3.1683
0	5.2925	6.6109	-0.0003

C.3. REDUCED SYSTEM MATRICES FOR HOVER

Asys =

-0.0000	-0.0000	0.0000	0	0	0
0.0000	-0.0000	-0.0000	0	0	0
0.0000	-0.0000	-0.0000	0	0	0
1.0000	-0.0000	0.0000	0	0.0000	0
0	0.9999	0.0133	-0.0000	0	0
0	-0.0133	0.9999	-0.0000	0.0000	0

```
Bsys =

    0.5652   -0.6503   -0.0617    3.1109
    0.1610    0.1496   -0.3127    0.1744
    0.0088   -0.0078   -0.0040  -24.6034
         0         0         0         0
         0         0         0         0
         0         0         0         0


Csys =

   1.0e-10 *

         0         0         0         0   -0.4755    0.0063
         0         0         0    0.4755         0   -0.0028
         0         0         0   -0.0063    0.0028         0
         0         0         0         0         0         0
         0         0         0         0         0         0
         0         0         0         0         0         0

Dsys =

     0     0     0     0
     0     0     0     0
     0     0     0     0
     0     0     0     0
     0     0     0     0
     0     0     0     0
```

C.4. REDUCED SYSTEM MATRICES FOR FORWARD FLIGHT

```
Asys =

   -2.3134   -0.0155    0.9607         0         0
   -0.0028   -5.3069   -0.0142         0         0
    0.0239    0.0113  -10.0090         0         0
    1.0000   -0.0000    0.0019   -0.0000   -0.0000
         0    1.0000    0.0001    0.0000         0
```

```
Bsys =

         0 -210.4362    0.2152  -10.8637
         0    0.7275   73.5970   -0.0160
         0    2.3372   -0.1571   -0.3845
         0         0         0         0
         0         0         0         0

Csys =

         0         0         0         0         0
         0         0         0         0         0
         0         0         0         0         0
         0         0         0    1.0000         0
         0         0         0         0    1.0000


Dsys =

     0     0     0     0
     0     0     0     0
     0     0     0     0
     0     0     0     0
     0     0     0     0
```

APPENDIX D

D.1. WEIGHTING MATRICES FOR HOVER

Qhover_lqr =

0.4053	0	0	0	0	0
0	0.4053	0	0	0	0
0	0	0.4053	0	0	0
0	0	0	0.4053	0	0
0	0	0	0	0.4053	0
0	0	0	0	0	0.4053

Qhover_lqt =

0.4053	0	0
0	0.4053	0
0	0	0.4053

Rhover =

0.0006	0	0	0
0	0.0006	0	0
0	0	0.0006	0
0	0	0	0.4053

D.2. WEIGHTING MATRICES FOR FORWARD FLIGHT

```
Qforward_lqr =

    0.4057         0         0         0         0
         0    0.4057         0         0         0
         0         0    0.4057         0         0
         0         0         0    0.4057         0
         0         0         0         0    0.4057

Qforward_lqt =

    0.4053         0
         0    0.4053

Rforward =

    0.0006         0         0         0
         0    8.2101         0         0
         0         0    8.2101         0
         0         0         0    8.2101
```

D.3. LQR GAIN MATRIX FOR HOVER MODE

```
KLQR_hover =

   17.2163   11.2602    1.3686   16.4940   10.2887    1.1342
  -20.1186   11.5600   -1.4431  -19.2492   10.4888   -1.4813
   -1.6074  -22.8334   -0.2931   -1.5621  -20.7986    0.0049
    0.0736    0.0075   -1.0371    0.0730   -0.0061   -0.9973
```

D.4. LQR GAIN MATRIX FOR FORWARD FLIGHT MODE

```
KLQR_forward =

         0         0         0         0         0
   -0.2160    0.0007   -0.0027   -0.2220    0.0007
    0.0006    0.1742   -0.0002    0.0007    0.2223
   -0.0112   -0.0001   -0.0014   -0.0115   -0.0001
```

D.5. LQT GAIN MATRICES FOR HOVER MODE

```
K =

    4.9402    4.6034    0.5264   16.4940   10.2887    1.1342
   -5.8403    4.8288   -0.5558  -19.2492   10.4888   -1.4813
   -0.4022   -9.4253   -0.1090   -1.5621  -20.7986    0.0049
    0.0126    0.0022   -0.2843    0.0730   -0.0061   -0.9973

Kz =

   16.4940   10.2887    1.1342
  -19.2492   10.4888   -1.4813
   -1.5621  -20.7986    0.0049
    0.0730   -0.0061   -0.9973
```

D.6. LQT GAIN MATRICES FOR FORWARD FLIGHT MODE

```
K =

         0         0         0         0         0
   -0.0362    0.0001   -0.0023   -0.2219    0.0005
    0.0001    0.0339   -0.0000    0.0005    0.2222
   -0.0019   -0.0000   -0.0001   -0.0115   -0.0001


Kz =

         0         0
   -0.2219    0.0005
    0.0005    0.2222
   -0.0115   -0.0001
```